UNIVERSITY OF LIVERPOOL

Investigating soil-root interaction and changes in soil physical properties under different soil managements using X-ray computed tomography

Dissertation presented by

Di Wang

The Department of Civil and Design Engineering

In Full Fulfilment of the Requirement for the Degree of

Doctor of Philosophy

In the Subject of

Civil Engineering

University of Liverpool

Liverpool, United Kingdom

February 2021

Acknowledgements

I would like to express my gratitude to my supervisor Dr. Ming Li who has been instrumental and patient with my research and life at the University of Liverpool over the past three years. I would also thank my external supervisor Dr. Xiaoxian Zhang at the Rothamsted Research who showed me how to do research and become a scientist by offering me the opportunity to study and work at Rothamsted Research for two years.

I am grateful to the tremendous support from the University of Liverpool and the Rothamsted Research for giving me the opportunities to study and work in their organizations, which will benefit my academic career to come.

I would like to thank the staff at the Hounsfield Facility at the University of Nottingham and the Rutherford Appleton Laboratory IMAT, especially Dr. Craig J Sturrock and Dr. Winfried Kockelmann, for teaching me how to use their X-ray computed tomography and neutron computed tomography respectively, which enabled me to quickly grasp these facilities and are valuable to my PhD project.

Finally, I am incredibly thankful to my family, especially my wife Xiangnan Li and my parents Tianshun Wang and Hui Xu. Their emotional support helps me go through the difficult times, setbacks and sometimes pains over my three and a half years of study in the UK.

Abstract

Tomography technologies including X-ray computed tomography (CT) and neutron tomography have been increasingly used by both research and industrial communities in many fields to non-invasively visualize opaque materials in three dimensions. Their applications in soil science over the last decades have substantially improved our understanding of many fundamental processes which would otherwise remain unknown. With the development in both technologies, we are now able to visualize and quantify 3D pore gnomery in porous materials at a spatial resolution as fine as a few microns. Combining these with process-based pore-scale simulations would enable us to elucidate how soil structure responds to agronomic practice changes as well as its consequence for soil physical properties such as permeability, water retention and tortuosity at different scales, which are important for soil functions. My PhD project aims to build a new system to investigate soil-root interaction and soil property changes induced by both agronomical practice changes and root-soil interaction.

In this thesis, I present two experimental results to analyse root growth and its consequent impact on soil structure under different managements and environments. The first experiment is to investigate how water and salinity stresses affect development of root architecture of maize in three dimensions. Maize seedlings were grown in pots packed with a loamy sand soil for three weeks under water and salinity stresses both in isolation and combination. I then scan them using X-ray CT at resolution of 110 microns to analyse the impact of these stresses on root architecture traits, including root length, root branching angle as well as diameters of the crown and primary roots. These could help us understand how plants respond to abiotic stresses by adjusting their root morphology. In the meantime, I also took soil aggregates adhered to the roots and scanned them using X-ray tomography at resolution of 4 microns to analyse the change in pore geometry under different stresses as well as its consequence for soil permeability and porosity as these parameters were important to estimate how roots take up water and nutrients from soil. The results showed that both abiotic stresses reduced the porosity and permeability of the rhizosphere when they worked in isolation. Their combination could reduce rhizosphere permeability by threefold.

The second experiment was to quantify the structural change in soil aggregates following land use changes 70 years ago in long-term experiment at Rothamsted Research. Soil samples were taken from the topsoil in a field under different land usages: continuous grass, arable and fallow, for more than 70 years. I then scanned them using X-ray CT at a resolution of 1.5 microns. Image analysis showed that the land usage change has a significant impact on intra-aggregate structure in that the soil under continuous grassland is more porous while the soil having been fallowed for 70 years is least porous. Based on the X-ray images, I also analysed how the cropping systems affect the ability of soil to retain (water retention curves) and conduct water (permeability), as well as to move nutrients (diffusion coefficient). All these have direct implications for improving our understanding of root uptake of water and nutrients as well as hydrological cycle.

Table of Contents

List of Figures

Chapter 1 Introduction

1.1 Background

Soil is the most complicated biomaterial on the earth. It not only produces foods to feed a growing global population which is projected to increase to 9.7 billion by 2050 (Affairs, 2017), but also offers numerous ecosystem services that might be less known to the public. For example, soil stores a massive amount of carbon which is estimated to be more than the carbon in atmosphere and ocean combined (Cullen and Boyd, 2008). Depending on management, the soil could either become a carbon sink or source. For example, a study on the UK revealed that over the past century, the UK soil has been losing carbon at an average annual rate of 0.6% (Young et al., 2016). It is generally accepted that converting grassland and forests to arable land for agricultural production leads to a loss in soil carbon. For example, in an experiment lasting for more than 50 years, converting grassland to arable land had reduced carbon in the top 0-20 cm soil, while fallowing the soil reduced carbon in topsoil even more (Gregory et al., 2016).

1.2. Soil and soil carbon

Carbon in soil is dynamic changing temporarily. Input of plant roots and straws left-over after harvest increases carbon stock in soil, while in the meantime microbial decomposition of organic matters reduces soil carbon. As microbial activity in soil is affected by a combination of numerous biotic and abiotic factors such as soil water content and temperature, the carbon input rate and its microbial decomposition rate are unlikely to be in

equilibrium always (Castro et al., 2010). Microbial respiration associated with its decomposition of soil organic matter is one of the main sources of the increase in carbon dioxide in the atmosphere - a mechanism underlying global warming. The increase in atmospheric carbon is partly due to microbial activity in soil (Lipson et al., 2005). For example, Stout et al. (2016) found that soil respiration accounts for a large proportion of carbon dioxide released into the atmosphere (Bill A. Stout, 2016). Bacteria and archaea, known as prokaryotes, constitute a large proportion of microbial biomass in soil, and their respiration releases carbon dioxide into the atmosphere at a rate depending on a multitude of biotic and abiotic factors such as soil temperature and moisture. In general, soil respiration increases with temperature if temperature does not exceed an extreme value (Morán et al., 2017). In contrast, the impact of soil water content on soil respiration is more complicated but less studied (Orchard and Cook, 1983).

Soil carbon consists of soluble carbon and soil organic matter (SOM) with the latter referring to carbon in microbial biomass and litters originating from plants (Condron et al., 2010). SOM is essential for soil fertility and health, including retaining water and controlling water movement in soil (Rousseva et al., 2017). Since soil is a major carbon storage, developing new agronomic practices to improve soil carbon sequestration is critical to mitigating climate warming and constructing sustainable agriculture (Dignac et al., 2017). Apart from its importance in mitigating climate change, experimental results also found that enhancing soil carbon sequestration also improves crop yield and physical and biochemical properties of soil (Tanveer et al., 2019). Soil carbon exists in in different forms and based on

its bioavailability to microbiome, it can be divided into labile and recalcitrant carbon (Saljnikov et al., 2013). Labile carbon is carbon that is readily to be taken up by microbes, including amino acids and simple carbohydrates, while recalcitrant carbon refers to those that are difficult to be degraded by microbes, including humic acids and polysaccharide (Stott and Martin, 1989). The distributions of SOM and microbes in soil are spatially heterogeneous (Peth et al., 2014) and in most circumstances, the microbes need to secret extracellular enzymes to solubilize the SOM to acquire the nutrients, predominantly carbon, nitrogen and phosphorus, they require (Jacoby et al., 2017). Since the extracellular enzymes and solubilized nutrients move in liquid water which in turn is modulated by soil structure, recently studies found that it is soil physical structure rather than soil enzymes and soil microbial communities that controls carbon cycle and soil respiration (Schimel and Schaeffer, 2012). For example, a recent review by Dungait et al. (2012) showed that the mechanisms underlying the protection of soil SOM from decomposition is its accessibility to microbes rather than the recalcitrance of the soil carbon due to the impact of soil physical structures.

The change in SOM is affected by a multitude of interactive biotic and abiotic processes including soil texture, climate and land usage (Poulton et al., 2018), which vary with scales. At local scale, agronomic practices such as tillage, fertilizations and cropping system play a key role in controlling soil carbon dynamics and its microbial decomposition (Dignac et al., 2017), white at large scale, it is the topography and climate that determine carbon storage in soil (Garcia-Pausas et al., 2007). For example, Carey et al (2016)found that the response of SOM to temperature at large scale varies with biomes in that soil respiration in desserts and

northern shrubbery increased exponentially with temperature, while in temperate agriculture soils, grasslands and all non-desert biomes, soil respiration increased with temperature asymptotically - increasing first followed by a decline after temperature exceeded approximately 20 ℃. At local scale, the most important factor affecting soil carbon dynamics is tillage and fertilization. For example, the Rothamsted long-term Winter Wheat experiment showed that changing fertilization to composted farmyard manure more than 170 years ago increased the soil carbon content from 35 t ha^{-1} to more than 82 t ha^{-1}, while fertilization using inorganic fertilizers did not alter soil carbon at significant level (Johnston et al., 2009). Tillage also affects soil carbon significantly. For example, there are researches in the literature reporting that reducing tillage or no-tillage could increase SOM because the reduced disturbance to soil reduces soil aggregation and C decomposition (West and Post, 2002). However, this does not appear to be consensus as some studies showed that a change in till age did not always lead to a significant change in soil carbon (Luo et al., 2010). It is generally accepted the impact of tillage on soil carbon depends on soil texture.

Soil carbon exists in different forms and is affected by many physical and biochemical factors. Its measurement is expensive and tedious (Krishna, 2013). Over the past decades, there has been an increase in use of near-infrared reflectance spectrometers (NIRS) to measure soil carbon. The principle of NIRS is that the reflectance spectra by soil is related to the content of soil water and organic matter (Bowers and Hanks, 1965). The NIRS can generate photons; detecting the photons scattered by different components in a soil enables us to measure the relative content of these components. The NIRS can non-destructively

measure different soil properties in the field (Yang et al., 2012). For example, Krishnan et al (1980) used two wavelengths to measure soil organic matter, and Dalal and Henry (1986) used it to measure total soil C, N and soil moisture content. Another advantage of NIRS is that it is able to measure massive data in a relatively short period of time. For example, Chang et al measured 12 soil properties, including total C and N and soil moisture, of 802 soil samples in a matter of week (Chang et al., 2001). It is anticipated that with the accuracy of the NIRS improving, its application will substantially improves our understanding of soil turnover and its determinants, as well as soil carbon modelling to predict the feedbacks between global warming and soil carbon.

1.3. Soil and hydrological cycling

Apart from mediating carbon, soil also helps purify water and decontaminate pollutants in soil via either physical and chemical adsorption or microbial degradation. When pollutants flow with water in soil, they could be trapped to small pores, thereby reducing their leaching to groundwater. In the meantime, their chemical adsorption by soil could also purify water as the surface of most soil particles are negatively charged due to the existence of clays minerals and organic matter. While negatively charged anions such as nitrate cannot be adsorbed, cations such as sulphates and phosphates can form a strong bond with soil particles to become immobile (McLean and Bledsoe, 1992). For instance, phosphates undergo a chemical reaction with soil to form covalent bonds with clay minerals. Other cations, such as heavy metals, could also be adsorbed by soil, thereby becoming less mobile. All these impede the movement of pollutants from soil into groundwater (Wuana and Okieimen, 2011).

Soil microorganisms also play a critical role in water purification. For example, fungi and bacteria can transform nitrate into nitrogen, thereby reducing its leaching to surface water and/or groundwater (Kallenbach et al., 2016). Some bacteria are capable of decomposing oil spilt into less harmful substances such as carbon dioxide and water. Soil microbes not only decompose organic pollutants but also inorganic contaminants (Masciandaro et al., 2013). For example, soil in wetlands is in the anaerobic condition where nitrate can be transformed into nitrogen gas and nitrous oxide via denitrification. While this might increase greenhouse emission, it reduces nitrate contamination to watercourses (Thorslund et al., 2017).

Wetlands and riparian lands are natural water purifiers and could remove more than half of metal ions from entering the watercourse, apart from filtering sediments in surface runoff emanating from rural and urban lands(Liu et al., 2011). Most heavy metals, such as lead and mercury, have a detrimental impact on human beings (Godwill et al., 2019).

In addition to purifying water, soil also plays a critical role in hydrological cycle (Alberti, 2008). Demand for water in plant photosynthesis creates a water pressure gradient from the leaf to the root, and driven by this pressure gradient, water flows continuously from soil to the leaf through the xylem networks of the plant. Root uptake depletes soil water, which, along with the water evaporated from the soil surface, is an important component in hydrological cycle.

Water enters soil either through precipitation or irrigation. Soil structure determines the amount of water that a soil can store, as well as its distribution, refiltration and movement (Schoonover and Crim, 2015). Water dynamics in soil also depends on soil structure and soil

texture (Easton and Bock, 2016). Sandy soils normally have large pores which facilitate water infiltration, thereby reducing the bioavailability of water for plants to uptake. In contrast, clay soils are characterized by small pores and could develop cracks in dry conditions. After rewetting, water cloud flows through these cracks rapidly (Beven and Germann, 2013). Soil would become waterlogged if it is unable to infiltrate the surface water timely. In addition to parental materials of the soil, topology and agronomic practice also play an important role in soil water movement.

1.4. Soil degradation

Despite the importance of soil in providing ecosystem service, inappropriate soil management has led to severe soil degradation, which in some countries, such as Haiti, even resulted in political crises (Williams, 2011). Soil degradation could occur in different ways, including erosion instigated by wind and surface water flow, nutrient losses and acidification. For example, it was estimated that ploughing the soil layer in China had lost more than 1cm of the top soil over the past century (Li et al., 2014), reducing soil fertility and compromised its ecosystem services. The study of Zhao and Hou (2019) found that deforestation and cultivation in steep slopes is a primary cause of land degradation in China, especially in the karst mountainous areas where converting grasslands and woodland for agricultural production had led to severe soil degradation and soil erosion.

Unmanaged grazing is another cause of land degradation. In western Kenya, for example, livestock grazing and land cultivation are believed to be the major reasons of the land degradation (Wanyonyi and Mwangi, 2016). Apart from agriculture, deforestation also

accelerates soil degradation (Lal, 1996). The increasing demand for wood and fuel has led to land degradation in areas where biomass is the primary source for energy (Berger et al., 2013) such as in China (Deng and Li, 2016), and significant deforestation also depletes soil nutrients.

1.5. Aim and Objectives

Services provided by soil are affected by many integrative physical and biogeochemical processes, but all these processes are controlled by soil structure which in turn is mediated by microbial activity. As microbial activity is driven by plant roots, a change in root activities would shift carbon input soil, thereby altering microbial activity and reshaping soil structure. However, how soil structure changes in response to environment and its consequence for soil functions are currently unknown due to its complexity and the lack of technology to measure it. The aim of this thesis is to break this barrier, systemically investigating root-soil interaction and its consequent impact on soil functions. To achieve this aim, I used laboratory and field experiments in combination with neutron and X-ray tomography. The main objectives are:

- To elucidate how plant changes its roots morphology in response to water and salinity stresses using X-ray computed tomography at resolution of 110μm.
- To quantify how plant under water and salinity stresses, either in isolation or combination, reshapes its rhizosphere using pore-scale simulations and X-ray computed tomography.
- To investigate how land use changes more than 70 years ago reshaped soil structure using X-ray computed tomography at 1.5μm resolution.
- To quantify how the soil structural changes induced by the land use changes affect soil functions in transporting water and substrates.

Chapter 2 Literature Review

2.1 Hierarchical soil structure

Soil is formed by a multitude of biotic and abiotic processes operating at different scales, and its structure is hence hierarchical (Caldwell et al., 2012). For example, root growth can instantly reshape soil structure by compacting its adjacent soil from millimetre to centimetres, while the decay of roots could form large bio-pores. In addition, earthworm burrowing can also create large cylindrical pores in both vertical and horizontal directions (Ruiz and Or, 2018). Physically, wetting-drying cycles induced by root water uptake and irrigation/rainfall fragments soil to create cracks (Krounbi and Lazarovitch, 2014). Biologically, microbial decomposition of organic matter binds soil minerals into aggregates, restructuring soil at scales ranging from one micron to tens microns (Kravchenko et al., 2015). Such complicated hierarchical soil structures allow co-existence of air and water across a wide range of environments, which is the key for all lives in the terrestrial ecosystems (Hall, 2016). It also determines flow and storage of water and nutrients, which is essential to microbial activity and plant growth.

Unlike industrial porous materials packed by granular particles, soil is not randomly structured but self-organized and, to some extent, it can be described as a fractal (Young and Crawford, 1992). Its large pore-wall interfaces provide habitats for microbes. The exchange of water and gases (especially oxygen) between soil and atmosphere at a wide range of conditions is the driving force of all biogeochemical reactions and nutrient cycling taking place in soil, which is the key for soil to provide the ecosystem services as reviewed above.

The hierarchical soil structure was recognized long-time ago, and Tisdall and Oades (1982) systematically reviewed its relationship with microbial activity. Subsequent research since then has shown that the effect of microbial activity on soil structure is particularly strong at scales that regulate air and water flow at a wide range of matric potentials (Tecon and Or, 2017). While microbial activity reshapes the soil structure, the soil structural change due to microbial activity also have a feedback effect on functions and community of soil microbiomes. Such feedback interactions have been termed as self-organization in the literature (Young and Crawford, 2004).

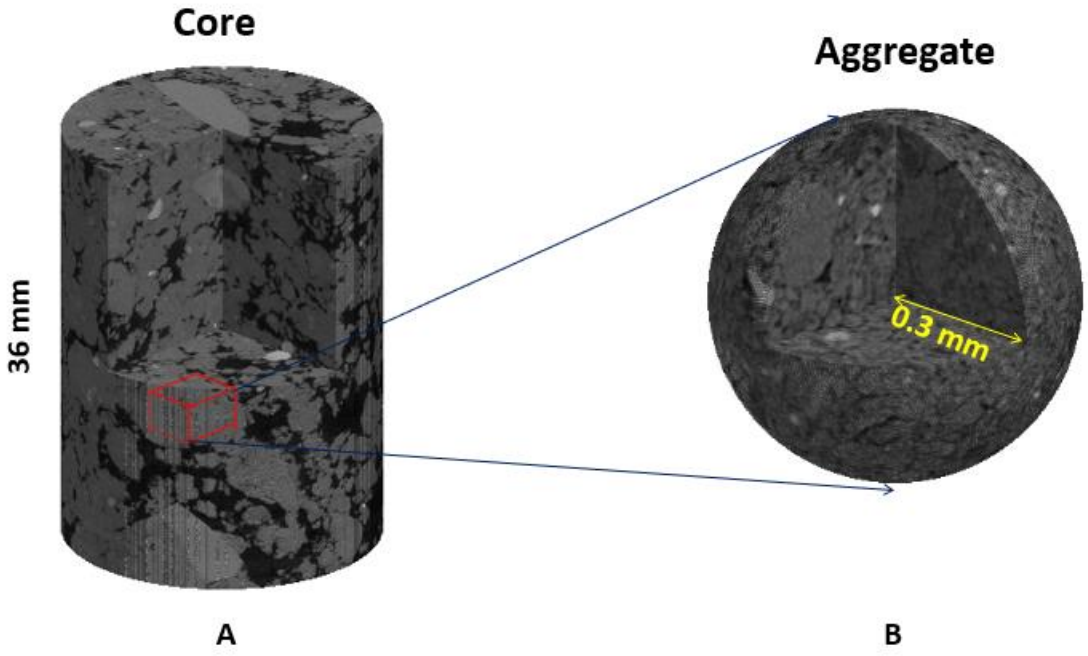

Figure 2.1. Schematic showing the hierarchical soil structured with pores >40μm between the aggregates shown in (A) and pores <40μm inside the aggregate shown in (B).

As an illustration, Figure 2.1 shows a hierarchically structured soil scanned using X-ray tomography at two scales: one at core scale acquired at resolution of 40μm to expose the inter-aggregate pores and the other one scanned at resolution of 1.5μm to visualize the intra-

aggregate pores. Pore structure at the two scales modulates ability of the soil to transport water and nutrients around soil (through inter-aggregate pores) during and following rainfall/irrigation and to retain (via the intra-aggregate pores) water and nutrient when soil becomes dry.

The feedback reactions between soil structure and microbial activity are nonlinear and they are the mechanisms underlying self-organization emerging from soil systems (Young and Crawford, 2004). Self-organized soil structure and its functions emerge spontaneously from soil enforcement against stochastic disturbance of environments, which supports a high level of microbial activity; systems displaying such an organized complexity are irreducible and complicated (Crawford et al., 2012).

2.2 Relationship between soil structure and soil carbon

One key finding in studies on soil organic matter over the past decade is that soil carbon sequestration is not controlled by its molecular complexity as traditionally thought but by its accessibility to microbes (Dungait et al., 2012; Rasmussen et al., 2018). As microbial decomposition of organic matter only proceeds at hydrated sites with co-existence of microbe and oxygen while substrate and water distributions in soil are controlled by capillary pressure (Sessitsch et al., 2001), the turnover of soil carbon is hence modulated by soil structure, i.e., how pores of different sizes are connected spatially. In addition, small pores also functions as a storage for both water nutrition storage, apart from providing habitats to microbial communities (Crawford et al., 2005). Despite the importance of soil structure, our understanding of its relationship with soil carbon sequestration is obscure. This has been

changing over the past decade due to the development of imaging technologies and their application in soil, particularly X-ray computed tomography (CT). There has been an increase in using CT technology to study the relationship between soil structure and soil carbon sequestration. For example, Juarez et al (2013) investigated the impact of soil pore structure on kinetic decomposition of organic carbon based on the pore network acquired from CT, and Kravchenko et al (2019) found that enzymes responsible for dissolving organic matter are associated with a specific range of pores rather than randomly distributed in soil.

Carbon is heterogeneously distributed due to soil aggregation and accessibility of carbon to microbes (Augustin et al., 1995). Soil aggregates are formed from mineral particles bound by fungi and decomposed soil organic matter, and their size varies widely from less than one millimetre to centimetre (Six et al., 2004). The pore geometry inside aggregates varies with aggregate size and carbon mineralization; carbon sequestration in different aggregates is thus different (Yoo et al., 2006). Understanding the relationship between soil carbon and aggregate structure is a key to developing agronomic practices so as to improve soil carbon sequestration.

Soil aggregate is often classified as macroaggregate (bigger than 250μm) and microaggregates (smaller than 250μm) in the literature based on their size (TISDALL and OADES, 1982). Macroaggregates normally contain more carbon than microaggregates (Six et al., 2000), as the former can protect organic matter from rapid decomposition due to its heterogeneous distribution (Lützow et al., 2006; Schmidt et al., 2011). Pore arrangement, characterized by tortuosity, pore connectedness and pore size, is the most important soil

property affecting nutrient distribution and movement of microorganisms in both soil profile and within the aggregates (Tecon and Or, 2017). For example, nutrients normally accumulate in pores with 100–200 μm diameter within sodic clay soil aggregates (Jassogne et al., 2009); Liang et al. (2019) recently found a good relationship between pore sizes in the exterior macroaggregates and soil microbes as well as soil organic carbon (SOC), in which mesopore between 30 and 100 μm is the most suitable habitat in clay for microbes. Pore arrangement is also an important indicator for microbial to access nutrients (Sexstone et al., 1985). Pore size distribution (PSD) is a parameter to quantify the fraction of different pores and affects the ability of the aggregates to protect carbon from decomposition. For example, Ananyeva et al (2013) found that total soil carbon is lower in medium-sized pores than in small and large pores, and that an increase in soil aggregate size reduces soil susceptibility to erosion induced by wind and surface runoff (Liu et al., 2017; Nciizah and Wakindiki, 2014); all these can increase stability of the bonds between soil carbon and soil particles.

2.3 Root and soil-root interaction

Soil aggregate formation is mediated by microbial activity which in turn is driven by carbon input emanating from plant root activities. Plant growth relies on its roots to take up water and nutrients from soil, which is modulated by soil structure. Apart from supplying water and nutrients to sustain plant photosynthesis, roots also function as anchors to stabilize plant against mechanical resistances (Zobel, 2005). The roots thus determine not only the survival and development of plants, but also modify soil structure to optimize water and nutrient uptake (Bengough, 2012). Evolutionarily, roots develop various mechanisms to

facilitate water and nutrients uptake under different environments (Czarnes et al., 2000; Koebernick et al., 2017), and they are plastic to facilitate optimal uptake of water and nutrients even under unfavourable conditions by adjusting their morphology and penetration depth (Smet, 2012). For example, it is well known that under water stress, roots penetrate deep to forage water, while in wet conditions, they ramify in topsoil to explore water (Franco et al., 2011). Similarly, nutrient distribution in soil also affects root growth and branching (Bengough et al., 2011). Apart from water distribution, nutrients also affect development of root architecture. For example, when phosphorus is deficit, plants appear to increase synthetization of root hairs to increase root-soil contact areas as a strategy to improve phosphorus uptake (Lambers et al., 2006). Root formation undergoes different stages in plant development. For example, it is known that maize generates its primary root first at its embryonic stage and as the plant grows, it forms other types of roots including crown roots and root hairs (Abbe and Stein, 1954; Hochholdinger et al., 2004). A change in environment could trigger synthesis of specific hormones to reshape root architecture to facilitate its resources acquisition from soil (Atkinson et al., 2020b; Pandey et al., 2021); it is well established that hormones control adaptation of plant to almost all biotic and abiotic stresses both below and above the ground surface (Dunbabin et al., 2013).

Root and soil interact with each other in a small volume of soil in the proximity of the root which is known as the rhizosphere (Hartmann et al., 2008; Hiltner, 1904). The term of the rhizosphere was coined 100 years ago by (Hiltner, 1904), but its importance in soil functions was recognized only about three decades ago. We now know that the rhizosphere

houses a diverse microbes differing markedly from those in bulk soil (Torsvik et al., 2002; van der Heijden et al., 1998). Apart from their microbial and biochemical difference, the bulk soil and the rhizosphere also differ in their physical properties. Root growth instantly compacts its adjacent soil and destroys some larger pores, thereby leading to an increase in porosity of micropores (Nunan et al., 2006). In the meantime, some root-mediated processes such as root exudation and microbial activity induced by rhizo-deposits enhance soil aggregation, thereby leading to an increase in porosity (Baumert et al., 2018). Also, drying-wetting cycles due to root water uptake and irrigation/rainfall could create cracks and increase the porosity of macropores and soil aggregation (Whalley et al., 2000). As the impact of above biotic and biotic processes on physical properties of the rhizosphere might be contradictory, how roots reshape the structure of their rhizosphere is not conclusive and appears to depend on soil texture and crops. For example, in studying tomatoes grown in coarse and fine soils, Helliwell et al (2017) found that as the plant grew, the porosity of the rhizosphere increased at the expense of the porosity of the bulk soil. In another study, Rabbi et al (2018) compared the porosity and pore connectivity of soil adhered to the roots (i.e., rhizosheath) of drought-tolerant and drought-sensitive chickpeas respectively, finding that the porosity of the rhizosheath of the drought-tolerant increased to 33%, compared to porosity 29% of the bulk soil, and that the pore connectivity of the former was also higher than that of the latter. In contrast, there was no significant difference in porosity and pore connectivity between the rhizosheath and the bulk soil for the drought-sensitive variety (Rabbi et al., 2018). Intensive studies over the past few decades have converged that root growth could

lead to a significant change in physical properties of the rhizosphere through a multitude of biotic and abiotic processes, which in turn modulate how roots acquire water and nutrient from soils, as both water and nutrients need to move into the rhizosphere first before being taken up by the roots (Helliwell et al., 2019) .

The physical structure of a soil determines its ability to transport gases and soluble minerals to and away from the roots (Hinsinger et al., 2009). The roots are also the driving force of soil aggregation, as their associated biotic and abiotic processes bind mineral particles into agglomerates (Kumar et al., 2013). For example, Kaci et al.(2005) found that the rhizobium associated with roots could produce exopolysaccharides to bind mineral particles to form aggregates. In addition, roots themselves also secrete mucilage which is able to reshape the structure of the rhizosphere (Czarnes et al., 2000).

Roots, microorganisms and soil structure interactively react in a process called self-organization, in which a change in one of them could lead to a change in others (Bergmann et al., 2016). The surface of most soil particles and organic matter is negatively charged, and cation nutrients, such as phosphorus, zinc and ammonium, could therefore be absorbed by the soil and become immobile for roots to take up (Violante and Caporale, 2015). In general, plants can only take up soluble minerals from soil. As such, nutrients in organic forms need to be mineralized by soil microbes first before they can be taken up by roots and microbes (Darrah, 1991a; Darrah, 1991b). Apart from fertilizers and mineralization, rhizobia associated with legumes are capable of fixing atmospheric nitrogen for plants they colonize, which is another nitrogen input to soil (Zahran, 1999). Microbial community in soil depends

on plants to supply carbon (Caravaca et al., 2004; Kabir and Koide, 2000). In natural ecosystems, plants and microbes exist collaboratively, with the former providing carbon and energy to the system while the latter exploring mineral nutrients from soil to feed the plants (Bargaz et al., 2018). Plants are also able to change their roots morphology as a strategy to facilitate water and nutrient uptake as a response to soil environment change (Atkinson et al., 2020b). For example, plants in nutrient-poor soils could elongate their root systems and/or increase their root surfaces to enhance their accessibility to nutrients (Rao et al., 2016). These evolutionary adaptations improve allocation of soil resources to plants so as to sustain plant survival and development.

2.4 Tomography technologies and their application in soil-root study

Soil-roots interactions control almost all biotic and abiotic processes in terrestrial ecosystems and support all live on earth, but our understanding of them is limited due to the opaqueness of the soil (Young and Crawford, 2004). The development in imaging technologies over the past decades, particularly X-ray computed tomography and neutron tomography, has started to break this barrier (Mooney et al., 2011). Computed tomography (CT) is a non-invasive technology to visualize interior structure of opaque materials in three dimensions. Cormack and Hounsfield first proposed the method to construct 3D images based on a set of 2D radiographs in the 1960s and won the Nobel prize for this in 1979 (Cantone and Hoeschen, 2011). Since then, CT technology has found applications in a wide range of fields including palaeontology and sedimentary structure (Peyton et al., 1992; Zeng et al., 1996). The early application of X-ray CT in geoscience was to visualize the

development of fractures and variation in materials at microscopic scale (Keller, 1997). The use of X-ray CT in soil science started in the early 1990s, with early interest focusing on pore structural change induced by different agronomic practices and it consequence for ability of the soil to retain and transport water and solutes (Al-Raoush and Willson, 2005; Atkinson et al., 2009; Nunan et al., 2006; Papadopoulos et al., 2009). As its price falls over the past decade, CT has become increasingly accessible to soil research (Baveye et al., 2018).

2.4.1. Principle of X-ray computed tomography

X-ray computed tomography (CT) is a technique to non-invasively visualize interior structure of opaque materials in three dimensions (Taina et al., 2008). Its principle is based on that when an electromagnetic wave passes through an object, its attenuation varies with different materials within the object. Figure 2.2 shows the schematic of a typical X-ray CT scanner; it consists of an X-ray source, a manipulation stage and a detector (camera). The electromagnetic wave emitted from the source is attenuated when it passes through the object on the manipulator. Further attenuation could occur when the object becomes a secondary source of X-ray and produces electrons through atomic interactions (Mooney et al., 2012). Different material in the object attenuates the X-ray differently, and the attenuation can be quantified using an attenuation coefficient μ, referring to the ability of a material to scatter or absorb a wave-particle or a photon. The attenuation coefficient of a material depends on four processes: Compton scattering, photoelectric absorption, Rayleigh scattering, and pair production (Helliwell et al., 2013).

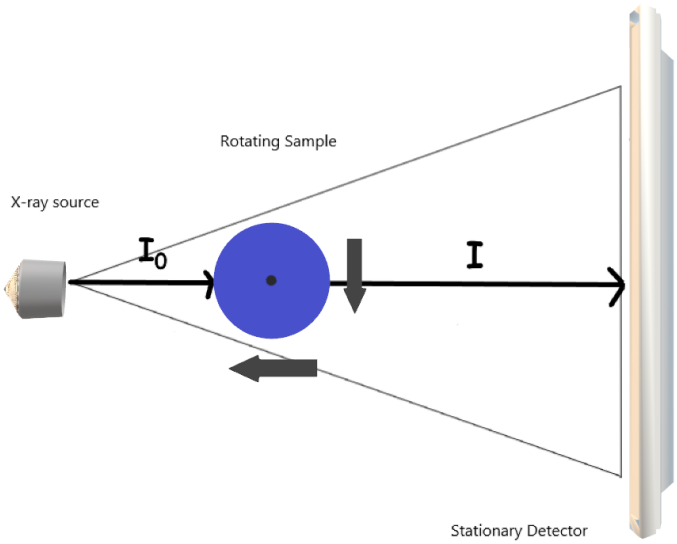

Figure 2.2. Schematic illustration of a typical X-ray scanner and its working principle.

When the X-ray passes through an object thick L as shown in Figure 2.2, its attenuation can be calculated as follows:

$$I / I_0 = \exp(-uL), \quad u = \ln(I_0 / I)/L, \tag{2-1}$$

where I_0 and I are the intensity of the X-ray before entering the object and at the exit of the object respectively, as shown in Figure 2.1, and μ is the attenuation coefficient of the material in the object. If the object consists of M materials and the thickness and attenuaiton coeffcieitn of the kth material are L_k are μ_k respectively, Eq. (2-1) can be modified as follows to describe the combined effects of the M materials:

$$I = I_0 \exp\left(-\sum_{k=1}^{M} \mu_k L_k\right) \tag{2-2}$$

The attenuated X-ray estimated by Eq. (2-2) is captured by a camera as shown in the figure. By rotating the object as illustrated in Figure 2.2, the detector would take a sequence of 2D images of the object from different angles. The attenuation coefficient associated with each

material in the object can be inversely computed based on Eq. (2-2) from these 2D images. For a typical benchtop X-ray micro-CT used in laboratory, the X-ray emits from a point source, and rotating the object 360 degree yields a 2D slice. The three-dimensional structure can be obtained by moving the object up-down to generate a sequence of 2D slices. As an illustrative example, Figure 2.3 shows a 2D slice and a 3D image I scanned and reconstructed using an X-ray micro scanner to be described below.

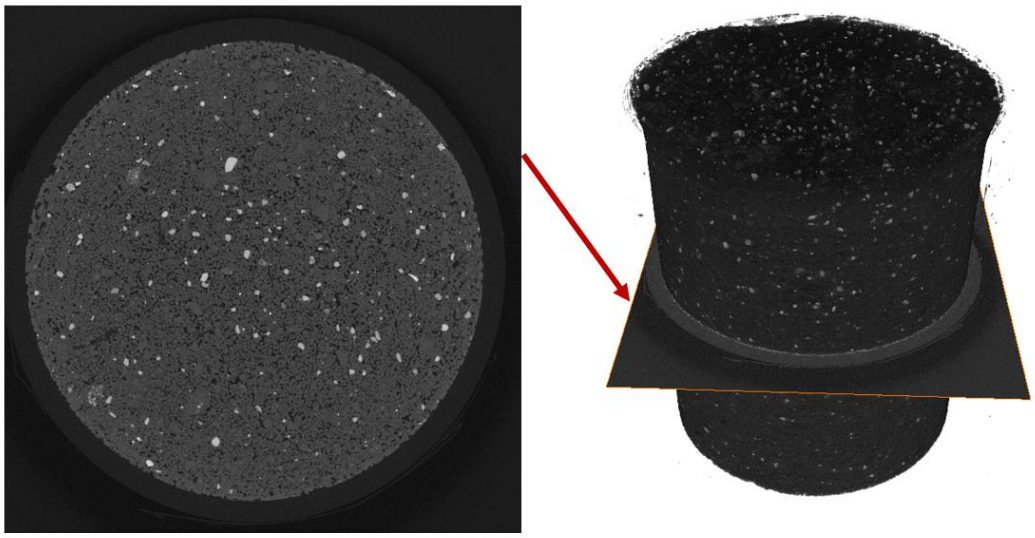

a b

Figure 2.3. A reconstructed 2-D slice (a), and the 3D image constructed by stacking a sequence of 2D slices (b).

2.4.2. Application of X-ray CT in soil structure quantification

Limited by its resolution, early application of X-ray CT in soil was to measure variation of soil density at microscopic scale (Petrovic et al., 1982). Using dual-energy, Rogasik et al. (1999) calculated water distribution in a loam soil with resolution in the 2D slices being 0.25cm × 0.25cm and the distance between adjacent slices being 1mm. Because of the price, the X-ray CT was not widely accessible and its application in soil science was very limited,

with most studies done using medical CT. As such its resolution was not high enough to separate void phase from solid phase although it was able to visualize macropores (Grevers et al., 1989). For example, Mooney (2002) studied the changes in macropore (>0.46 mm) in repacked sand and clay soils, including pore connectivity, continuous pore networks, and consequence for water flow. Rogasik et al (2003) characterized the impact of different cropping systems on macropores, including pore size, pore length and pore connectivity.

Soil macropores provide pathways for water to flow, and understanding their spatiotemporal change is critical to unveiling how agricultural practices affect hydrological cycling. However, soil micropores are equally important as they control how much water a soil is able to retain (Beven and Germann, 2013). The advance in CT technologies over the past decade, especially benchtop CT, has not only substantially reduced its price and made it increasingly accessible, but also improved its resolution. With a benchtop CT, one can characterize the impact of roots on structure of soil within the proximity of the root at great details (Gregory et al., 2003; Perret et al., 2007). For example, Rabbi et al (2018) estimated the change in structure of soil in the proximity of roots of different chickpeas, and found that the structural change in the soil depends not only on soil texture but also on crop varieties. Helliwell et al (2017) found that the porosity of soil in the immediate proximity of roots did not decrease but increased as the root of tomato (Solanum lycopersicum) grew. This is in contrast to traditional view that soil compaction associated with root growth normally densifies soil thereby leading to a decrease in soil porosity, which has been found to increase exponentially with the distance from the root (Helliwell et al., 2019).

Soil is hierarchically structured as shown in Figure 2.1. Because of the trade-off between resolution and sample size in the use of X-ray CT, it is impossible to acquire both macro- and micro-features in a soil simultaneously. To bridge this gap, a commonly used approach is multiscale imaging, in which one uses a low-resolution (30-100 microns) to scan a large sample first and then destroy the sample to scan their aggregates at a much higher resolution (1-10 microns). For example, Bacq-Labreuil et al (2018a) investigated the impact of cropping systems on soil structural change in a sandy loam and clay loam at both aggregate (1.5 microns) and core (40 microns) scales, finding that the impact of cropping systems on soil structure at both scales is not the same but depends on soil texture. Zhao et al (2020) also measured pore characteristics in aggregates taken from alpine meadow, chestnut field and red soil in China at resolution of 7μm, finding that the interior structure in the aggregates was modulated by plant types, temperature and soil texture.

X-ray CT currently is still unable to detect carbon directly because its attenuation of X-ray is not contrasting to that of other constituents in the soil. However, it can be combined with other techniques such as scanning electron microscopy (SEM) to unravel the relationship between soil organic matter and pore geometry within aggregates. For example, Arai et al. (2019) combined SEM and X-ray μCT, and used liquid-phase smium-thiocarbohydrazide-osmium to stain biological materials in soil before impregnating the soil by resin. The stained biological materials were quantified/visualized using SEM, while the pore geometry in the soil was quantified using X-ray CT. Similar technology was also used

by others to quantity the relationship between soil enzymes and pore structure (Kravchenko et al., 2019).

2.4.3. Application of X-ray CT in roots phenotyping

Another application of X-ray CT in soil science and plant physiology is to non-invasively visualize root development and phenotype the roots affected by different agronomic practices (Hodge, 2004). Root traits, including root growth rate, root branching, root surface area and penetration angles, are important parameters determining the survival and development of plants under different environments (Morris et al., 2017). Roots not only take up water and nutrients from soil to sustain plant growth, but they also function as anchors to stabilize the plants against mechanical shear loading. Because of the opaque nature of soil, early study on roots was to excavate the roots and then wash the soil off (Trachsel et al., 2011); such methods are not only tedious but also destroy soil structure and damage the roots (Bucksch et al., 2014). Alternative methods are to grow plants in transparent rhizotrons or in hydroponic culture (Morris et al., 2017). These methods, however, cannot capture the impact of soil, which is crucial for crops growing in the field. The development and application of the X-ray CT has potential to overcome these problems.

Watanabe et al (1992) appeared to be the first to use X-ray CT to study plant roots in soil non-invasively, and Tollner et al (1994) used this method to monitor weekly the development of roots of soybean and Bahia grass in sandy soil cores for three months. Both studies used low-energy CT which was unable to visualise fine roots although it can identify

thick roots in the proximity of the soil surface. In another trial, Heeraman et al (1997) estimated the diameter of bush bean roots using C-ray CT.

Early application of X-ray CT for root phenotyping was limited by its spatial resolution and was unable to identify fine roots (<2mm) which are important for water and nutrient acquisition. The development in X-ray CT technology over the past decade has gradually resolved this limitation (Tracy et al., 2010), and a modern CT is not only able to pick up fine roots but also root hairs with diameter less than 2mm (Mooney, 2002). This makes study of root traits under different environments possible. For example, Mooney et al. (2006) investigated the impact of soil structure on development of roots of cereal with diameter <0.4mm using X-ray CT. Bao et al. (2014) studied the growing angle of root hairs of Arabidopsis, rice and maize under different soil conditions (water content, PH, organic matter) in a loamy sand soil at 22 μm resolution.

The X-ray image of a soil-root system is a sequence of 2D maps, with each pixel represented by an attenuation number. Linking these attenuation numbers to root architecture needs to segment the image, which could be challenging, especially for fine roots (Mairhofer et al., 2015). The early segmentation of X-ray images to discern roots was done independently by end-users, which could result in great uncertainties (Baveye et al., 2010). Over the past few years, various softwares have been developed to specifically separate roots based on their attenuation number and geometrical architecture (Haling et al., 2013b). Open-sources and commercial packages capable of distinguishing roots from soil have become

increasingly accessible, such as Image J, SmartRoot, RootNav and Gia Roots (Galkovskyi et al., 2012; Pound et al., 2013; Quin et al., 2014; Stingaciu et al., 2013; Zhang et al., 2018).

The application of CT has substantially improved our understanding of some fundamental mechanisms underlying root development under different environments such as combined impact of soil density and large bio-pores (Atkinson et al., 2020a), but some limitations remain. One is the trade-off between resolution and sample size. High-resolution needs the sample to be close to the detector as shown in Figure 2.2, which means that the sample must be small enough not to contact the detector during its rotation. Distancing the sample from the detector enables scanning large sample, but it comprises the spatial resolution and cannot identify fine root hairs. Another limitation is to discern the roots from their surrounding materials. The development in CT over the past few years has improved its ability to contrast attenuations of different materials, but soil is a complicated material comprising void space and organic and inorganic materials, some of which have similar ability as the root to attenuate X-ray. Therefore, unless the roots are large enough, distinguishing them in the image is not straightforward. For example, Figure 2.3 shows a rooted pot scanned using X-ray CT at resolution of 110 microns, in which some fine roots and pores were hard to distinguish from each other. If these fine roots are not spatially connected in the images, care must be taken as they cannot be traced automatically even using existing software as mentioned. In some circumstances, manual tracing is required.

2.4.4. The application of neutron computed tomography

The application of X-ray CT has substantially improved our understanding of some fundamental processes involved in soil-root interactions, which would remain unknown otherwise. But its accuracy depends on the difference in attenuations of X-ray between materials in the soil-root system. If the difference in their attenuation of the X-ray is not contrasting, the X-ray CT would not be able to satisfactorily distinguish root from soils. For example, the attenuation of water and soil mineral and organic particles for the X-ray is not contrasting, and it is thus difficult to separate liquid water without doping it in the X-ray images (Van Loo et al., 2014).

Neutron computed tomography (NCT) can overcome this limitation as neurons are sensitive to hydrogen. It has been used to identify roots in soil non-invasively. Figure 2.4 shows an example I scanned using the NCT at the Rutherford Appleton Laboratory (UK) in a soil-filled pot with an internal diameter of 30mm, where the maize roots (dark area) are very contrasting from their surroundings.

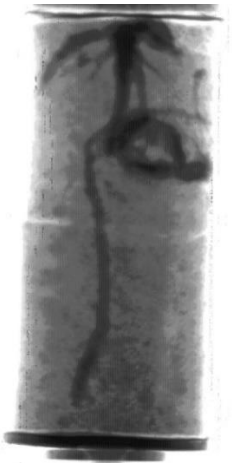

Figure 2.4. Maize root in a soil pot (30mm in diameter) scanned using NCT at the Rutherford Appleton Laboratory, UK.

The principle of NCT is the same as the X-ray tomography (Willatt et al., 1978), distinguishing different materials inside an object based on their difference in attenuating neutrons. It is more accurate in identifying water as the neutron radiation is sensitive to hydrogen. It has been used to quantify root development under different environments as roots are rich in water (Zarebanadkouki and Carminati, 2014). For example, Zarebanadkouki et al (2013) investigated the response of the rhizosphere of lupin to wetting-drying cycles, finding that the rhizosphere held more water when soil was drying while resisting water infiltration when soil was in rewetting. Moradi et al (2011) calculated water content in the rhizosphere of chickpea, lupin and maize after they grew 12 days using NCT; their results showed that the water content in the rhizosphere was higher than the water content in the bulk soil, which is contradictory to traditional view. Another application of NCT is investigation of the change in rhizosphere hydrophobicity following by wetting-drying cycle (Zarebanadkouki and Carminati, 2014), and their results revealed that the rewetting reduced hydrophobicity of the rhizosphere while drying increased it. Mawodza et al (2020) studied development of the 3D root architecture of wheat and water distribution in a sandy loam using NCT, finding that soil macro-aggregates were more moist and that the roots in large inter-aggregate pores were drier than the roots in other regions, implying a possible water leak from the roots in the inter-aggregate pores.

The sensitivity of neurons to hydrogen makes it accurate to identify water, but this also limits the size of soil samples the NCT can scan as an increase in water content and sample size would reduce the depth the neutron radiation is able to penetrate. As an example,

Figure2.5(a) shows the image of maize roots in a soil-filled pot with an internal diameter of 50mm, which I scanned using the same facility as for the image shown in Figure 2.4. The image in Figure 2.5a is blurred and some fine roots were lost even after optimization processes. Comparing Figure 2.4 and Figure 2.5 reveals that increasing the pot diameter from 30mm to 50mm significantly comprised the image quality due to the reasons discussed above.

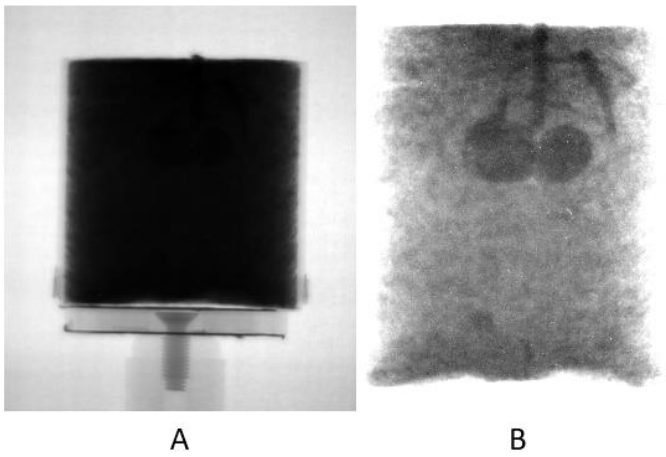

Figure 2.5. Maize root in a soil-filled pot with internal diameter of 50mm. (A) Original radiograph, (B) Processed image after optimization.

2.4.5. Pore-scale modelling

One of important soil functions is its ability to transport fluid and solute in both gaseous and aqueous phases. While it is well known that fluid flow and solute transport in soil is modulated by soil structure, it is impossible to measure in situ, especially aggregates. Modern X-ray CT can visualize interior structure of soil at resolutions less than one micron (Ostadi et al., 2010), but it is unable to visualize fluid flow and substrate transport. As an alternative, the pore-scale modelling could plug this gap (Blunt et al., 2013), and has been widely used to

unravel how agronomic changes alter the ability of soil to transport water and solute (Li et al., 2018b; Zhang et al., 2016a; Zhang et al., 2005; Zhang et al., 2021).

Before tomography technologies became widely accessible, early pore-scale modelling was usually based on simplified medium by idealizing soil as a network consisting of spherical pore bodies connected by cylindrical pores throats, with each pore throat occupied by one fluid only (Blunt et al., 2013; Li et al., 2006). The advantage of pore network model is that fluid flow in each throat can be computed analytically and it is hence computationally efficient. But since the idealized network is not representative of reals soil, it has been gradually replaced by pore network directly acquired using X-ray or other tomography technologies such as focused ion beam/scanning electron microscopy (FIB/SEM).

Tomography invasively captures the pore geometry, but as fluid flow and solute transport are highly nonlinear, simulating them through the pore space of soil at resolution of a few microns is challenging and needs computationally essential method. The development in lattice Boltzmann (LB) method (Chen and Doolen, 1998) and other computational fluid dynamics method (Tartakovsky et al., 2007) has broken this barrier, which can efficiently simulate both single and multiphase fluid flow at pore scale in soil and other porous materials. Over the past two decades, tremendous progresses have been made in developing these pore-scale models, especially the LB model. Their application in soil has resolved some fundamental transport phenomena which would remain unknown otherwise, such as discontinues pressure and solute concentration across an abrupt interface between two contrasting materials (Li et al., 2018b; Zhang et al., 2010), and that hydraulic properties of

the rhizosphere of roots responded differently to crop variety and agricultural management (Rabbi et al., 2018).

Soil is hierarchically structured with pore size ranging from less than one micron to a few millimetres (Bacq-Labreuil et al., 2018b), while the tomography can only capture the pores which is bigger than its resolution. Therefore, strictly speaking, the so-called solid phase in tomography images is porous containing pores less than the image resolution (Bacq-Labreuil et al., 2020). Such pores might not significant for fluid flow because fluid viscosity renders fluid velocity at the pore wall to be zero. As such, the average fluid flow rate across a pore is proportional to the square of the pore diameter (Zhang et al., 2021). In contrast, molecular diffusion on the pore wall is slip and its movement in those small pores that are not explicitly represented in the images could be significant. To account for the impact of such sub-scale pores on solute transport, the so-called grey lattice Boltzmann model had been proposed to bridge this gap (Zhang et al., 2016c). In the grey LB model, the solid phase in the image is assumed to permeable to solute but not to viscous fluid. Fluid can only flow through the void space in the images, while, in contract, solute can move in both the void and the solid phase, with its movement in the void space driven by convection and diffusion while in the solid phase it is controlled by molecular diffusion only (Zhang et al., 2016c).

The focus of my project is to investigate how crop under water and salinity stresses changes the hydraulic properties of its rhizosphere as well as the long-term effect of land use changes on ability of the soil to transport water and substrates. I will hence use the in-house codes developed by Rothamsted Research rather than develop my own codes.

2.5 Summary

Root-soil interaction is fundamental to all life in the terrestrial ecosystem. While most practical interests in terrestrial ecosystems are at catchment and continental scales, it is the physical and biochemical processes occurring at microscopic scales that underpin the phenomena and processes visible and measurable at large scales. Understanding these microscopic processes is hence crucial to improving our understanding of terrestrial ecosystem functions and developing sustainable agriculture; but it is challenging due to the opaqueness of the soil. The development in imaging technologies and their applications in soil and plant physiology over the past decades has gradually overcome these limitations.

X-ray CT has substantially improved our understanding of some fundamental processes involved in soil-root interactions, including both soil structural changes and root architecture development under different abiotic and biotic stresses. Despite the progresses that have been made, many fundamental issues remain elusive because of the complicity in the soil-root system.

Chapter 3. Change in root traits of maize in response to water and salinity stresses

3.1. Introduction

Maize is an arable plant growing worldwide under different climates. It is the most produced crop ahead of wheat. Maize could experience different abiotic stresses when it grows, in which drought (or water stress) appears to be most common in both developed and developing countries. Depending on their function and age, the roots of maize can be roughly divided into primary, seminal roots and root hairs in its early stage (Feldman, 1994; Neuffer, 1994). The primary and seminal roots emanate from the seed embryo, tending to penetrate deep into soil at early stages in order to anchor the crop (Lynch, 2013). As the plant grows, it needs to resist loading and take up water and nutrients to sustain its growth, hence developing crown roots inside the soil and brace roots just above the ground surface (Varney and Canny, 1993). The crown roots grow from the lower nodes of the postembryonic stem, functioning similarly as the brace roots (Hochholdinger et al., 2004). When topsoil is moist, the brace roots penetrate into soil and play a similar role as the crown roots in improving root respiration and forage for water and nutrients (Hochholdinger and Tuberosa, 2009). The development and growth of the primary and seminal roots also depends on availability of water and nutrients. When water and nutrients in topsoil are sufficient, they appear to prefer proliferation in the shallow soil to explore water and nutrients readily available (Koevoets et al., 2016). When nutrients are scarce in soil, the plants grow root hairs to increase the soil-

root contact areas so as to enhance nutrient acquisition, especially when phosphorus is in deficiency (Haling et al., 2013a; Haling et al., 2013b).

Maize could endure a variety of abiotic stresses during its growth, among which water stress is the most common one in arid and semi-arid regions when the available soil water is insufficient to sustain its evapotranspiration (Hutchings and John, 2003). Plant growth requires continuous supply of water and nutrients, and when the plant is under water stress, the reduced soil water could impede the movement of nutrients toward the roots (Fahad et al., 2017). To ameliorate detrimental impact of water stress, maize develops some mechanisms to facilitate water and nutrients acquisition by adjusting its root traits, particularly the crown and brace roots (Lynch, 2013). Typically, it was found that both brace and crown roots can adjust their penetration angle to explore water and nutrients in the subsoil (Vanhees et al., 2020). It is increasingly accepted that maize varieties having “cheap, deep and steep” root traits generally give high yield under water stress (Gong et al., 2015).

Despite the similar physiological roles of the brace and crown roots of maize, their growth and development are well coordinated to avoid competition for the same resources (Comas et al., 2013). For example, brace roots grow into a spatial pattern known as whorls (Hutchings and John, 2003) as the whorl-shape roots are more effective to take up water and nutrients from soil. Compared with the brace whorls, the crown roots grow more horizontally to explore the water and nutrients in the shallow soil (Lynch, 2013). This coordinated combination increases accessibility of the plant to water and nutrients in both shallow and deep soils (Rao et al., 2016). Root architecture of maize varies with soil structure as well

as soil water. Loose soils with high porosity tend to lose water more easily than compacted soil with low porosity under dry condition (Hutchings and John, 2003). For example, loamy soils are more capable of retaining water than sandy soils under dry conditions. As such, the roots of maize growing in sandy soils differ from that growing in loamy soils (Bengough et al., 2011). Maize roots depend strongly on soil water when soil moisture is below the field capacity, although other nutrients might also play an important role (Gray and Brady, 2016). For example, the available nitrogen in soil impacts root morphology, and it found that a nitrogen deficiency could increase the competition between lateral roots for nitrogen thereby increasing root biomass and limiting carbon translocation from the shoot to the roots (de Moraes et al., 2019).

Maize has a strong plasticity to survive under various biotic and abiotic stresses by modifying its root morphology. Understanding the feedback interaction between roots and soils is critical to improving agronomic management. Different methods have been developed to study soil-root interaction either invasively or non-invasively. The overarching objective of this chapter is to investigate the change in key root traits of two maize cultivars under water stress and salinity stress working in isolation or combination.

3.2. Materials and method

The experiment was conducted in a glass greenhouse equipped with ventilation and temperature control systems. We grew different maize cultivars in plastic pots under different abiotic stresses, and after the plants grew for approximately two weeks, we scan the pots non-invasively using the X-ray computed tomography.

3.2.1 Soil and plant

Maize cultivars *Zea mays L* and *var. Delprim* were used as the model plants. We grew them in plastic pots 20cm high with an internal diameter of 15cm, packed with a loamy sand soil taken from the long-term experiment of Rothamsted Research at Woburn, Bedforshire of UK (51.98826°N 0.61942°W). The soil was first air-dried for two weeks after being taken from the field, and it was then passed through a 2mm sieve to remove the debris prior to being packed into the pots at a bulk density of 1.45g cm^{-3}. The soil is classified as Arenosol (FAO soil classification) and the percentage of sand, silt and clay in it was 80%, 12% and 8%, respectively (Nicholson et al., 2018).

The seeds of each cultivar were sown at a depth of 5 cm in each pot and all pots were maintained in a greenhouse controlled at temperature of 25℃, with 14h of photoperiod (06:00-20:00), as shown in Figure 3.1. Three days after sowing, the germinated seedlings emerged. The pots were then irrigated with Hoagland nutrient solution (made from two solutions as shown in Table 3.1) 3, 7, and 11 days, respectively, after the seedling emergence; 14 days after the seedling emergence, we subjected some pots to different abiotic stress, whilst keeping a subset of the pots remained as unstressed controls (CK).

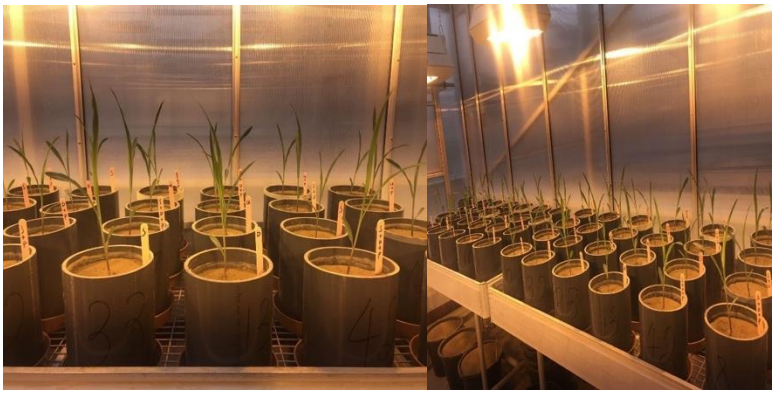

Figure 3.1. The pot-growing plants in a greenhouse at Rothamsted Research.

Table 3.1. The two solutions used to make the Hoagland nutrient solution

Compound	Amount (mM)	Concentration (mM)	Diluted concentration (mM)
Solution A			
$Ca(NO_3)_2 \cdot 4H_2O$	354.22	66.67	2.5
FeEDTA·2Na	11.01	1333.33	50μM
Solution B			
KH_2PO_4	81.65	26.67	1.0
KCl	89.50	53.33	2.0
$MgSO_4 \cdot 7H_2O$	73.94	13.33	0.5
H_3BO_3	1.86	60mL	50μM
$MnCl_2 \cdot 4H_2O$	1.348	60mL	10μM
$ZnSO_4 \cdot 7H_2O$	0.173	60mL	1μM
$CuSO_4 \cdot 5H_2O$	0.150	60mL	1μM
$H_2MoO_4 \cdot H_2O$	0.371	60mL	0.5μM
Note: 1) The pH of each solution was adjusted to 6.0 by adding 1M NaOH. 2) The Hoagland solution was made by adding 20L of distilled water to 750ml of Solution A mixed with 750ml of Solution B.			

On the top of each abiotic-stress treatment and the CK as described above, we added a biotic stress by cutting the leaf at the centre of the crop when it grew to three-leaves stage as shown in Figure 3.2, which will be called as pruning in what follows. Including the CK, there were 4×2 treatments, with water stress, pruning and salinity stress working either in isolation or in combinations. All treatments and their abbreviations are given in Table 3.2.

Table 3.2. The treatments

Treatment	CK	P	D	DP	S	SP	SD	SDP
Pruning	×	√	×	√	×	√	×	√
Water stress	×	×	√	√	×	×	√	√
Salinity stress	×	×	×	×	√	√	√	√

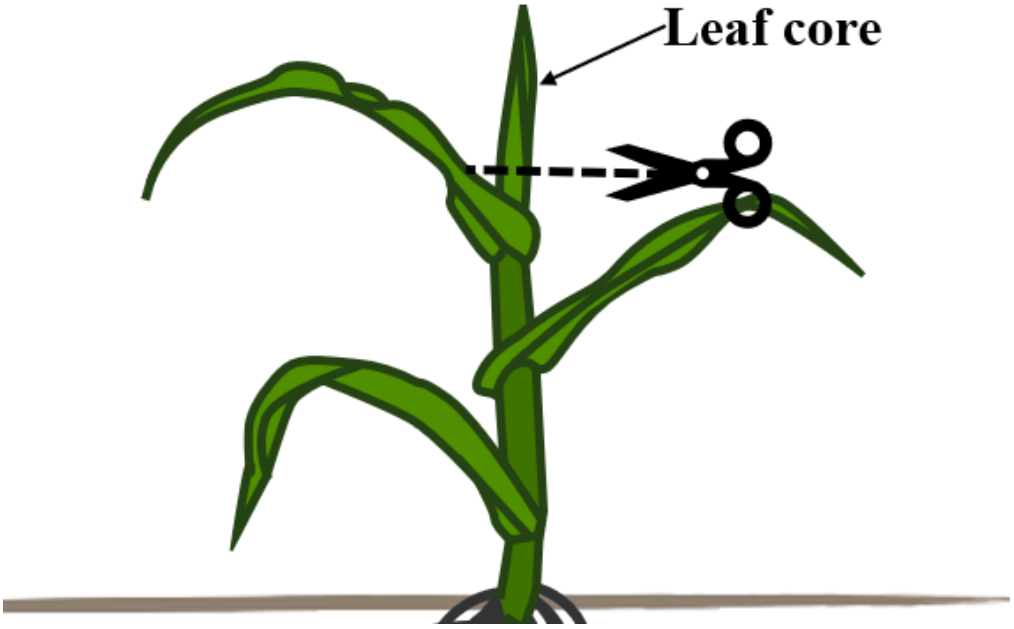

Figure 3.2. Schematic illustration of the abiotic stress – pruning.

The soil moisture in each pot was monitored using a WET-2 sensor connected to a HH2 meter (Delta-T120 Devices, UK). The water stress and salinity were to mimic what the maize grown in northern China often meets (Zhao et al., 2019). The CK - sufficient irrigation - was to add 190 ml of the Hoagland solution to the pot whenever the soil moisture measured using the sensor dropped to 60% of the field capacity (equivalent to 28%, weight content), and the water stress was instigated 14 days after the seedling emergence by adding 90 ml (compared

to 190 ml in the CK) of the Hoagland solution to the pots simultaneously with the CK. The onset of the salinity stress was also at 14 days after the seedling emergence by adding 50 mM of NaCl to the Hoagland solution in the irrigation associated with each treatment.

The time of the pruning varied, depending on plant development, but it was generally between 10 -14 days after the seedling emergence. After an additional two weeks after instigating the abiotic stress, we took all pots in a car boot to the University of Nottingham for X-ray CT scanning using the Hounsfield facility.

3.2.2. X-ray imaging

All pots were scanned using the v|tome|x L system at the Hounsfield Facility in the University of Nottingham as shown in Figure 3.3. The system consists of a greenhouse, a robot and an X-ray CT. The robot is laser-guided and can load a sample weighing up to 80kg on the manipulator in the CT chamber. The scanner is equipped with a 320 kV mini focus X-ray tube and can provide spatial resolution from 70µm to 150µm, depending on the distance between the sample and the camera. As the diameter of our pots was 15cm, the best resolution we could manage to achieve was 110µm. All pots were scanned under 260 kV and 260µA, and it took approximately 30 mins, including sample set-up and scanning, to scan one pot. For each pot, there were 2520 projection images, each taking approximately 250 ms. The raw images scanned from the CT were reconstructed using the software Phoenix datos | x 2 rec. As each pot was rotated 360° (equivalently to scan twice each rotating 180°), the software can use the beam hardening correction algorithm to remove the possible noise that could be caused due to sample-wobbling during the rotation. Once the reconstruction was

free of errors, it outputted a stack of 2D 16 bit grey-scale slices. For all pots I scanned, each had approximately 1820 slices. Due to beamtime limitation, I scanned only 25 pots rather than all the pots in three days.

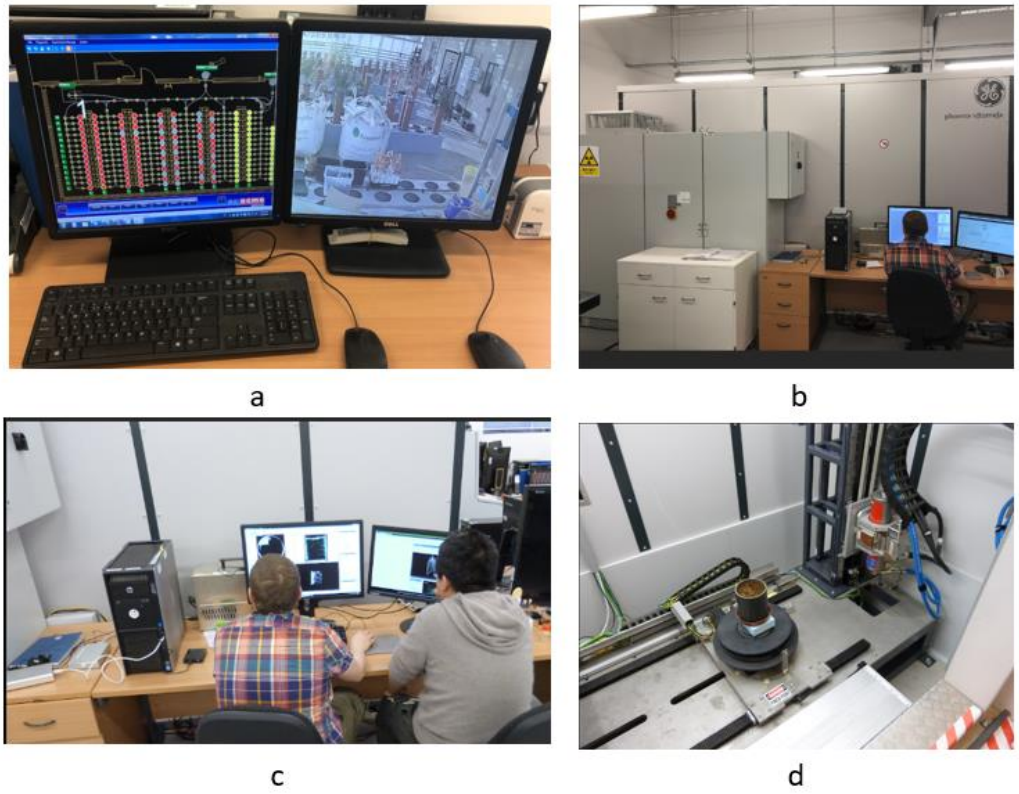

Figure 3.3. The v|tome|x L (modified) X-ray CT system. (a) The monitor; (b) the outlook; (c) the control panel; (d) manipulator in the chamber on which the sample is mounted.

Considering the change in humidity and growth of the plant we left in the greenhouse during the three days, in each scan I randomly selected a pot from the pool. To keep the plane line, I kept irrigation and the abiotic stresses in each por continued until it was scanned. Prior to scanning each pot, I cut the aerial part of the plant in it as shown in Figure 3.4.

Figure 3.4. The plants and their pre-treatment prior to the X-ray imaging.

3.2.3. Image processing

The direct output of the CT scanning for each pot is a sequence of 2D grayscale slices obtained from different heights of the pot, and Figure 3.5a shows one of such slices. The resolution of the 2D slices is controlled by the distance between the pot and the detector as shown in Figure 3.3d. Stacking all 2D slices makes a 3D image as shown in Figure 3.5b.

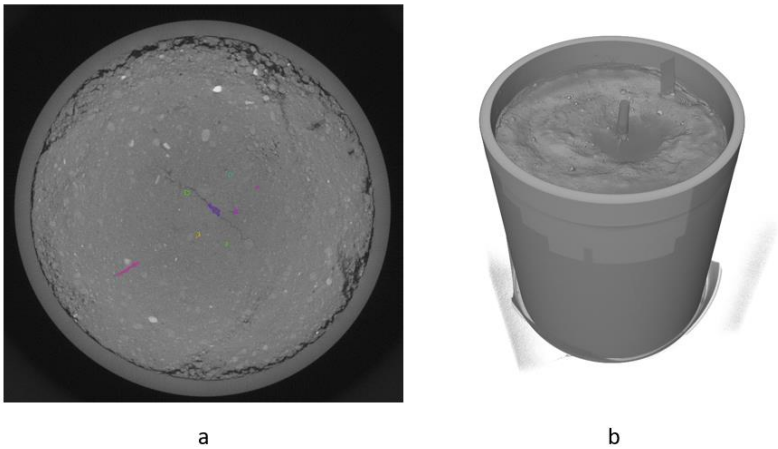

Figure 3.5. A 2D slice (a), and 3D image of a pot (b).

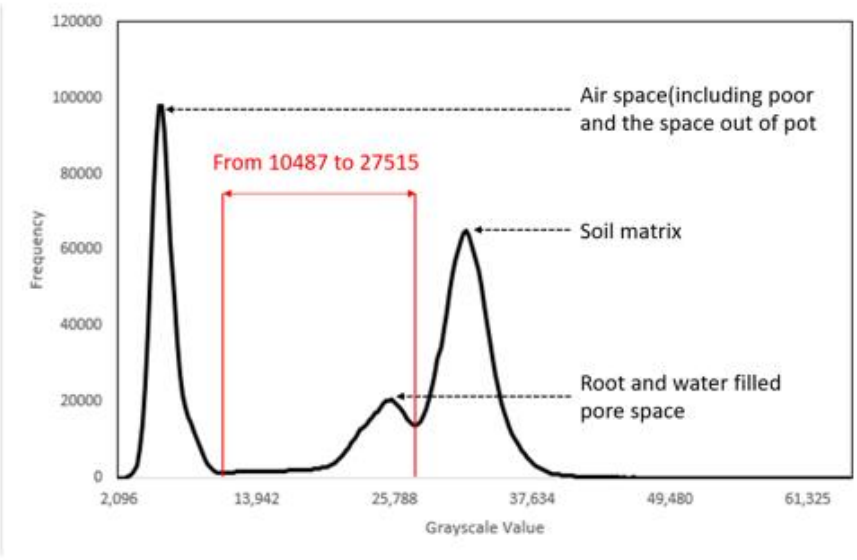

(a)

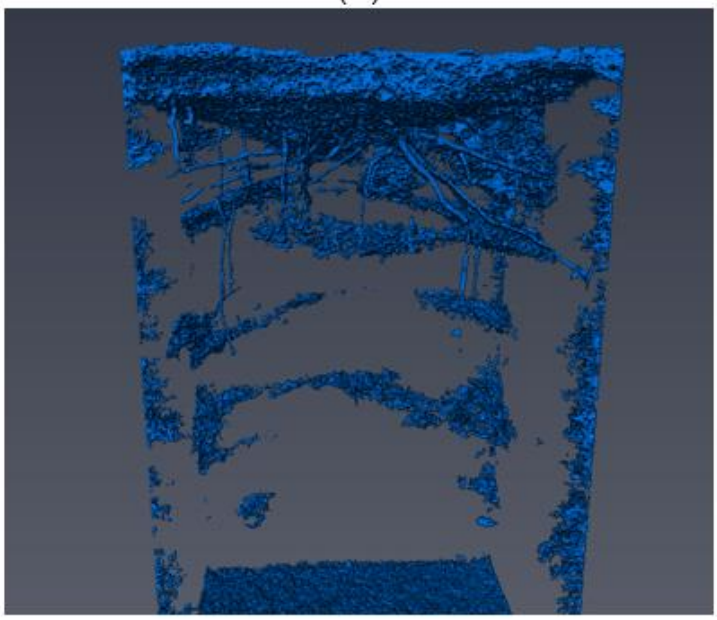

(b)

Figure 3.6. Histogram of grayscale value of all voxels in the 3D image shown in Figure 3.5 (a). Root architecture segmented automatically using the threshold shown in Figure 3.6a (b).

All images were processed using the software Avizo. I first tried to segment the root architecture automatically based on the histogram of the grayscale value of all voxels. In the 16-bit grayscale slices, the grayscale value of the voxels varied from 0 to 65536, with 0 representing the hardest minerals and 65536 representing the gas-filled pores, while the value

in between representing soil matrix or roots. Figure 3.6a shows the histogram of all voxels in the image shown Figure 3.5. It has three peaks: one at 5798 representing pores, one at 20526 representing roots, and the other one at 31957 representing soil matrix. While the pores and soil matrix are distinguishable, the contrast between the roots and the soil matrix is not sharp enough. Taking 20256 as a threshold to separate the roots from the soil matrix and pores, the results are shown in Figure 3.6b. Some roots, especially those in the proximity of the soil surface, are identifiable while others are mixed with the soil matrix, indicating that using the threshold method is unable to map out the root architecture in the pot. I thus used an alternative to segment the roots architecture.

3.2.4. Method to extract the root architecture

A brief analysis of the image shown in Figure 3.5 revealed that the voxel value of the roots depending on their location. The voxel value of the plant stem just above the soil surface shown in Figure 3.7a varied from 10923 to 20852, the voxel value of the roots away from the pot wall in the soil shown in Figure 3.7b varied from 22838 to 29292, and the voxel value of the roots proximal to the pot wall shown in Figure 3.7.c was from 15887 to 20107. Such a variation in value of the root voxels with their locations makes automatic segmentation of the roots based on the histogram difficult.

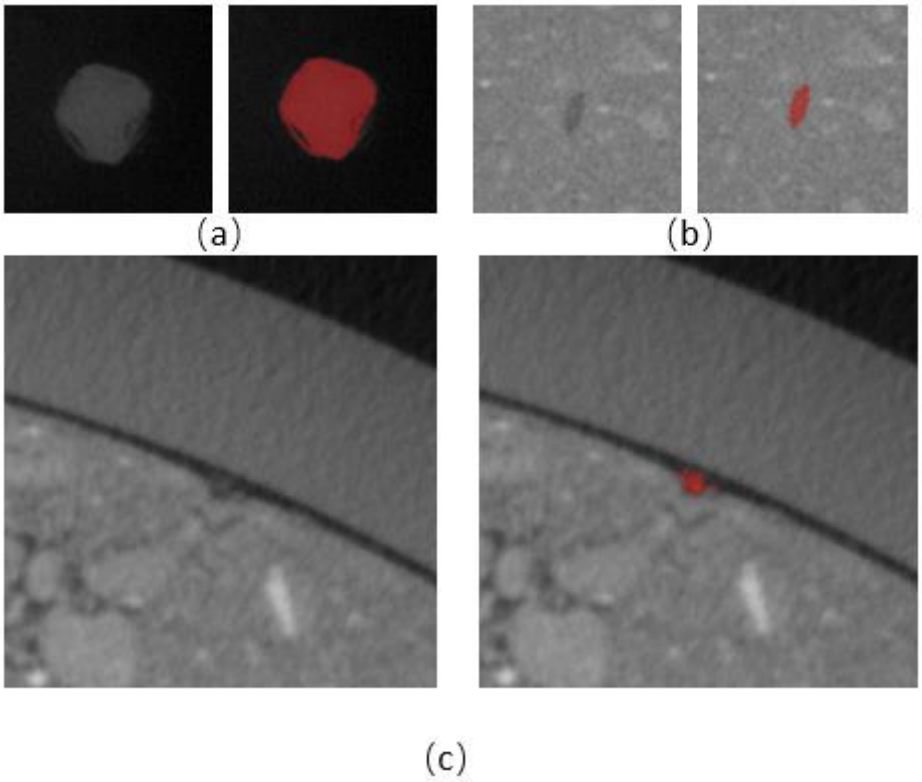

Figure 3.7. Three typical 2D root images for same roots but different position, (a) the plant apart above the soil, (b) primary root in soil and (c) root attach on wall of pot

The method I used to extract the roots is quasi-automatic based on the perception that roots emanating from the stem on the soil surface should be spatially connected. I started from the soil-surface 2D slice with the plant stem as a guidance to trace all roots slice by slice. The 3D root architecture was constructed based on the root traced in all 2D slices. The "segmentation function" in the Avizo was used to identify the root in each slice as it allows identification of the roots in the 2D slices, while in the meantime displaying the results in 3D in a window as shown in Figure 3.8. This helped me to adjudge that no roots have been missing while in the meantime no pores or other materials have been mistaken as roots.

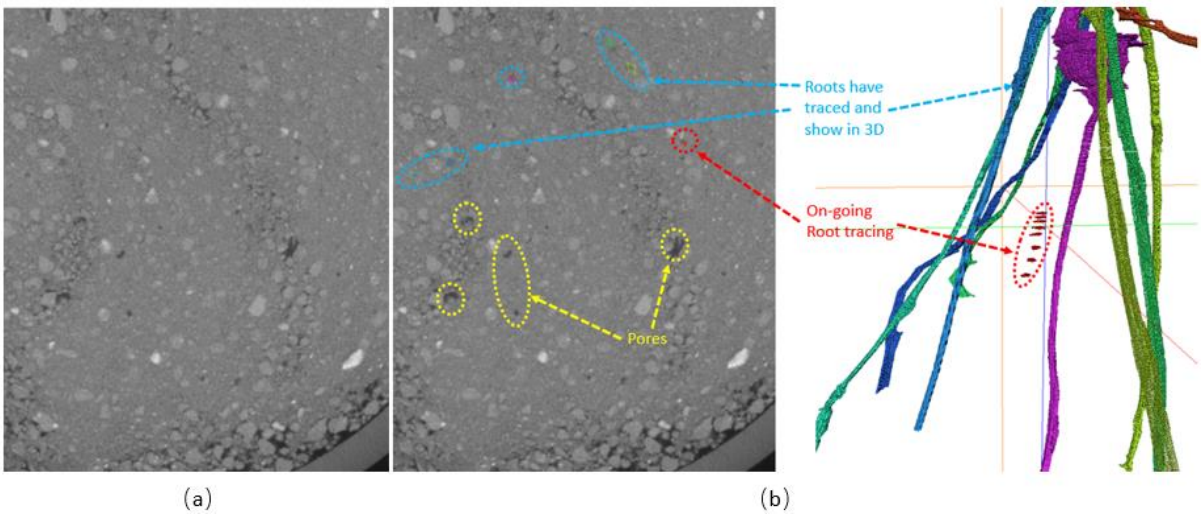

Figure 3.8. Method to trace the roots architecture. Identify roots in 2D slice (a); display the identified roots in a 3D image (b).

Given that the roots were morphologically complicated and that more-than-one roots could cross a 2D slice, one dilemma in tracing roots using this method is to trace all roots slice by slice or trace root by root. A trial-errors found that tracing root by root was more reliable and gave more accurate results. It was also much easier to avoid inadvertently mistaking other features, like the pores shown in Figure 3.8a which have similar attenuation numbers as the roots.

I used a threshold window to separate roots from other features for each 2D slice. In tracing the roots in slices proximal to the soil surface, which were morphologically simpler, the “magic wand” in the Avizo was used to mark the root first by selecting a point or an area on a root-like area; the wand then automatically linked all proximal pixels that have a grayscale value approximately the same as that of the selected point or area. The area generated by the wand could be adjusted by resetting the threshold for the roots as shown in Figure 3.9. When the roots became morphologically complicated in the subsoil with root

branching as shown in Figure 3.10a, the wand method could not separate the pores from the root branches as shown in Figures 3.10b and c. I thus used the brush-method to trace the roots in the subsoil as shown in Figure 10d.

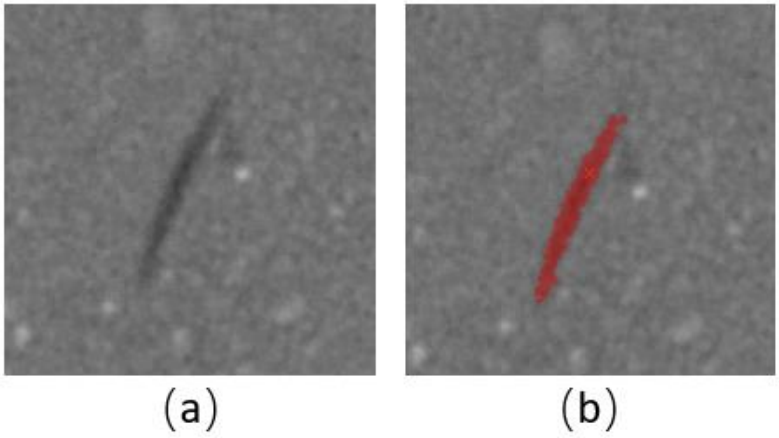

Figure 3.9 Tracing roots using the magic wand. The original image (a); the root identified and labelled (red) using the wand method (b).

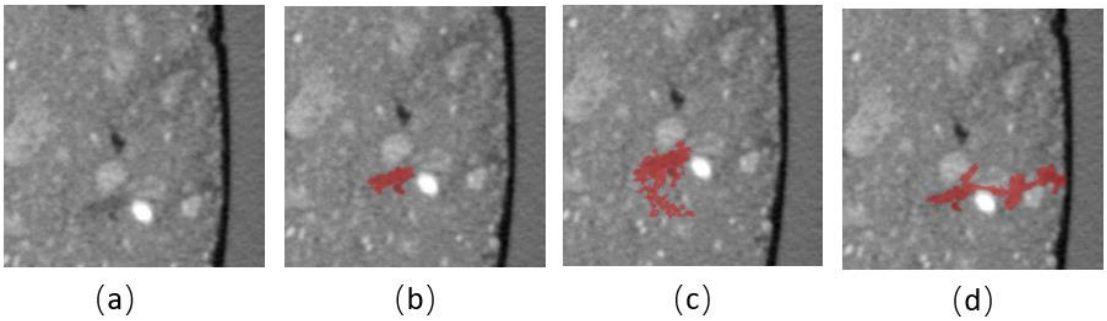

Figure 3.10. Image with root branching (a). Root branching identified by the wand method (b, c), and the root branch identified and labelled by the brush method (d).

Figure 11 explains the principle of the brush method. For an exemplary slice consisting of 17×14 pixels (Figure 3.11a) with grayscale value ranging from 0 to 9, it is assumed that the pixels with grayscale value of 2-4 represent roots. The brush method is to left-right swipe

the slice as shown in Figure 3.11b. The swiping can map all pixels with grayscale value of 2-4 out as shown in Figure 11(c), which, in the X-ray image, were marked as roots.

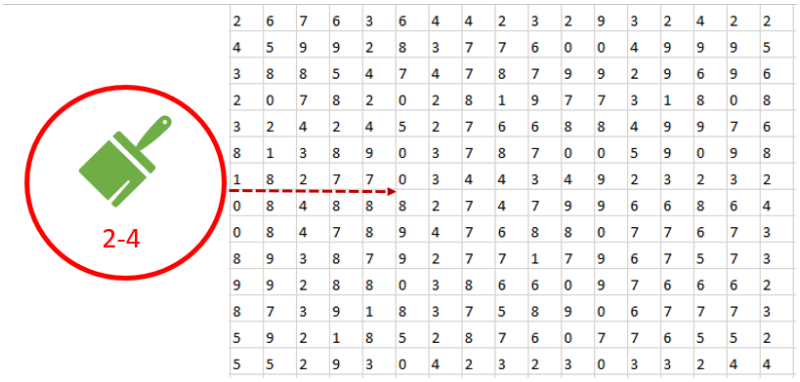

(a)

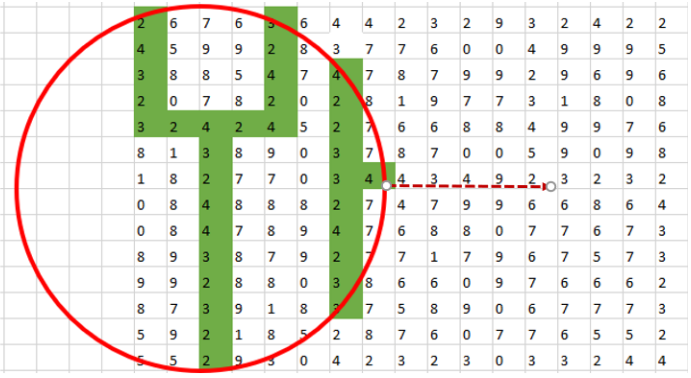

(b)

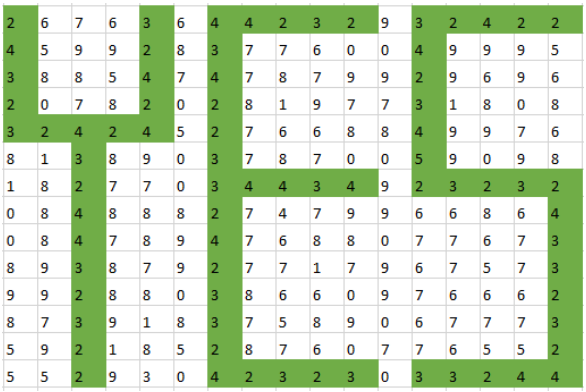

(c)

Figure 3.11. Schematic illustration of the brush method. The original slice (a); brushing the slice from left to right (b), mapping the targeted pixels out (c).

The grayscale values associated with the roots depend on the location of the roots in the soil as explained previously in Figure 3.7. In tracing the roots using the brush method, the threshold values to segment the roots were selected based on these grayscale values. Figure 3.12 shows an example of how the brush method was used to segment a seminal root in a 2D slice. The threshold value for the roots was from 22838 to 29292.

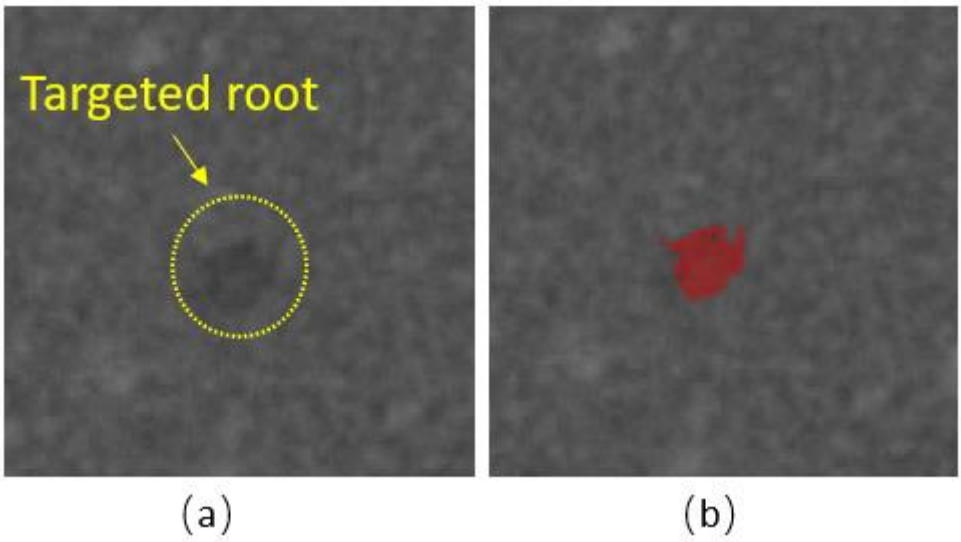

Figure 3.12. Illustration of the brush method for mapping out the roots. (a) The original grayscale slice and the targeted root (area in the yellow circle); (b) the target root mapped out by the brush method.

The 3D root architecture was constructed from the roots mapped out from all 2D slices. Considering the number of slices (approximately1800) of each 3D image and the work it required to identify the roots in each slice, instead of analysing all slices, I selected a number of slices in each image to trace the roots. The separation between two adjacent slices selected for root-tracing depended on the diameter and orientation of the root, ranging from two slices (in areas where the roots were thick or more horizontal) to five slices (in areas

where the roots were thin or more vertical). Figure 3.13 shows four examples: a thick vertical root (Figure 3.13a), an inclined thin root (Figure 3. 13b), a horizontal root (Figure 3.13c) and a bended root that was broken in the 2D slice (Figure 3.13d). As the roots in Figures 3.13a and b are more continuous in the vertical direction, the separation (5 slices) between two adjacent slices for root tracing is longer than that for the more horizontal roots shown in Figures 3.13 b and c.

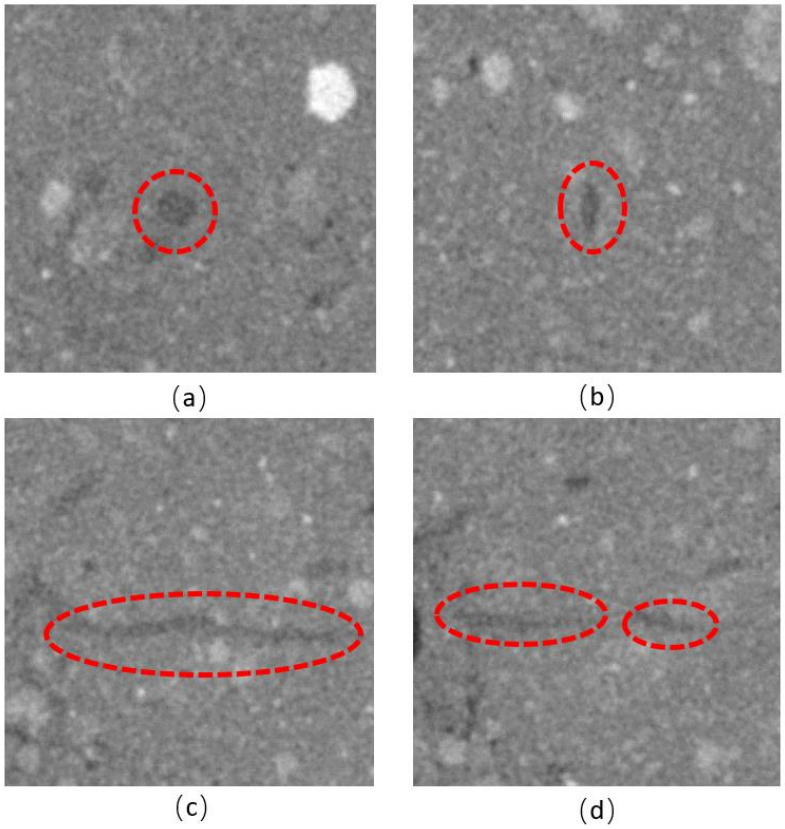

Figure 3.13. The 2D slices show a thick vertical root (a), an inclined root (b), a more horizontal root (c), and a bended root (d).

Root growth was limited to the soil and it could bend once touching the pot wall. Such roots are difficult to trace because the contrast of their grayscale values with their surrounding materials is not high enough as shown in Figure 3.14. Also, the diameter of the

root decreased from its basal to tip. When a root was not thick enough, its contrast with the adjacent materials became blurred in the image due to the limitation of the resolution. While these roots might not be relevant for computing root branching and branching angles, they are important for calculating root lengths. Tracing these roots using the above methods was tedious and I thus used an alternative method to trace them – cylindrical method.

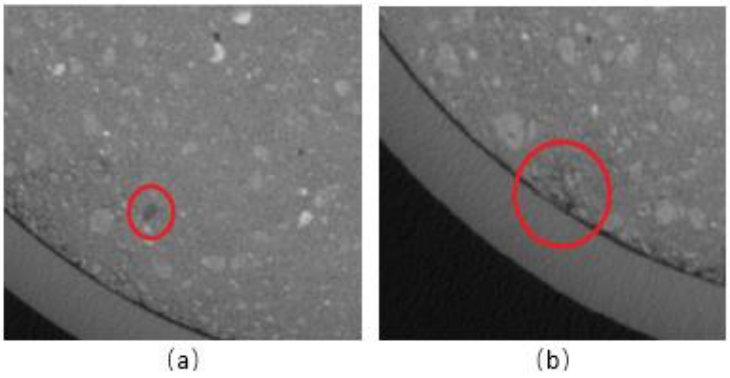

Figure 3.14. Root far away from pot wall (a); root proximal to pot wall (b).

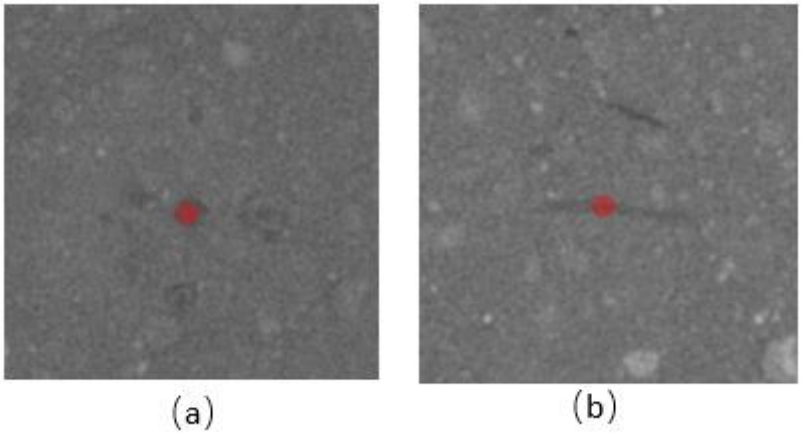

Figure 3.15. Method for racing the root existence using a circle with a diameter of 15 pixels (the solid red circle). Marking a vertical root (a), marking an oblique root (b).

The cylindrical method is to identify the existence of a root rather than its size. For speeding up the tracing process, a circle with a fixed diameter of 15 pixels was used to mark

the existence of any roots in the 2D slice as shown in Figure 3.15. This was equivalent to approximate each root by a cylinder with a diameter of 15 pixels.

The roots traced by both methods were based on a number of selected 2D slices in a pot, and they were spatially discontinuous in three dimensions as shown in Figure 3.16a. The missing root segments were calculated using interpolation as shown in Figure 3.16b. Also, the wand-brush method might create some artificial “bubbles” inside the roots due to the image noise as shown in Figure 3.12b. Such bubbles were refilled once the 3D root network was constructed. As biological functions of different roots in root architecture varied, each root type was marked using different colours as shown in Figure 3.16c and Figure 17.

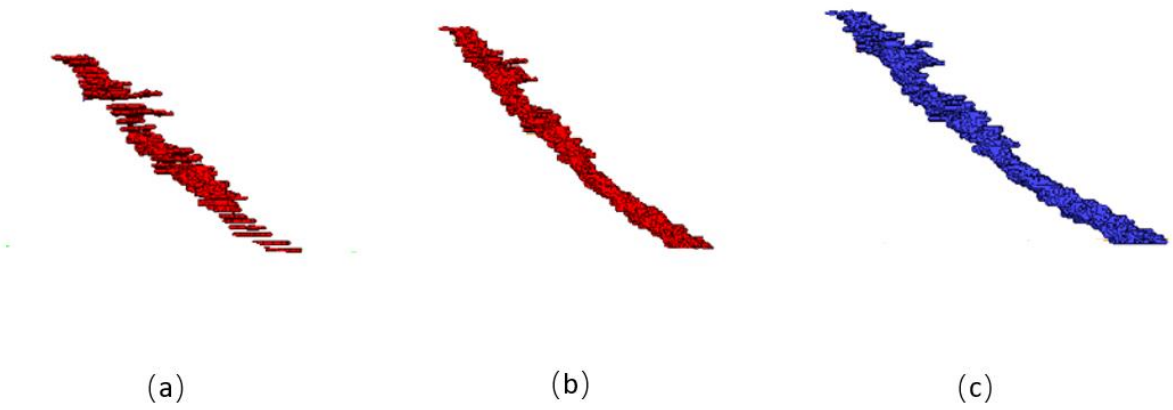

Figure 3.16. The process of constructing the 3D root architecture. Mapping skeleton of a root out from all 2D slices. (b) Calculating the roots in all 2D slices that were skipped during tracing. (c) Colouring-in the root.

The above procedures were applied to all 25 pots, and Figure 3.17 compares the same root architecture constructed by the above two methods. The root architectures of other pots are given in the Appendix at the end of this chapter. Figure 3.17a shows a root architecture

traced using the wand-brush method where the root diameters vary spatially, and they are used to estimate root volume. Figure 3.17b is the root architecture where each root is approximated by a cylinder with diameter of 15 pixels, it is used to estimate root length.

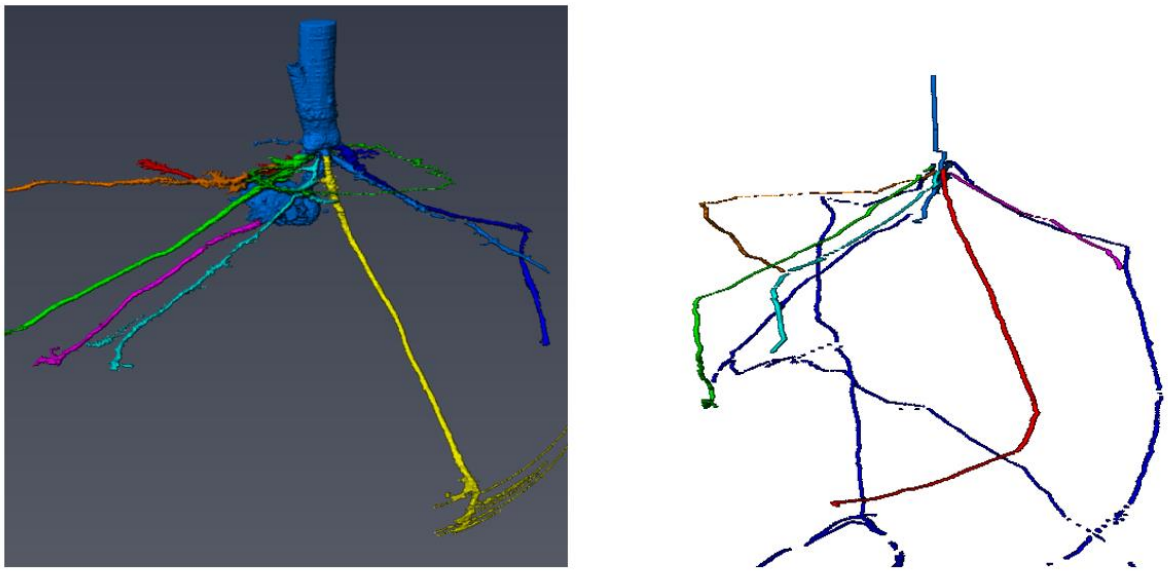

Figure. 3.17. The same root architecture constructed by the two methods. The roots architecture traced with the wand-brush method to calculate root volume (a). The root architecture constructed using the cylindrical method by approximating each root by a cylinder; it is used to estimate root length (b).

3.2.5. Calculating the root traits

Root traits are parameters characterizing root morphology and play an important role in acquisition of nutrients and water from soils by the roots. A change in environment where the plant grows could alert the root traits. Based on the 3D root architecture constructed for each pot using the above methods, the following root traits were calculated: Root angle, root diameter, root length and root depth as shown in Figure 3.18. As different root types have different functions, I separated the roots into crown roots and primary roots and calculated their traits separately. While brace roots are an important root type in maize, our experiment

did not last long enough for them to develop. Therefore, the analysis will focus on the crown and primary roots as shown in Figure 3.18. The root angle and root diameter were calculated based on the root networks constructed by the wand-brush method, while the root length and depth were estimated from the root architecture constructed by the cylindrical method approximating each root as a cylinder.

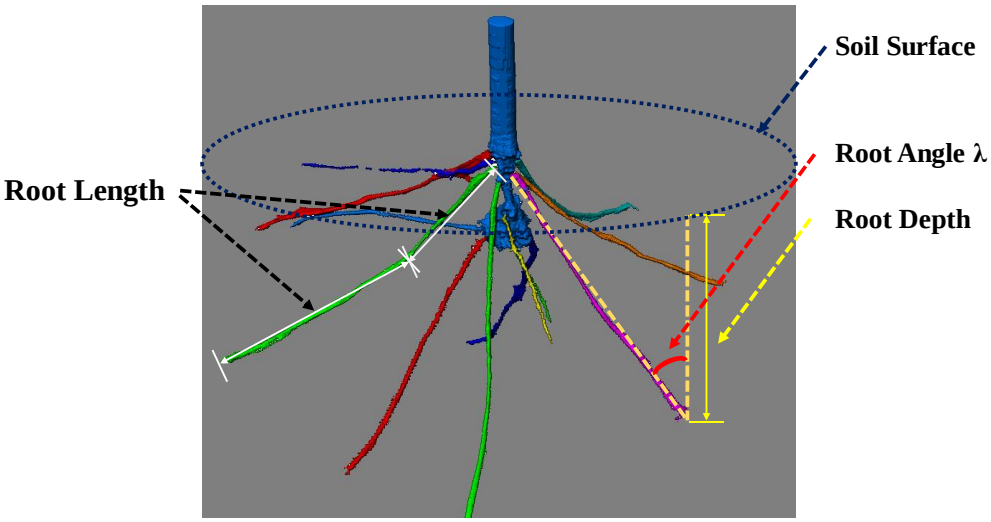

Figure 3.18. Definition of the roots traits I calculated based on the X-ray images.

3.2.5.1. The root angle

The root angle was defined as the angle between a root with the horizontal plane as shown in Figure 3.18. Roots are inherently tortuous, and we approximated it using a straight line to calculate the angle. The angle of each root was calculated by drawing a vertical line from the root tip or its contact point with the pot wall first, and the angle between the vertical line and a straight line used to approximate the tortuous roots λ as shown in Figure 3.18, was calculated from the software. The root angle with the horizontal plane was thus calculated from the following formula:

$$\alpha = 90^{o} - \lambda \qquad (3\text{-}1)$$

3.2.5.2. The root diameter

The diameter of a root varies from its basal to tip, and I used an average diameter to quantify the thickness of the root. Given that the pot wall could change the natural development of the root, for any root that touched the wall, I only considered the part before the root touched the wall in the calculation. The volume of this part of the root was calculated first by accounting the number of root voxels, and its diameter was calculated as follows

$$D = V / L \tag{3-2}$$

where D is the average root diameter, V is root volume and L is the root length.

3.2.5.3. The root length

As each root traced by the cylindrical method was approximated by a cylinder with a diameter of 15 voxels, the length of the root was calculated as follows:

$$L = \delta V / \pi R^2 \tag{3-3}$$

where δ is the size of the voxel (110 microns) and R (15/2 voxels) is the radius of the cylinder used to approximate the roots.

3.2.5.4. The root depth

The depth of each root was defined as the vertical distance from the root tip to the soil surface. It was calculated by finding the root tip first and then drawing a vertical line to cross with the soil surface slice as shown in Figure 3.18.

3.3. Result analysis

Physiologically, maize roots are usually classified as primary and seminal roots, crown roots and roots hairs as different root types have different functions. Figure 3.19 shows their definition. The image resolution was not high enough to capture the root hairs, and in what follows, I will analyse crown roots and primary roots separately.

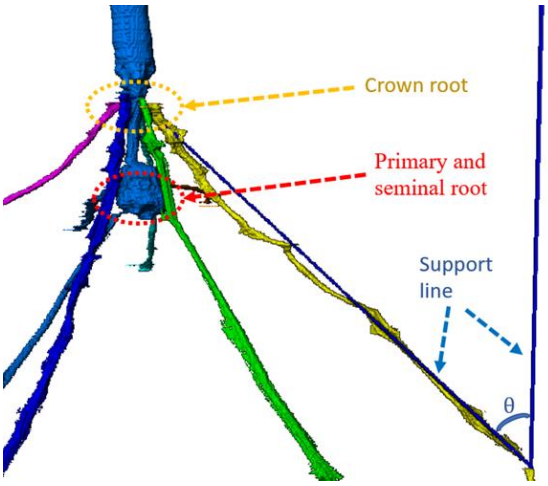

Figure 3.19. Crown roots and primary/seminal roots defined in maize physiology.

3.3.1. The root angel

Figure 3.20 shows the change in root angle with the treatments for the two cultivars. It is evident that subjecting the plants to abiotic stresses alerted the angle between their roots and the horizontal plane. Compared to the CK, water stress and salinity stress working alone reduced the angle of the crown roots from 74.69^{o} to 45.59^{o} and 36.01^{o} respectively for the cultivar *Zea mays L*, and from 50.73^{o} to 37.88^{o} and 25.22^{o} respectively for the cultivar *var. Delprim*. Combining water and salinity stresses reduced the angle of the crown roots further: for the cultivar of *Zea mays L*, combining the two stresses reduced the angle to 37.01^{o}, while for the var. Delprim cultivar, the angle was reduced to 16.99^{o}.

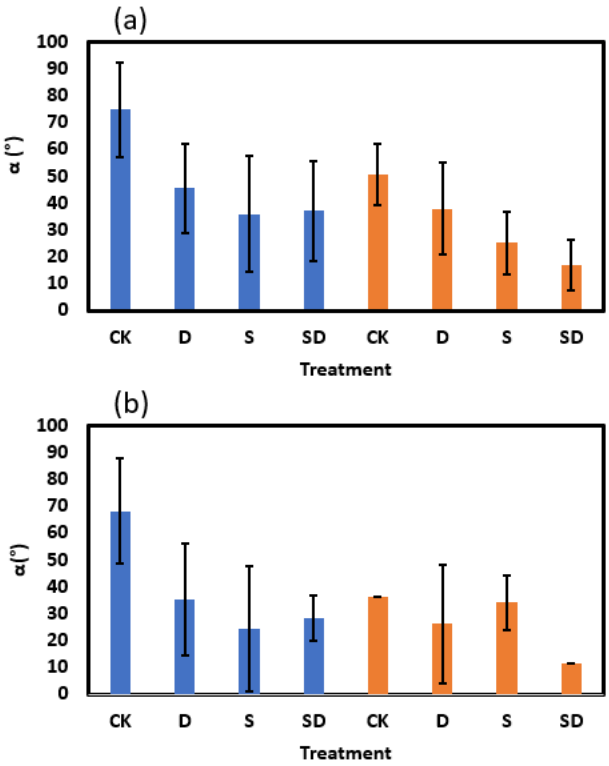

Figure 3.20. Change in root angle with the abiotic stresses. Crown roots (a); primary and seminal root (b). Blue bars and red bars are for the *Zea mays L* cultivar and the *var. Delprim* cultivar respectively.

The impact of the abiotic stresses on the angle of the primary and seminal roots of the cultivar *Zea mays L* was similar as that on the crown roots in that their angle decreased under the stresses. The salinity stress impacted the angle more than the water stress, while combining the two stresses substantially reduced the angle compared to the CK. In contrast, the impact of the abiotic stress on the angle of the primary and seminal roots of the *var. Delprim* cultivar was less significant than on the cultivar *Zea mays L*, in which the angle under salinity stress was comparable with that in the CK, although the water stress and combination of the two stresses reduced the angle.

3.3.2. The root diameter

Figure 3.21 shows the variation in root diameter under different treatments for the two cultivars. For the cultivar *Zea mays L*, the diameter of the crown roots decreased from 2.02mm in the CK to1.56 mm and 1.48mm under water stress and salinity stress respectively, and to 1.61mm under combination of the two stresses. For the cultivar *var. Delprim*, subjecting it to water stress and salinity stress reduced its average root diameter from 2.04mm (CK) to 1.55mm and 1.35mm respectively, while combining the two stresses reduced the average diameter to 1.11mm. These results indicated that the impact of the abiotic stresses affected the crown roots of the cultivar *Zea mays L* more than the crown roots of the cultivar *var. Delprim*.

In contrast, the abiotic stresses increased the diameter of the primary and seminal roots of the cultivar of *Zea mays L* from 1.24mm (CK) to 1.38mm and 1.81mm under the water and salinity stress respectively, and to 1.93mm under the combination of the two stresses. For the cultivar of *var. Delprim* cultivar, the average diameter under water stress decreased slightly from 1.35mm (in CK) to 1.32mm, while the diameter under salinity stress and combination of the two stresses was increased to 1.84mm and 2.09mm respectively.

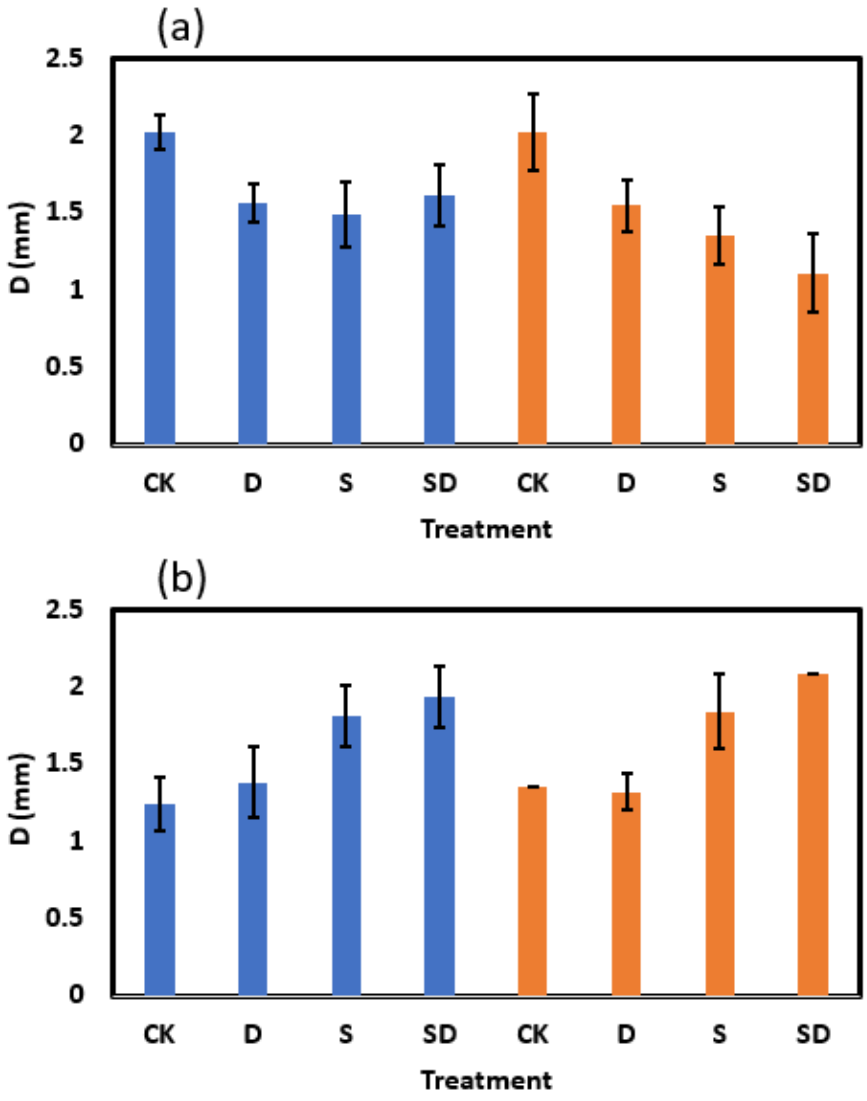

Figure 3.21. Variation in average root diameter with the abiotic stresses. The crown roots (a); the primary and seminal roots (b). The blue bars are for the *Zea mays L* cultivar and the red bars are for the *var. Delprim* cultivar.

3.3.3. Root length

The root length results are shown in Figure 3.22. The root length varied more widely between the replicates than the above two root traits. Salinity and water stress reduced the length of the crown roots. For the *Zea mays L* cultivar, its root length decreased from 108.56mm (CK) to 61.49mm and 73.60mm under water stress and salinity stress respectively, while for the *var. Delprim* cultivar, its root length decreased from 91.12mm (CK) to

82.75mm and 70.30mm respectively under the two stresses; combining the water and salinity stresses reduced the root length of the former and latter cultivar to 78.84mm and 76.78mm respectively.

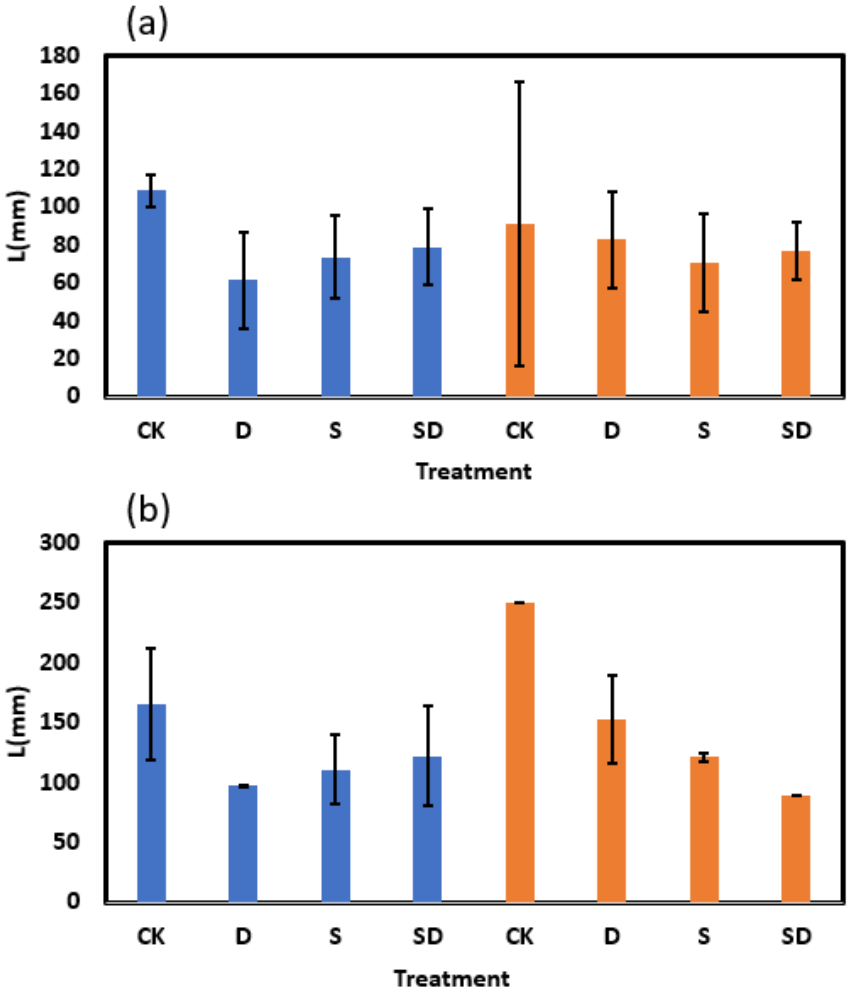

Figure 3.22. The average root length. Crown roots (a), primary and seminal roots (b). The blue bars are results for the *Zea mays L* cultivar, and the red bars for the *var. Delprim* cultivar.

The length of the primary and seminal roots appeared to be more sensitive to the abiotic stress than the crown root length for both cultivars. Without stresses, the average length of the primary and seminal roots of the *Zea mays L* cultivar and the *var. Delprim* cultivar was 164.78mm and 250.15mm respectively. Under water stress, salinity stress and combination of

the two stresses, the root length of the *Zea mays L* cultivar decreased to 97.14mm, 110.51mm and 121.93mm respectively, while the root length of the *var. Delprim* cultivar was shortened to 152.97mm, 121.22mm and 88.33mm respectively.

3.3.4. The root depth

The abiotic stresses limited the penetration depth of the roots of both cultivars, and Figure 3.23 compares the results. The *Zea mays L* cultivar appeared to be more sensitive to the abiotic stresses, with its crown roots penetrating to 43.9mm deep under water stress, 47.94mm deep under salinity stress, and 47.45 under deep under combination of the two stresses, compared with the root depth of 104.71mm in the CK. In contrast, the crown roots of the *var. Delprim* cultivar managed to grow to a depth of 50.82mm under water stress, 29.96mm under salinity stress, and 22.44mm under combination of the two stresses, compare to root depth of 70.54mm in the absence of the abiotic stresses.

The abiotic stresses impeded penetration of the primary and seminal roots even more. The average penetration depth of the roots of the *Zea mays L* and *var. Delprim* cultivars in the CK was 153.03mm and 212.22mm respectively, while the water and salinity stresses and their combination reduced the root depth of the former cultivar to 58.15mm, 62.24mm and 77.16mm respectively, and that of the latter cultivar to 106.24mm 81.46mm, and 26.87mm respectively.

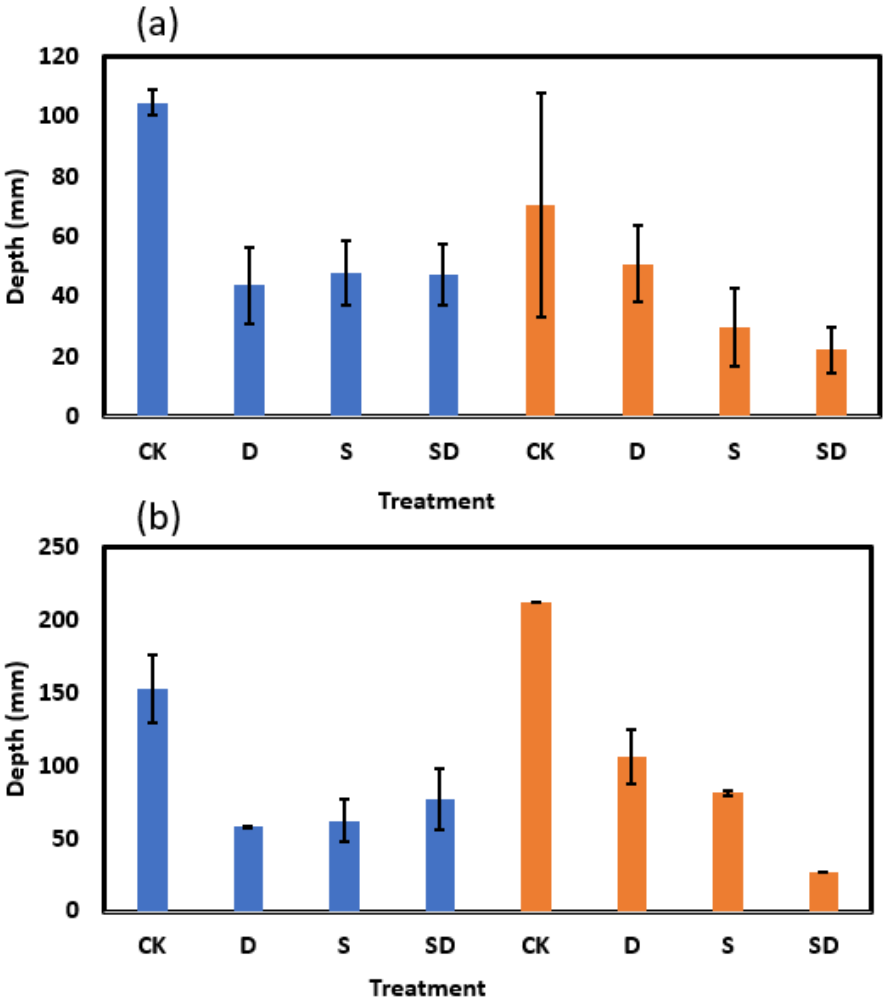

Figure 3.23. The average root depth. Crown roots (a), Primary and seminal roots (b). The blue bars are results for the *Zea mays L* cultivar, and the red bars for the *var. Delprim* cultivar.

3.3.5. The impact of pruning

The response of root traits to pruning was complicated and it is difficult to identify appreciable trends in its impact on primary and seminal roots. We thus only calculated the root traits of crown roots. Figure 3.24 compares the combined impact of the pruning and salinity stress on the root traits of the two cultivars.

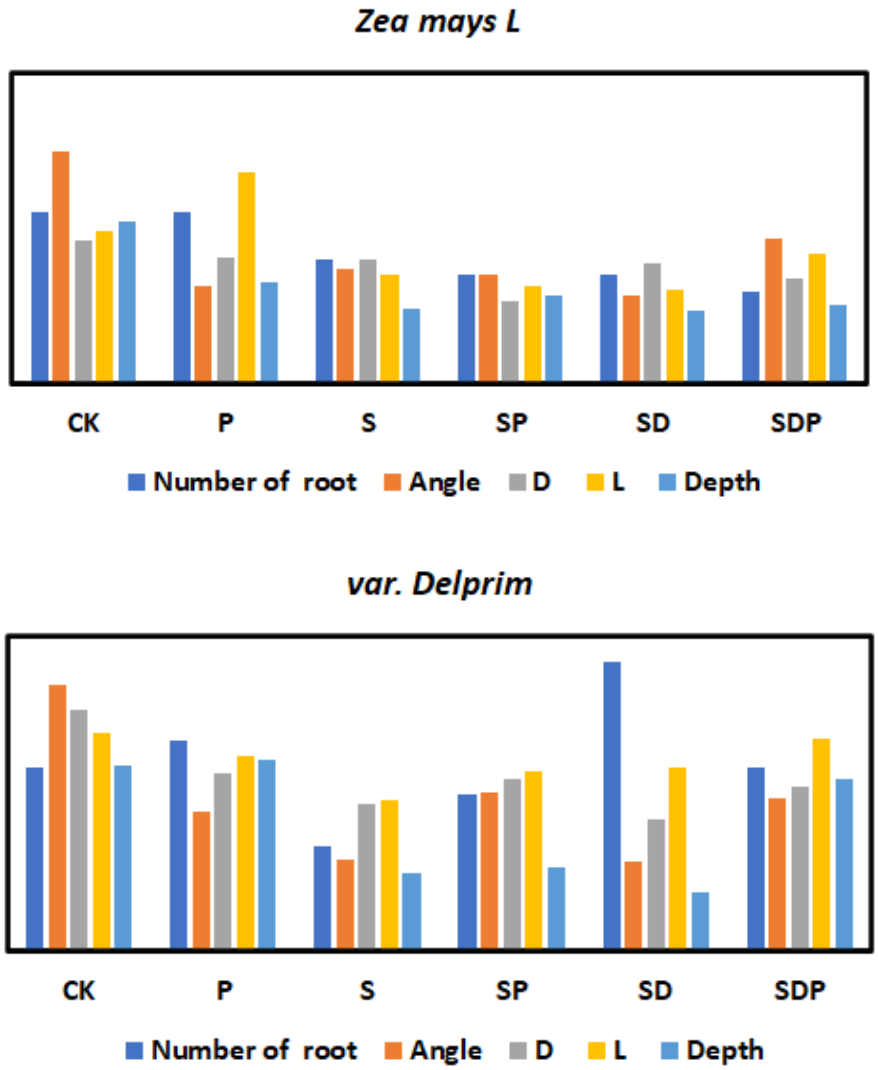

Figure 3.24. The combined impact of the pruning and salinity stress on the root traits of the two cultivars.

The combined impact of the pruning and the salinity stress appeared to be more significant on the *var. Delprim* cultivar than on the *Zea mays L* cultivar. For the *Zea mays L* cultivar, in the absence of water stress, pruning reduced root diameter and root length but slightly increased the number of roots, meaning that the pruning made the plant develop more roots and these roots grew more steeply as the root angles under pruning became steep. Under salinity stress, pruning increased all root traits, including root numbers and root length,

although the root depth remained approximately the same. When the plant was subjected to the combined water and salinity stresses, pruning made the roots grow deep and become longer, but the numbers of the roots were reduced.

For the *var. Delprim* cultivar, pruning reduced all root traits in the absence of abiotic stress, while in the presence of the salinity stress alone, it increased all root traits and made the roots go horizontally. In the presence of water and salinity stresses, pruning reduced the roots number but increased other root traits.

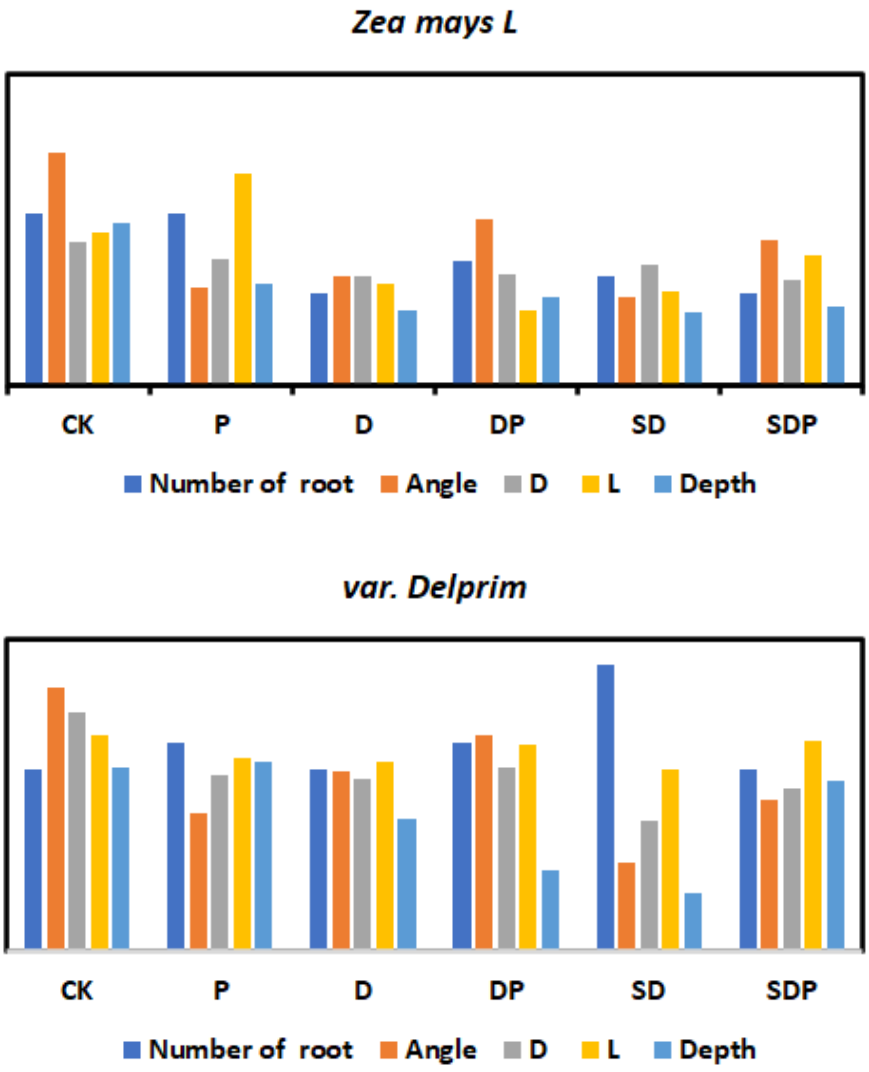

Figure 3.25. Combined impact of pruning and water stress on the root traits.

Figure 3.25 shows the combined impact of pruning and water stress on the root traits of the two cultivars. Compared to salinity stress, pruning the plant when it was under water stress did not bring significant change to its root traits, except the root depth and root numbers of the var. Delprimi cultivar.

3.4. Discussion

The objective of these experiments was to investigate how root traits of maize respond to change in biotic and abiotic stresses during its early growth stage as Peleg and Blumwald (2011) stated that the seedling of maize is most sensitive to abiotic stress and that the formation of its root system at this stage might have shaped their root development in the whole growth season. Figures 3.20 to 3.23 compare four traits of two maize cultivars under water stress and salinity stress working in isolation and combination. The results showed that both cultivars altered their root morphologies and root traits when they were subjected to the abiotic and biotic stresses to facilitate water and nutrients uptake although I did not measure nutrient contents in the soil and plants. A conjecture in the literature is that under water stress, maize roots prefer going deep to explore water in the subsoil (Lynch, 2013; Vanhees et al., 2020), and that cultivars with roots that are cheap to make and can go deep at a steep angle, coined as “cheap, deep and steep”, normally give a high yield under water stress (Lynch, 2013; Vanhees et al., 2020). As directly measuring root development and its architecture in the field is practically impossible, I tested this hypothesis and conjecture using pot experiments with the roots in each pot scanned using the X-ray CT tomography at a resolution of 110 microns. While such a resolution was not fine enough to identify all roots, it

was sufficient to capture the crown and brace roots which are critical for the plant to survive under biotic and biotic stresses.

For both cultivars, subjecting the plants to the abiotic stresses increased the angle of their roots with the horizontal plane, meaning that under water and salinity stress the roots grew more horizontally. This appeared to be contradictory to the “cheap, deep and steep” conjecture as just discussed above. Lynch (2013) rationalized that the roots of maize growing more steeply (i.e., vertically) under water stress is to explore water in the subsoil as in the field it is the deep soil that is moist and retains more water due to the combined impact of gravity (which drains water) and the presence of a groundwater table (which supplies water to soil via capillary force). In the pot experiment, the bottom was impermeable and the water in the soil was from the irrigation and was rich in the soil surface. That is, the topsoil was moister in the pot experiment as opposed to the soil in the field where the subsoil is moister. As an illustration, Figure 3.26 shows a neutron image of a pot planted with maize I scanned using the neutron tomography at the Rutherford Appleton Laboratory IMAT, UK. Although the pot was too big to allow the roots in it to be identified, it is evident that the topsoil was darker than the subsoil, implying that the topsoil contains more water as the attenuation of neutrons by hydrogen in the water makes the image look darker. The reasons why roots in my pot experiments went more horizontally under water stress is because the topsoil was moister and more nutritious, and more horizontal roots could facilitate roots to acquire the water and nutrients. Therefore, my results are physiologically consistent with the conjecture of Lynch (2013).

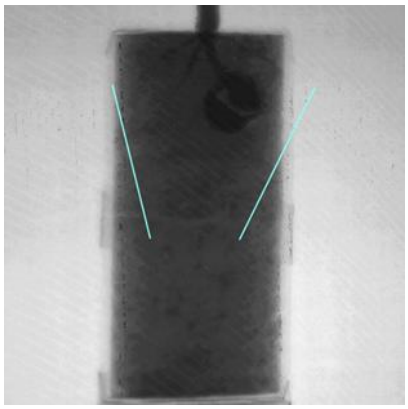

Figure 3.26. An image acquired using neutron tomography shows the topsoil was moister than the subsoil in the pot experiment.

The angle of crown roots varied more substantially than the embryonic root (the primary and seminal roots) because two weeks after the plant grew to the three-leave stage (about 10 to 14 days after seedling emergence), the primary roots had almost established. This was approximately the date when the abiotic stresses were instigated. Therefore, the embryonic roots were less sensitive to the abiotic stresses than the crown roots. However, it is clear that the root angle is modulated by water and salt distribution in the soil. Water and salinity stresses impeded root growth, and both root length and root depth were reduced. These are consistent with previous results showing that salinity and water stresses have a detrimental impact on root growth (Barber, 2014).

Apart from water and nutrients, soil temperature is also a factor that might affect root development (Tollenaar and Wu, 1999). In the field, soil temperature normally rises as soil water decreases. In my experiment, however, the plants were grown in a greenhouse and it was almost certain that the impact of temperature was minor even in the water stress treatment. This treatment could consider a temperature stress treatment because the heat

source is located on the top of the greenhouse, similar to the sun in the field. However, crop roots in the field grow deep where soil is cooler than top soils. Therefore, within an acceptable temperature range, water and salinity stress demonstrate more greater influence than temperature. The root traits changes under different stresses explain that root development is intensively affected by soil environment (Mooney et al., 2011).

Figures 3.24 shows the impact of pruning on root development of the two cultivars under different abiotic stresses. An initial trial experiment in Xinjiang of China revealed that pruning the maize leaves when the plant grows to two- or three leaf-stage could increase its ultimate yield when the plant was under drought, although the underlying mechanisms remain unknown. We anticipated that one reason is that the pruning might have altered root development. Part of our results supported this. Compared with the CK when the plants were not subjected to water stress, pruning the plants only slightly reduced the length, diameter and depth of the roots, with the roots becoming slightly more horizontal. In contrast, when the plants were subjected to combined water and salinity stresses, pruning the plants might ameliorate the effects caused by the water and salinity stress. For example, Figure 3.23 and 3.24 show that the root angles of both cultivars can be ranked in the order of CK>SP>S, CK>DP>SDP and CK>SDP>SD, and the pruning (SP, DP and SDP) made the root angle closer to that in the CK, improving the tolerance of plants against the stresses as a result.

3.5 Conclusion

Using X-ray CT tomography and pot experiment, I, for the first time, investigated the impact of water stress and salinity stress, working in isolation and combination, on root development of two maize cultivars in three dimensions. The results showed that the water and salinity stresses impeded root growths, and the roots grew more horizontally to explore the water and nutrients in the proximity of soil surface following irrigation. Salinity and drought stresses restrict root growth but pruning a leaf when the plant grows to three-leaf stage could alter root growth to improve its tolerance to the stresses. Under high salinity stress or water stress, the maize roots could reduce its hydraulic conductance by up to 80% (Wang et al., 2020). Pruning the plants reduced its demand for water and other nutrients due to the reduced photosynthesis, and might hence temporarily improve resistance of the plant against the stresses.

Different plants respond to environmental change differently. Positive environmental changes offer optimum conditions for plants. However, adverse environmental exposure hinders the survival of the plants. Plant roots play a crucial role in triggering plant to adapt to a changing environment. I studied how maize responds to abiotic stress in its early growth stage. Water and salinity are the most common abiotic stresses encountered by maize roots, and X-ray tomography can improve our understanding of the root behaviour under different abiotic and biotic stresses as demonstrated in this chapter.

Appendix: The 3D Root architecture in all treatments and their replicates

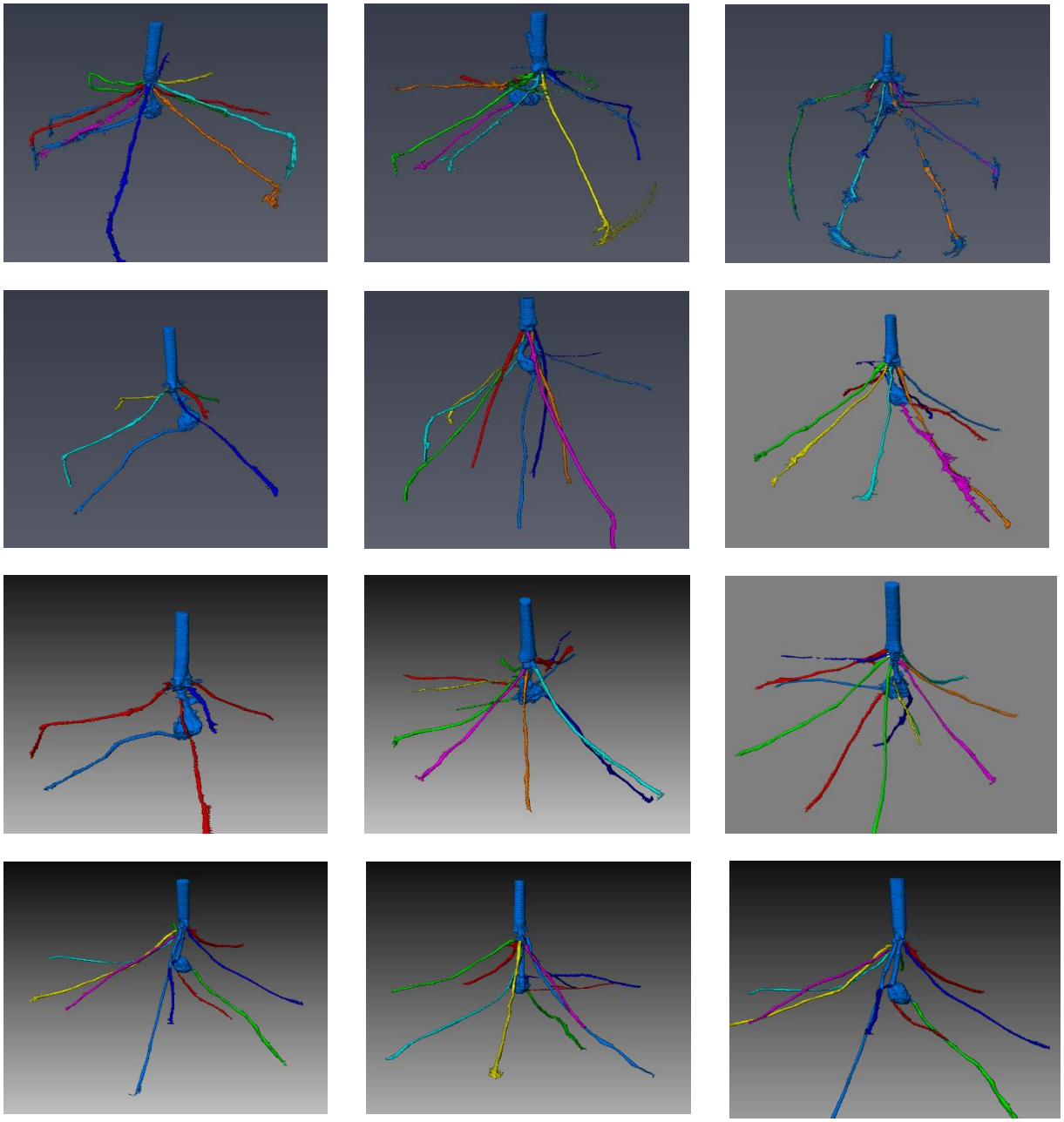

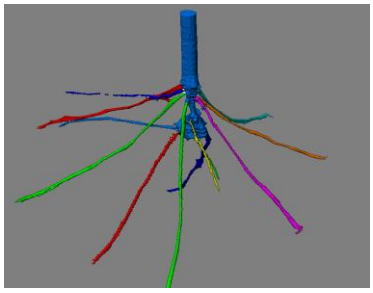
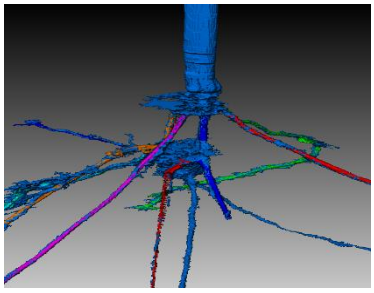
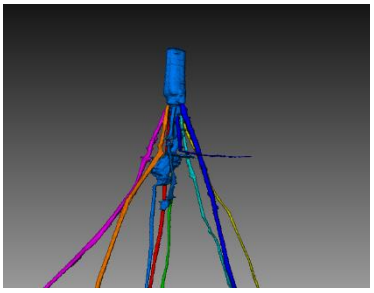
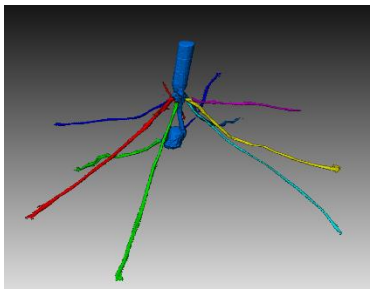
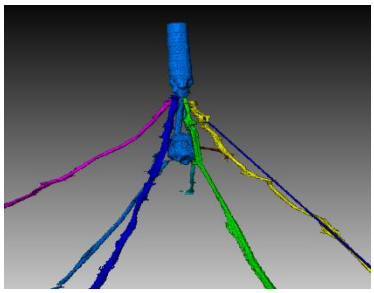
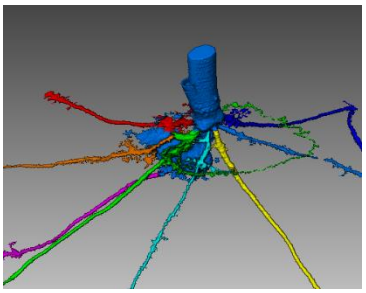
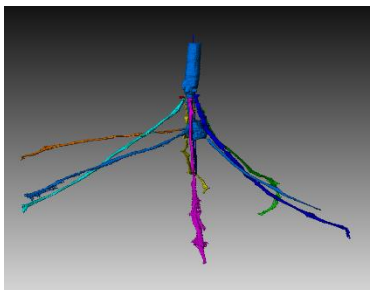
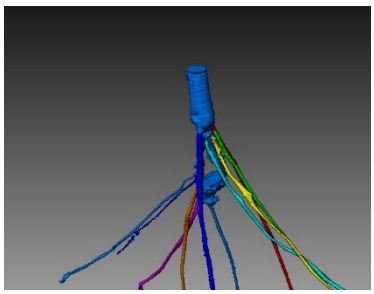
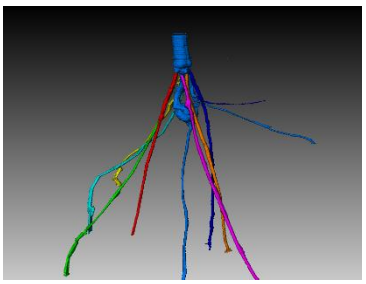
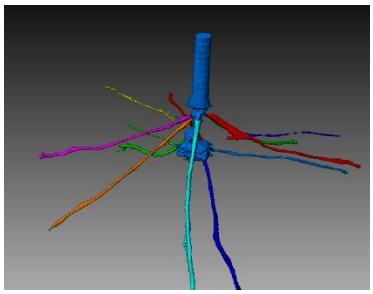
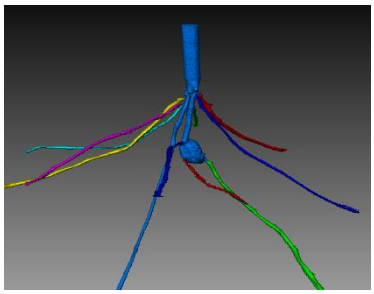
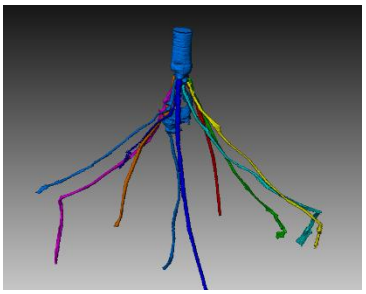

Chapter 4 Change in hydraulic properties of the rhizosphere under different abiotic stresses

4.1. Introduction

The rhizosphere is the small volume of soil impacting and being impacted by plant roots; it is the most active zone in the terrestrial ecosystem (Gregory, 2006). The large quantity of rhizodeposits secreted by roots, along with the imbalanced uptake of cations and anions by roots, makes the rhizosphere differ markedly from the bulk soil both physically and biochemically (Hinsinger et al., 2009). Early experiments showed that root growth led to a densification of the rhizosphere (Dexter, 1987), while recent studies found that root-mediated physical and biological processes could also increase the rhizosphere porosity via enhancing aggregation (Helliwell et al., 2019; Rabbi et al., 2018).

The change in physical properties of the rhizosphere is a result of the interplay of a multitude of biotic and abiotic processes (Hinsinger et al., 2009). Physically, root growth radially deforms its adjacent soil, resulting in a compression of the surrounding pore space. In contrast, mucilage and extracellular polysaccharides (EPS) exuded by roots and microorganisms have been shown to boost soil aggregation and increase the number of large pores relevant to water and nutrient flow (Alami et al., 2000). In addition to restructuring the rhizosphere, the mucilage and EPS also alter the surface tension and viscosity of soil water (Ahmed et al., 2016; Ahmed et al., 2018; Carminati et al., 2010; Hallett et al., 2003; Read et

al., 2003), rendering the rhizosphere either hydrophilic or hydrophobic depending on its moisture content (Carminati et al., 2010; Moradi et al., 2011).

Most research on change in the rhizosphere hydraulic properties has focused on water retention, whereas there is a paucity of studies on alteration of the rhizospheric hydraulic conductivity as directly measuring water flow in the rhizosphere is very difficult even using modern tomography(Huang et al., 2015; Ren et al., 2015) and tracer-based technologies (Totzke et al., 2017). As a result, indirect methods have been used as an approximation. For example, Zarebanadkouki et al. (2016) calculated the permeability of a lupin rhizosphere based on radiographic images acquired using neutron tomography, and Rabbi et al. (2018) calculated the permeability of a chickpea rhizosphere through pore-scale simulation based on X-ray CT images. Similar methods had also been used by others to calculate the unsaturated hydraulic conductivity of the rhizosphere (Daly et al., 2015; Tracy et al., 2015). These indirect methods provided some insight into how roots modulate their rhizosphere to facilitate water uptake, but they need to make assumptions about water flow in the void space which are difficult to justify experimentally. For example, the pore-scale simulations need to know the water velocity at the water-solid and water-air interfaces. While the water-solid interface could be assumed to be a non-slip boundary in hydrophilic soil where the water velocity is zero (Rabbi et al., 2018), the water-air interface for unsaturated flow is difficult to decide *a priori* (Tracy et al., 2015; Zhang et al., 2016e). Research using neutron imaging to inversely estimate the hydraulic conductivity of the rhizosphere has shown potential, but it required information on the hydraulic conductance of the roots which is difficult to measure *in vivo*

(Zarebanadkouki et al., 2016). Also, because neutrons are very sensitive to water, the application of neuron tomography to soil-root interactions is limited to 2D radiographic images as I demonstrated above (Carminati et al., 2010).

The putative role of the rhizosphere in regulating water uptake by changing its hydraulic properties has been well established (Bengough et al., 2011), but the impact of abiotic stresses on this change is an issue that remains elusive. This chapter is a continuation of the previous one - to study the change in physical properties of the rhizosphere of the maize. Two weeks after instigating the water and salinity stresses, I extracted the roots out of some pots to harvest the aggregates adhering to the roots and then scanned them using X-ray CT at much finer solution. The porosity, pore-size distribution of all aggregates were estimated from the segmented images, while their permeability and tortuosity were calculated from pore-scale simulations of water flow and solute diffusion in the void space. Comparisons were made with aggregates taken from the unstressed controls.

4.2. Materials and methods

The plant and soil were the same as those used in Chapter 3. The experiments were conducted simultaneously. Two weeks after the water stress and salinity stresses were initiated, one pot from each treatment was upturned down to remove the soil and roots gently from it. The loose soil was shaken off the roots first and I then manually removed three aggregates adhering to different roots from each pot. The aggregates were left in the greenhouse to air-dry, and they were then scanned with X-ray computed tomography in the same facility in the University of Nottingham. As a comparison, I also took aggregates from

an unplanted pot. All aggregates were geometrically irregular, and their size was approximately in the range of 2-5 mm. As an illustration, Figure 4.1 shows the aggregates and the roots taken out from two pots under different treatments.

Figure 4.1. Illustration showing the aggregates and the roots taken out from the pots.

4.3. Image acquisition

All aggregate samples were scanned using a Phoenix Nanotom X-ray CT scanner at the Hounsfield Facility at the University of Nottingham. The samples were loaded in a plastic tube as shown in Figure 4.2, which was mounted on the manipulator in the chamber of the

scanner. The samples were scanned using an electron acceleration energy of 85 keV and a current of 100μA at a spatial resolution of 4μm, with each sample taking approximately 30 mins to scan. Each scan consisted of the collection of 3600 images with a detector timing of 500ms. The raw images were constructed using the software phoenix datos|x (Waygate Technologies), and they were then saved as a stack comprising 16-bit grayscale 2D slices.

Figure 4.2. The aggregates were packed into a plastic tube to be scanned in the CT scanner.

4.4 Image analysis

4.4.1 Preparation

As discussed previously, the X-ray imaging is based on the difference in attenuation of X-ray by different constituents in a material. Soil comprises various organic materials and inorganic minerals which have contrasting ability to attenuate the X-ray. The resulting X-ray image of a soil is a grayscale image with different grayscale values representing different components in the soil. Separating the solid from the void phases in the soil thus needs to process the original grayscale X-ray images. The main steps in X-ray image processing include cropping, normalization, reducing noise and enhancement.

Figure 4.3 shows a grayscale image of one aggregate acquired using the X-ray CT. It is geometrically irregular, and the cropping is to take a cuboid out of the irregular image as shown in the figure, for ease of processing and quantitative analysis (Figure 4.3b). For the aggregates studied in this work, I cropped a cube or cuboid out from each image as shown in Figure 4.3c, with the size of the cube or cuboid varying with the aggregates.

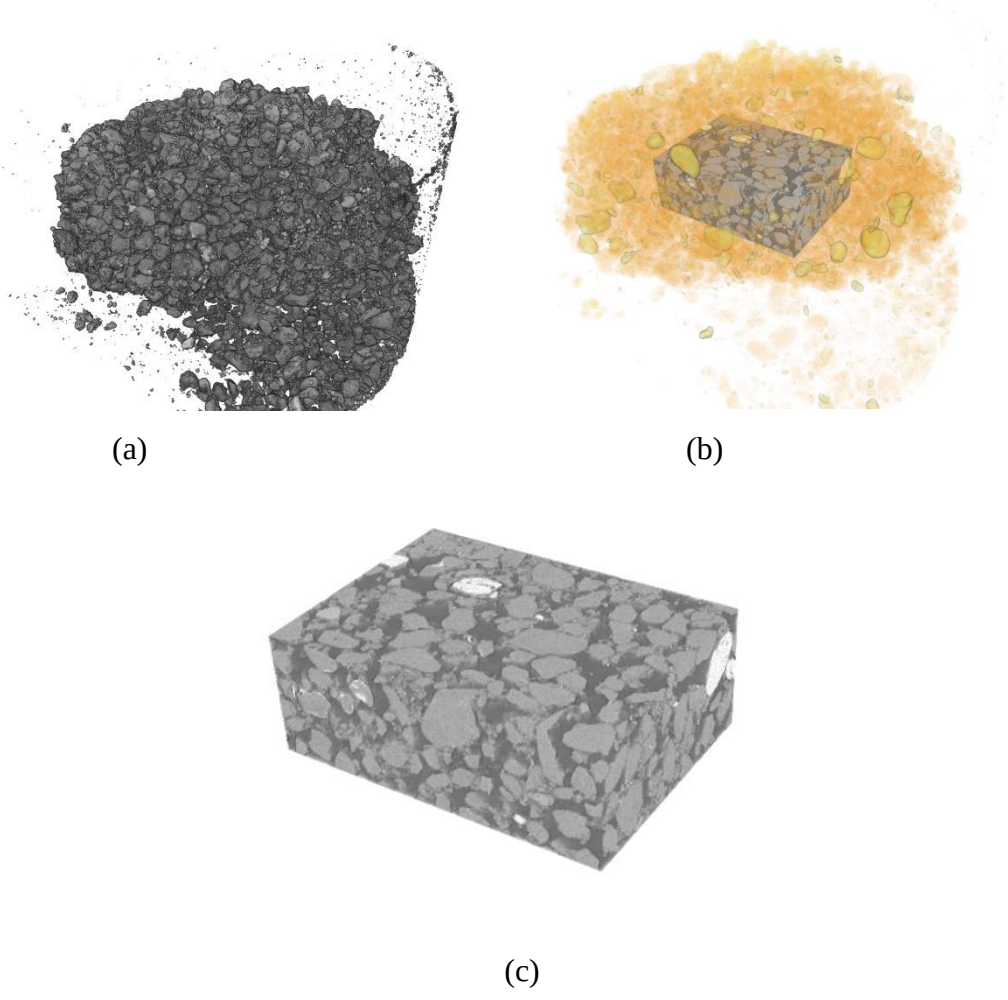

(a) (b)

(c)

Figure 4.3. Schematic showing the original grayscale image (a), and where the cuboid was cropped out from the image (b). The cropped image for analysis (c).

4.4.2. Noise removal and image improvement

Noise existed in the original images and was denoised before segmentation. The goal of denoising is not only to improve the quality of the images but also to reduce the errors (Gonzalez, 1987). Image noise is pixel(s) that is isolated and not on a cluster(s). Different methods are available to define noise in imaging processing and in this work, I focused on pores and defined pore pixels as noise if the size of the pores exposed in the image was less than 3 pixels and replaced them by solid pixels. As an illustration, Figure 4.4 shows the details of how the noises in a 2-D slice were removed.

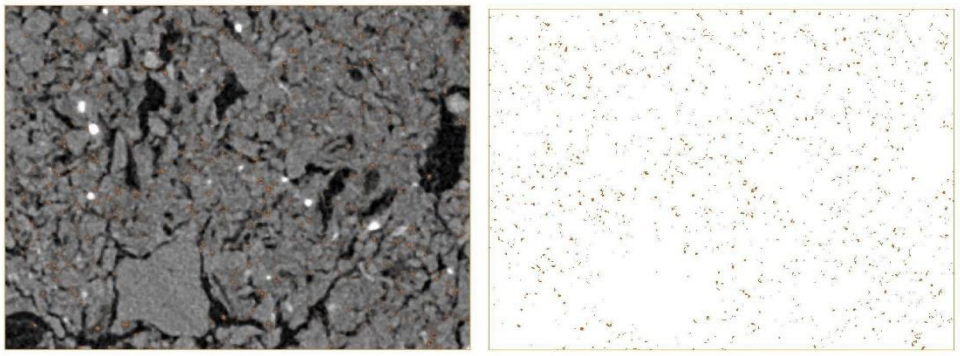

(a) (b)

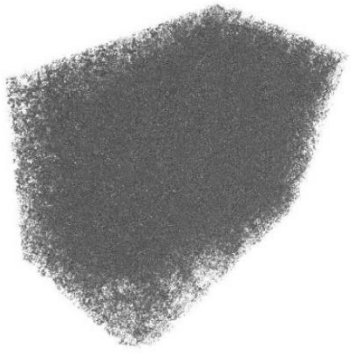

(c)

Figure 4.4. Illustration of noise removal in 2D slice. The red dots are noise pixels (a); and all but the noise pixels are made transparent (b). Locations of the noise pixels in 3D image.

The next step is normalization and enhancement. The normalization is to magnify the range of the grayscale value of the voxels in a specific region to make different materials in it more contrasting; the enhancement is to increase the contrast of the interfaces between different phases. These two steps are necessary to make a blurred image more contrasting in order to improve accuracy of the image segmentation. Figure 4.5 shows the improvement after the normalization and enhancement compared to the original image. It needs to be pointed out that the two treatments did not alter the image, and they just make it look more contrasting. When processing 8-bit image, I recalculated their voxels by increasing their saturation by 0.3%. This, together with the normalization and enhancement, improves the accuracy of the segmentation as to be discussed in the next sections.

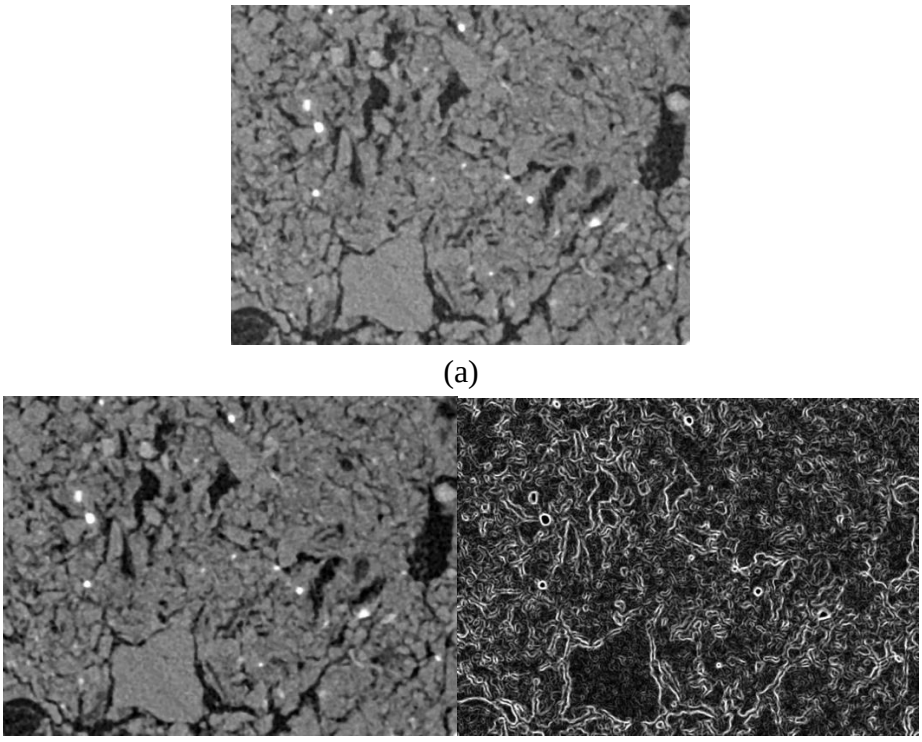

(a)

(b) (c)

Figure 4.5. Comparison of an original 2D image (a); after its normalization (b) and enhancement treatment of the phase interfaces (c).

4.4.3. Segmentation

Soil can be roughly divided into solid phase and void phase. To calculate the geometry of each phase, it needs to segment each soil sample into a binary image. Every voxel in the grayscale image is described by a grayscale value, and the image segmentation is based on the histogram of these grayscale values. A threshold in the histogram was used to segment the image. Over the past decade, different threshold methods have been proposed to segment X-ray images, which can be approximately divided into groups: Local threshold method and global threshold method. Global threshold method is to use a single threshold to segment an entire 3D image, while the local threshold method is to segment each 2D slice (or local 3D regions) using a threshold. Local threshold method is more accurate, but it is tedious for large samples. In this work, I used the global threshold in all segmentations. Figure 4.6 shows the histogram of an 3D image acquired using the X-ray CT.

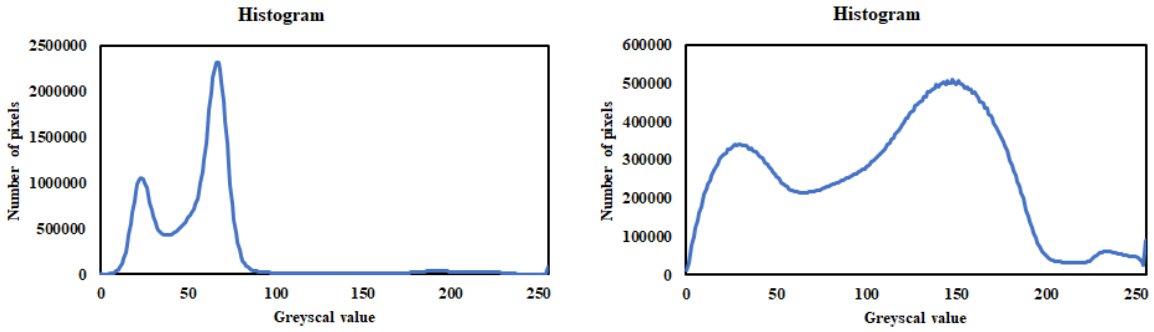

(a) (b)

Figure 4.6. Histogram of the grayscale values of all voxels in a 3D image. (a) Histogram of the original image; (b) histogram of the image after normalization and enhancement.

Figure 4.7 compares the binary images segmented using 12 global threshold methods for the 2D slice shown in Figure 4.5. It is evident that they differ substantially. Comparing

these segmented images with the original grayscale image reveals that the Otsu method appears to have captured the pore geometries more accurately than other methods, and it was thus used in what follows. All the images were segmented using the software Image J (University of Wisconsin-Madison).

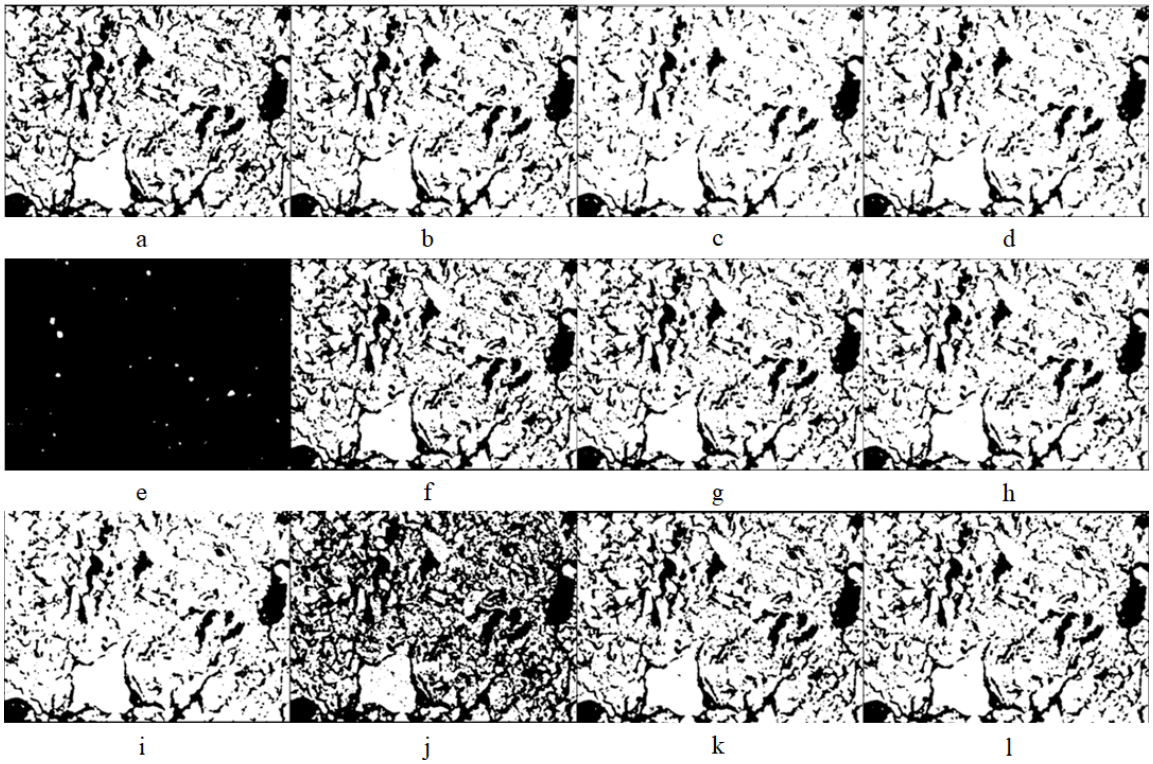

Figure 4.7. Comparison of binary image segmented by 12 global threshold methods. Optimized Iso-Data method (a), Huang (b), Triangle (c),Yen (d), Intermodes (e), Otsu (f), Iso-Data (g), Li (h), MaxEntropy (i), Moments (j), Huang 2 (k) and Shanbhag (l).

4.5. Pore-size distribution

Each pore in a 3D segmented image was approximated by an inscribed sphere and I defined the diameter of the sphere as the diameter of the pore. The histogram of the diameters of all pores in the image is known as pore-size distribution (PSD) in the literature.

The PSD of each soil was calculated using the Plug-in CT-image Analysis & Manipulation Plugin (SCAMP) in the ImageJ. To verify the method, I also recalculated the

PSD using Avizo, finding that the difference between the two was less than 5% as shown in Figure 4.8. In what follows I will only present the results obtained from SCAMP. Since all noisy voxels had been removed, only the pores with diameters >8μm were accounted for in the PSD.

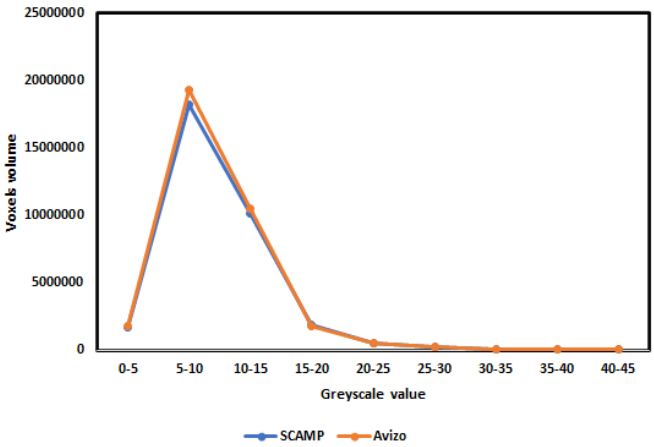

Figure 4.8. Comparison of the pore size distributions calculated by Avizo and SCAMP.

4.6. Hydraulic conductivity and permeability

Water flow is natural soils is driven by gravity and pressure gradient, and their relationship is described by the empirical Darcy's Law. For horizontal water flow through a tube filled with soil as shown in Figure 4.9, the flow rate across the vertical section of the tube is

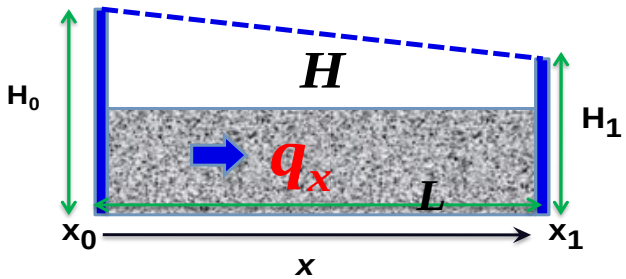

Figure 4.9. Schematic showing water flow in a horizontal tube filled with soil.

$$q = \frac{Q}{A} = \lim_{x_0 \to x_1} -K \frac{H_1 - H_0}{x_1 - x_0} = -K \frac{\partial H}{\partial x} \qquad (4\text{-}1)$$

where q is the flow rate across a unit cross-section area (m/s), Q is the volumetric flow rate across the section (m^3/s), A (m^2) is the cross-section of the tube, K is the hydraulic conductivity of the soil (m/s), H_0 and H_1 are the water pressure head (m) at the two ends, and x_0 and x_1 are the coordinates of the two ends.

Eq. (4-1) is for water flow in soil and the water pressure is described by the water head. For flow of other fluids, such as gases, in the same soil, if their viscosity and density differ from that of water, Eq. (4-1) needs to be modified to take the change in density and viscosity into account by the following formula:

$$q = -\frac{k}{\mu\rho} \frac{\partial P}{\partial x} \qquad (4\text{-}2)$$

where ρ is the density of the fluid (g/cm^3), μ is the kinematic viscosity of the fluid (cm^2/s), P is pressure (Pa/cm^2), k is permeability of the soil (cm^2), g is gravitational accelerations (cm/s^2), k(cm^2) is permeability. The permeability depends on soil structure only. As the interest in fluid flow in soil includes both liquid water and gaseous fluids such as CO_2, in what follows, I will only present the results for the permeability.

Eqs. (4-1) and (4-2) are for macroscopic flow with the detailed microscopic processes averaged out. The impact of pore geometry is instead represented by hydraulic conductivity or the permeability. Hydraulic conductivity and permeably of a soil can be measured using specific apparatus but they all need the samples to be sufficiently large (>5cm, typically). For aggregates taken from the rhizosphere studied is this work, they are highly irregular and only

a few millimetres in diameter, and directly measuring their permeability is impossible. I hence calculated it from pore-scale simulations using in-house codes developed by Rothamsted Research (Zhang et al., 2016d) .

The permeability of each aggregate is the consequence of fluid flow in its 3D pore space, and the pore-scale simulation is to mimic the 3D fluid low process. Pore-scale simulation of fluid flow was conducted using the lattice Boltzmann (LB) method, and its details were given in the appendix and in the literature (Li et al., 2018a; Zhang et al., 2016b; Zhang et al., 2005; Zhang and Lv, 2007). In short, initial water velocity in all simulations was zero, and fluid flow through the pore space of each aggregate was instigated by imposing an external pressure gradient in one direction of the image. The flow was then simulated to steady state, deemed to have reached once the absolute relative difference between the sum of absolute fluid velocity in all voxels simulated at two time points separated by 100 time-steps was less than 10^{-7}. At steady state, the fluid velocity and pressure in the voxels were volumetrically averaged over each section normal to the imposed pressure gradient direction. The permeability of the aggregate in the imposed pressure direction was calculated as follows assuming that the volumetric average flow rate (q) and the volumetric average pressure (P) in the imposed pressure direction follows Darcy's law:

$$q = -\frac{k}{\mu}\nabla P, \qquad (4\text{-}3)$$

where k is the permeability and μ is the viscosity of the water. The permeability of each aggregate was calculated as follows from the simulated results:

$$k = \frac{\mu q L}{P_0 - P_1}, \tag{4-4}$$

where L is the length of the image in the direction in which the external pressure gradient was imposed, and P_0 and P_1 ($P_0 > P_1$) were the two constant pressures imposed on the two opposite sides of the image to drive the fluid flow. The average volumetric flow rate depends on the average flow direction. For example, when imposing the pressure gradient in the z direction, the q in Eq. (4-4) was calculated from

$$q = \frac{1}{N} \sum_{i=1}^{N} u_z \left(x_i, y_i, z_i \right), \tag{4-5}$$

where N is the number of all voxels in the image, including both fluid-filled pores and solid vowels, $u_z \left(x_i, y_i, z_i \right)$ is the water velocity component in the z direction at voxel centred on $\left(x_i, y_i, z_i \right)$. The permeability of a soil depends on the direction the external pressure gradient is applied to, and for each image, I calculated its permeability in the three directions.

4.7. Tortuosity

The permeability of a soil depends not only on its porosity but also on how the pores of different sizes are spatially connected. I used tortuosity to represent the change in pore connectedness in each aggregate. For idealised pore media such as bended capillary tube, the tortuosity is defined as the ratio of the real length of the tube to the Eulerian distance between the two ends of the tube (Ghanbarian et al., 2013). However, its definition and calculation for complicated media such as soil is far more complicated (Fu et al., 2021). It can be either calculated as a geometric parameter or based on a specific transport process such as fluid

flow and molecular diffusion (Fu et al., 2021). In this project, I calculated it as the ratio between the effective diffusion coefficient of an aggregate for a solute and the molecular diffusion coefficient of the solute in water (Wang et al., 2020; Zhang et al., 2021). The effective diffusion coefficient was calculated using the pore-scale model developed by Rothamsted Research and the details will be described in the next chapter.

4.8. Statistical analysis

Statistical comparison of porosity, permeability, tortuosity and pore-size distribution between the treatments was performed using the software MATLAB. The difference in the mean (n=3) between the treatments was assessed by analysis of variance (ANOVA) and *post-hoc* pairwise comparisons of the treatment-means were performed using the Duncan's multiple range test with the difference considered significant at $p < 0.05$. The difference in pore-size distribution between the treatments was calculated using the Kolmogorov-Smimov test.

4.9 Results

Figure 4.10 compares a 2D slice and its segmentation, and Figure 4.11 shows four pairs of 3D grayscale images and their associated segmentations, with each pair illustratively representing one treatment. Visual comparison of the greyscale and segmented images in both 2D and 3D revealed that the segmentation method correctly captured the pore geometries.

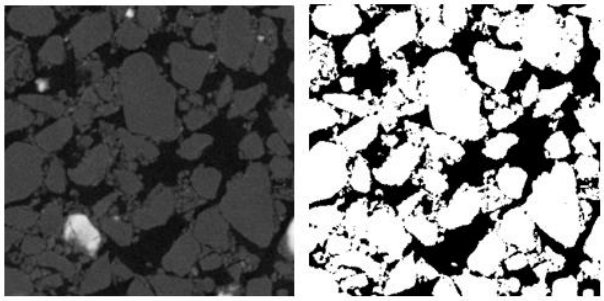

Figure 4.10. Schematic comparison of a grayscale 2D slice and its segmentation.

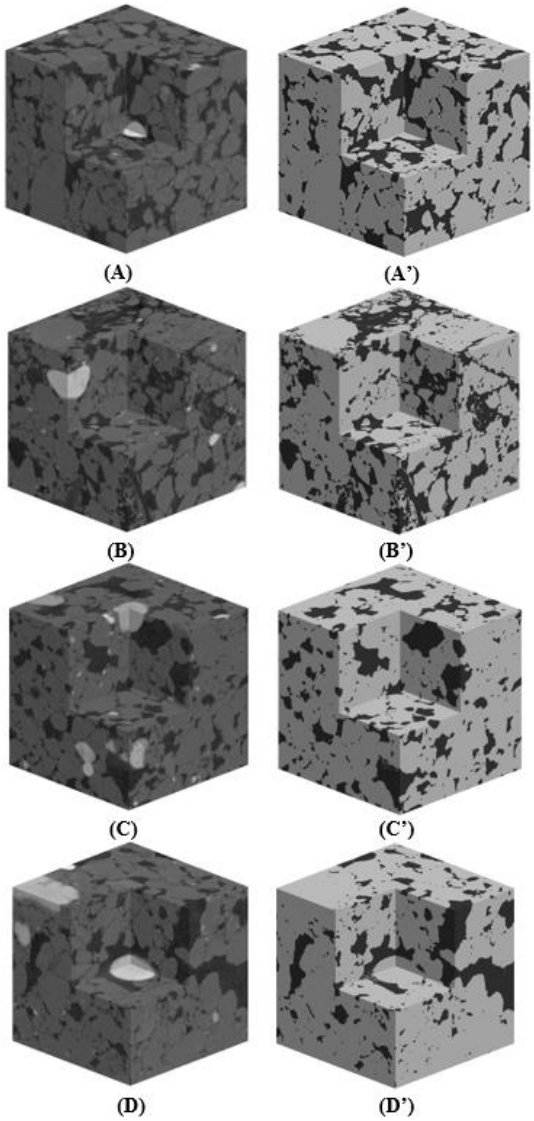

Figure 4.11. Representative grayscale image and its associated segmentation for each treatment acquired using the X-ray CT at resolution of 4 μm. A-A′: unstressed control (CK); B-B′: drought stress; C-C′: salinity stress; D-D′: combined water and salinity stresses. Pores are in black and others are in grey.

Figure 4.12 compares the average pore-size distribution. In general, abiotic stress reduced the relative volume of large pores and increased the relative volume of small pores, especially for aggregates subjected to the combined water and salinity stresses. Pore-size distributions for aggregates subjected to water and salinity stresses in isolation are comparable and the Kolmogorov-Smimov test did not find significant difference between the CK and all treatments. Because of beamtime limitation, I only scanned one sample taken from the unplanted pot and thus excluded it in the statistical analysis hereafter.

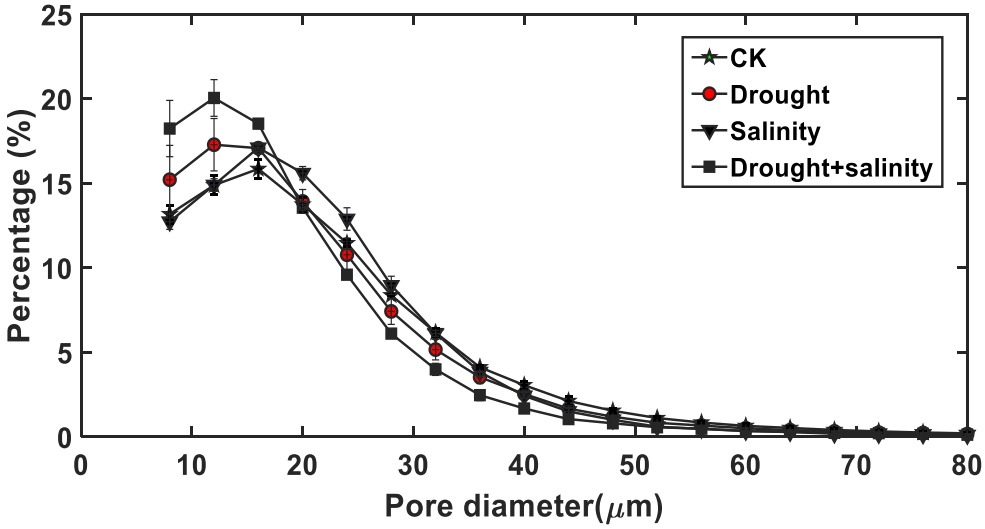

Figure 4.12. Comparison of the pore-size distributions for aggregates taken from different abiotic stress treatments and the unstressed control (CK).

Figure 4.13a compares the porosity of the aggregates under different treatments. Abiotic stress led to a reduction in aggregate porosity, especially for the combined water and salinity stresses which reduced the porosity significantly ($p < 0.05$) from 0.246 in the CK to 0.167. Differences between the three abiotic stress treatments, as well as the difference between the CK and the treatments with the stresses in isolation, were not significant.

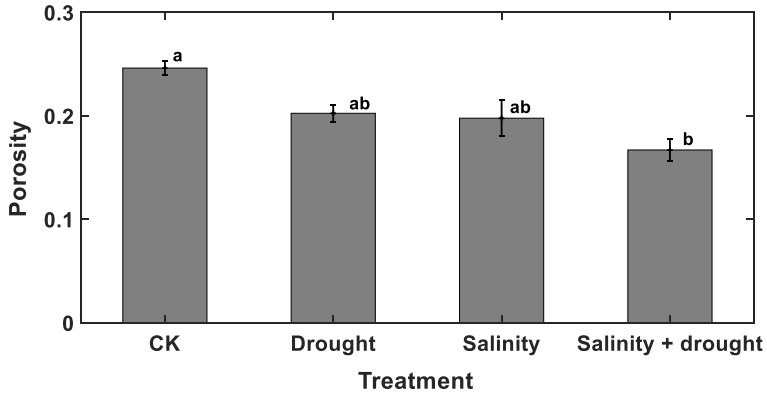

(a)

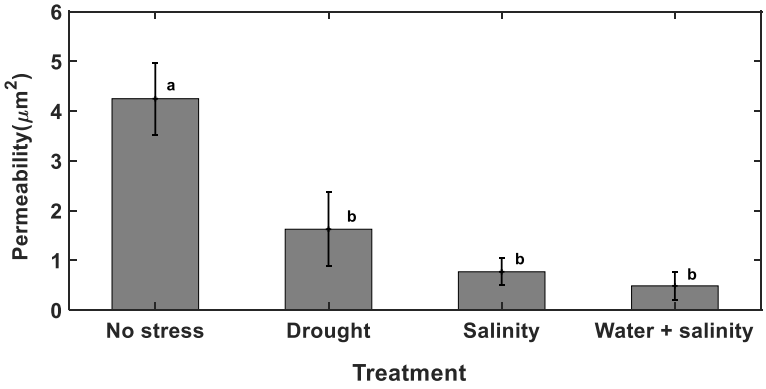

(b)

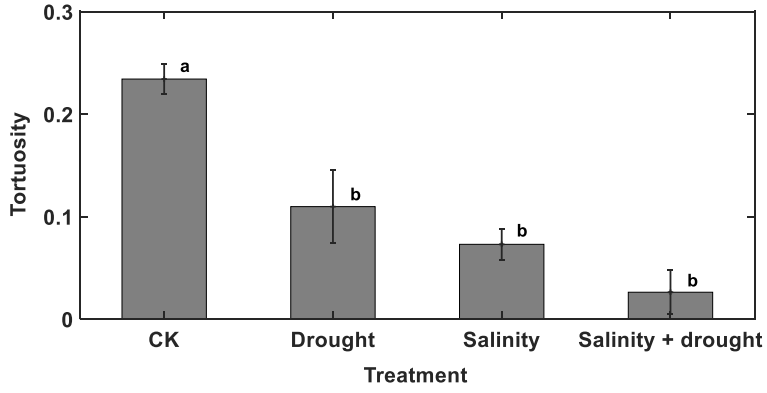

(c)

Figure 4.13. Comparison of the porosity (a), permeability (b) and tortuosity (c) of the aggregates taken from different abiotic stress treatments and the unstressed control (CK). The lowercase letters on top of the bars represent a significant difference at $p < 0.05$.

The tortuosity for different treatments was compared in Figure 4.13c. Abiotic stress resulted in a significant decrease in tortuosity compared with CK ($p < 0.05$). There was no significant difference between the three stress treatments.

The permeability calculated for the three orthogonal directions in each aggregate differed for some aggregates. As permeability is a sensor, for the pressure gradient imposed in each direction I calculated both the diagonal and the off-diagonal permeability components and found that for most aggregates, the two off-diagonal permeability components were at least one order of magnitude smaller than the diagonal permeability component. In the analysis, I thus used the average of the three main permeability components in each aggregate to compare the treatments. Figure 4.13b shows the permeability of the aggregates under different treatments. It was manifested that both stresses reduced the rhizospheric permeability significantly ($p < 0.05$) either working alone or in combination. Compared to the CK, water stress reduced the average permeability by approximately 60% and salinity stress by 80%, while combining water and salinity stresses reduced the permeability by nearly 90% from 4.32 μm^2 to 0.49 μm^2.

The reduction in permeability under stress is partly due to the decrease in porosity, and the relationship between the permeability and the porosity for all treatments appeared to follow a power law function with an exponent of 4.42 as shown in Figure 4.14. However, the deviation from the power law indicates that the change in porosity was important but not the only reason.

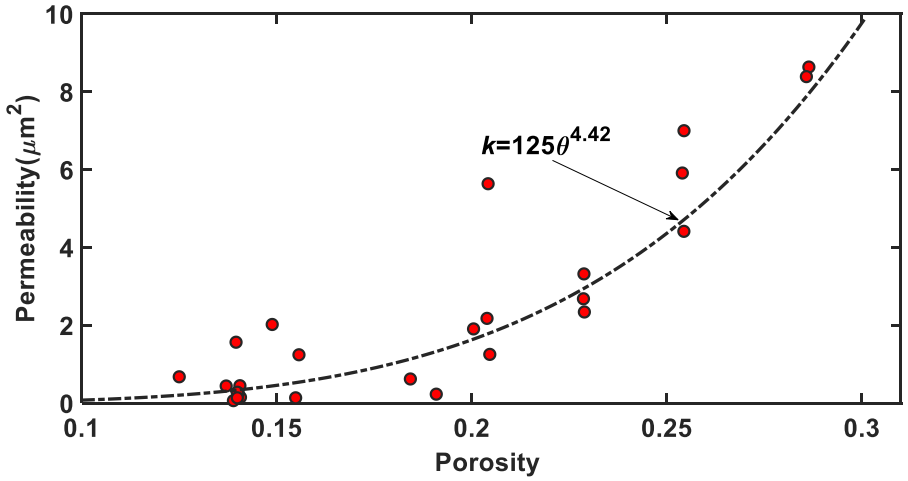

Figure 4.14. Change in permeability (symbols) with porosity θ for all aggregates taken from all treatments, and the fitting of power-law k=125 $\theta^{4.42}$ (solid line).

4.10. Discussion

The permeability and tortuosity calculated from pore-scale simulations for aggregates not subjected to abiotic stress differed significantly from those subjected to water and salinity stresses, although the difference between the treatments with water and salinity stresses working alone or in combination was not statistically significant (Figures 4.13b, c). As I thoroughly sieved and mixed the soil before packing it into the pots, the aggregates formed on the root surfaces were likely the consequence of roots and root-mediated processes. As such, the variation between their permeability and tortuosity was due to the impact of the treatments rather than spatial heterogeneity. This was also corroborated by the porosity, for which I found significant difference ($p < 0.05$) only between the CK and the treatment with combined water and salinity stress, while the difference between the CK and other treatments was not significant (Figure 4.13a). These results suggested that the change in permeability and tortuosity was not solely caused by porosity change, and that the pore structure formed by biotic activities in the aggregates, such as root hairs and fungus, might also play an

important role. These, along with other processes, made the aggregates in the vicinity of the rhizosphere respond differently to the abiotic stresses (Crawford et al., 2012), although it was impossible to distinguish the relative dominance of one over another.

Compared to the CK, salinity stress working in isolation or combined with water stress reduced the permeability and tortuosity of the aggregates at $p < 0.05$ significant level (Figures 4.13b, c). NaCl was added to deliberately salinize the soil and the Na could have dispersed the clay particles and consequently weakened the aggregation in both the rhizosphere and bulk soil. This could be one reason underlying the reduced porosity and permeability of the rhizosphere under salinity stress, but does not appear to be the only one as water stress also reduced porosity as much as the salinity stress did (Figure 4.13a).

Soil permeability depends not only on porosity but also on how pores of different sizes are spatially organized. The tortuosity of aggregates under different treatments showed that salinity stress rendered the soil more tortuous than water stress, making the aggregate more difficult for water and solute to move (Figures 4.13b). Although salinity and water stresses changed intra-aggregates structures and their ability to transport water and solute, the change in permeability with porosity for samples taken from all treatments appears to follow a common relationship (R^2=0.65) as shown in Figure 4.14, manifesting the importance of porosity. However, the deviation from the power law function implies that the shape and spatial organization of the pores also played an important role.

Reduction in rhizosphere porosity and its ability to transport water and solute due to water and salinity stress would restrict root uptake of water and acquisition of dissolved

solutes by the plant. Apparently, I do not know if this is a physiological response of the plant as a self-defence mechanism to reduce transpiration (saving water under water stress) and salt uptake (ameliorating salt toxicity) or purely a passive soil physical process without active influence from the plant.

Visual observation of the root architectures revealed that the abiotic stresses curtailed root ramifying and made the roots thinner than those not under stress (Figure 4.1). Radial expansion of roots locally compacts the soil and thus the thick roots should mechanically densify the rhizosphere more than the thin roots. However, our data does not support this and in contrast, the opposite appears to be true indicating that other mechanisms might have played a role in structural and permeability change in the rhizosphere under water and salinity stresses.

Maize is known to exude a large amount of mucilage into the soil providing C to support a diverse microbial community. This process can bind soil particles together and enhance aggregation in the rhizosphere (Benard et al., 2019). Aggregates bound by mucilage are quite stable even after desiccation (Benard et al., 2019); such aggregations could create pores detectable by X-ray imaging at resolution of 4 μm. For example, the experimental study of Benard et al. (2019) showed that amending soil with maize mucilage increased soil porosity by 10% but reduced the hydraulic conductivity because of the increase in water viscosity. I speculated that abiotic stress might alter mucilage secretion and change soil aggregation and the intra-aggregate structure as a result. I used permeability rather than hydraulic conductivity to describe the ability of the aggregates to conduct fluid as I do not know to what extent the

abiotic stresses and root-mediated processes had altered the water viscosity. In addition to mucilage, the difference in root hair proliferation under different treatments could be another mechanism underlying the change in porosity and permeability as affected by abiotic stresses (Rabbi et al., 2018).

The enhanced aggregation by roots and root-associated abiotic and biotic activities also create large pores between the aggregates. Due to technical limitations, it was not possible to scan the entire pots (20 cm high and 15 cm in diameter) at a resolution high enough to identify the inter-aggregate pores. Therefore, our results on the impact of abiotic stresses on soil structure were limited to the aggregates adhering to the roots rather than the alteration in properties of the whole soil that includes both inter-aggregate and intra-aggregate features. Also, I repacked soil into pots and conducted the experiments in a controlled environment. This limited the space for roots to grow and did not capture the physical and biochemical heterogeneity of field soil. Therefore, it would be prudent not to extrapolate my findings to those of maize growing in field conditions. Notwithstanding these, my results do shed some light on the role of abiotic stresses in mediating root-soil interactions and provide a way to improve our mechanistic understanding of the impact of real-world abiotic stresses on crop growth.

4.11. Conclusions

This chapter studied the impact of abiotic stresses on structural change in the rhizosphere of maize and its consequence for the rhizospheric permeability and tortuosity using X-ray CT and pore-scale simulations. The results showed that compared to an

unstressed control, water stress reduced the soil permeability by approximately 60% and the salinity stress reduced it by 80% when working in isolation, while combining the two stresses reduced the soil permeability by 90%. Since water and nutrients need to pass through the rhizosphere before being taken up by roots, change in physical properties of the rhizosphere has important implications for unravelling how roots respond to abiotic stress. Given the increasing interest in improving crop productivity by manipulating their root traits as discussed in Chapter 2, understanding the changes in physical properties of the rhizosphere in response to abiotic stresses is critical. Since the rhizosphere is only a few millimetres within the proximity of the root and directly measuring its physical properties, especially its ability to conduct fluids, is difficult technically, combining pore-scale simulation and X-ray CT, as described in this chapter and above, could help to bridge this gap. I made such efforts in this and above chapter.

Appendix A

Water flow and solute diffusion through the void space of the segmented images were both simulated by the following lattice Boltzmann model (d'Humières et al., 2002):

$$f_i\left(\boldsymbol{x}+\delta t\boldsymbol{e}_i, t+\delta t\right)=f_i\left(\boldsymbol{x},t\right)+M^{-1}SM\left[f_i^{eq}\left(\boldsymbol{x},t\right)-f_i\left(\boldsymbol{x},t\right)\right], \qquad \text{(A1)}$$

where $f_i\left(\boldsymbol{x},t\right)$ is the particle distribution function at location $\boldsymbol{x}$ and time t moving at lattice velocity $\boldsymbol{e}_i$, δx is the size of the image voxels, δt is a time step, $f_i^{eq}\left(\boldsymbol{x},t\right)$ is the equilibrium distribution function, M is a transform matrix and S is the collision matrix. The models for water flow and solute transport differed only in their equilibrium distribution functions, both involving a collision step and a streaming step to advance a time step. In each model, the

collision was calculated as $m = SM\left[f_i^{eq}(\boldsymbol{x},t) - f_i(\boldsymbol{x},t)\right]$ first and *m* was then then transformed back to particle distribution functions by $M^{-1}m$. In both models, we used the D3Q19 lattice in which the particles move in 19 directions with velocities: $(0,\ 0,\ 0)$, $(\pm\delta x/\delta t,\ \pm\delta x/\delta t,\ 0)$, $(0,\ \pm\delta x/\delta t,\ \pm\delta x/\delta t)$, $(\pm\delta x/\delta t,\ 0,\ \pm\delta x/\delta t)$ and $(\pm\delta x/\delta t,\ \pm\delta x/\delta t,\ \pm\delta x/\delta t)$ (Qian et al., 1992).

Model for water flow

The collision matrix in the model for water flow is diagonal:

$$\begin{aligned} &S = (s_0, s_1, s_2, s_3, s_4, s_5, s_6, s_7, s_8, s_9, s_{10}, s_{11}, s_{12}, s_{13}, s_{14}, s_{15}, s_{16}, s_{17}, s_{18})^T, \\ &s_0 = s_3 = s_5 = s_7 = 0, \\ &s_1 = s_2 = s_{9-15} = 1/\tau, \\ &s_4 = s_6 = s_8 = s_{16-18} = 8(2-\tau^{-1})/(8-\tau^{-1}), \end{aligned} \tag{A2}$$

and the equilibrium distribution functions are

$$\begin{aligned} &f_i^{eq} = w_i\left[\rho + \rho_0\left(\frac{3\boldsymbol{e}_i\cdot\boldsymbol{u}}{s^2} + \frac{9(\boldsymbol{e}_i\cdot\boldsymbol{u})^2}{2s^4} - \frac{3\boldsymbol{u}\cdot\boldsymbol{u}}{2s^2}\right)\right], \\ &w_0 = 1/3, \\ &w_i = 1/18, \qquad \|\boldsymbol{e}_i\| = \delta x/\delta t \\ &w_i = 1/36 \qquad \|\boldsymbol{e}_i\| = \sqrt{2}\delta x/\delta t \end{aligned} \tag{A3}$$

where $s = \delta x/\delta t$ and ρ_0 is a reference fluid density to ensure an incompressible fluid at steady state (Zou et al., 1995). The water density ρ and bulk water velocity $\boldsymbol{u}$ are calculated from

$$\begin{aligned} &\rho = \sum_{i=0}^{18} f_i, \\ &\boldsymbol{u} = \sum_{i=1}^{18} f_i\boldsymbol{e}_i/\rho_0. \end{aligned} \tag{A4}$$

The kinematic viscosity of fluid was $\nu = \delta x^2(\tau - 0.5)/6\delta t$ and its pressure is related to density in $p = \rho\delta x^2/3\delta t^2$.

Model for solute diffusion

The equilibrium distribution functions for solute diffusion are defined by

$$f_i^{eq} = w_i c, \tag{A5}$$

where c is solute concentration and the weighting parameter w_i is the same as those defined in Eq. (A3). The diagonal collision matrix for solute diffusion is uniform:

$$S = \left(\tau_0, \tau_0, \tau_0, \tau_0, \tau_0, \tau_0, \tau_0, \tau_0, \tau_0, \tau_0, \tau_0, \tau_0, \tau_0, \tau_0, \tau_0, \tau_0, \tau_0, \tau_0, \tau_0\right)^T, \tag{A6}$$

The collision can thus be directly calculated from $m = \tau_0\left[f_i^{eq}(\boldsymbol{x},t) - f_i(\boldsymbol{x},t)\right]$ without need of the transform as for fluid flow. The concentration c and the diffusice flux $\boldsymbol{j}$ in each voxel are calculated from

$$\begin{aligned} c &= \sum_{i=0}^{18} f_i^{eq}, \\ \boldsymbol{j} &= \sum_{i=0}^{18}(1-0.5/\tau_0)e_i f_i^{eq}, \end{aligned} \tag{A7}$$

The molecular diffusion coefficient in the above model is $D_0 = \delta x^2(1/\tau_0 - 0.5)/6\delta t$. The effective diffusion coefficient of the image was calculated using the method proposed in our previous work (Zhang et al., 2016c).

Model implementation

For both water flow and solute diffusion, there are two calculations to advance one time step. The first one is to calculate the collisions: $f_i^* = f_i(\boldsymbol{x},t) + M^{-1}SM\left[f_i^{eq}(\boldsymbol{x},t) - f_i(\boldsymbol{x},t)\right]$ for water and $f_i^* = f_i(\boldsymbol{x},t) + \tau_0\left[f_i^{eq}(\boldsymbol{x},t) - f_i(\boldsymbol{x},t)\right]$ for solute, and the second step is to move f_i^* to $\boldsymbol{x} + \delta t\boldsymbol{e}_i$ at the end of δt. Whenever f_i^* hits a solid voxel during the streaming, it is bounced back to where it emanates to ensure a zero velocity on the water-solid interface for both water flow and solute diffusion.

Chapter 5. Salt accumulation in the rhizosphere

5.1. Introduction

Water flow and solute transport in soil in the terrestrial ecosystem is driven by gravity and evapotranspiration. As water evaporates, solute moving with it accumulates in the proximity of the surface soil; when the enriched concentration exceeds solute solubility, it precipitates becoming salt crust within the pores (Bechtold et al., 2011). Soil salinization caused by evaporation has been known for centuries, yet how soil microscopic structure and the precipitated salt intertwined to reshape each other and impact water flow and solute movement remains poorly understood (Bergstad and Shokri, 2016). Recent experiments found that manipulating soil structure can guide solute to move and precipitate in desirable direction and location (Bergstad et al., 2018; Bergstad and Shokri, 2016), which has inspired the development of innovative technology to improve crop management in salt-affected soil (Berezniak et al., 2017) and engineering the rhizosphere to facilitate resource acquisition by plant roots (Ahmed et al., 2018).

Together with evaporation, transpiration induced by root water uptake is another way that water is lost to the atmosphere. Since root selectively takes up solutes, solute whose mass flow - driven by root water uptake - toward the root exceeds root uptake would accumulate at the root-soil surface (Alharby et al., 2018). Typical such excessive elements include Na^{+}, $H_2SiO_4^{2+}$, Al^{3+}, Ca^{2+}, Mg^{2+}, Cl^{-}, SO_4^{2+}; under anaerobic condition, Fe^{2+} and Mn^{2+} are also more abundant in the rhizosphere (Khan et al., 2020). Experiments found that the

concentration and composition of excessive ions in the rhizosphere could be ten times higher than that in the bulk soil (Hinsinger et al., 2003), creating a concentration gradient extending from a few millimetres to a few centimetres from the root surface (Kuzyakov and Blagodatskaya, 2015; Vetterlein et al., 2004). Because root water uptake dries the rhizosphere and consequently reduces its aqueous transportability, when molecular diffusion is insufficient to drive the excessive ions away, solute could precipitate at the root-soil surface. For example, it has been found that extreme solute accumulation at the soil-root interface could lead to the calcified root (Zamanian et al., 2016) and plaque around the root (Melton et al., 2014).

In addition to toxicity, solute enrichment in the rhizosphere generates an osmotic potential (Vetterlein et al., 2004). As water flow from the soil into the root is proportional to the difference in water potential across the root membrane, the increased osmotic potential slows down or even prevents root water uptake when the enriched concentration is high enough to drop the water potential in the soil equal to or even lower than that in the root (Hamza and Aylmore, 1992). Recent work has found that root water uptake changes spatiotemporally with root age as the plant grows (Vetterlein and Doussan, 2016). For example, maize takes up most water from its seminal and lateral roots at its early growth stage, while at the late stage most water the plant transpires is supplied by crown roots (Ahmed et al., 2016). Water uptake by individual root is not uniform from its proximal end to the distal end. In lupin root, for example, radial water flux into its proximal segment was found higher than into its distal segment (Zarebanadkouki et al., 2013). Since the osmotic

potential is linked to solute concentration across the root membrane, it is imperative to understand how heterogeneous water uptake by individual root underpins solute distribution in its rhizosphere and the consequence for water and nutrient uptake.

Patchy solute distribution in soil is important for crops to maintain their functions because if solute spreads uniformly, it would be lethal to crops (Bazihizina et al., 2012). Experimental findings are that root water uptake by crops under spatially homogeneous salt stress is less than by crops grown in spatially heterogeneous salinity (Sun et al., 2016) because, in the latter, roots not under salinity stress can upregulate their water and nutrient transport-related genes to enhance uptake (Kong et al., 2017). While the above studies have improved our understanding of how crops respond to salinity, most them were based on pot experiments by subjecting part of the plant roots to salinity stress while keeping the other part stress-free (Bazihizina et al., 2012). This differs from what crops could endure in field where surface evaporation and ion-filtering by roots combine to intriguingly redistribute the solute heterogeneously at scales from millimetres (variation from rhizosphere to bulk soil) to tens centimetres (variation from surface soil and subsoil). Ion-filtering by roots have been intensively studied at the root zone and rhizosphere scales (Alharby et al., 2014; Mmolawa and Or, 2000), but there is a paucity of knowledge about how the nonuniform water uptake by individual root redistributes solute in its rhizosphere although progress has been made thanks to the development in imaging and tracer technology (Haber-Pohlmeier et al., 2019).

Application of tomography in soil research has substantially improved our understanding of how root modulates its rhizosphere, both physically and biochemically, as detailed in the above chapters, to facilitate resource acquisition (Aravena et al., 2014; Helliwell et al., 2017; Moradi et al., 2011; Rabbi et al., 2018). It also helps unravel how microscopic soil structure and solute precipitation intertwined to impact and be impacted by water evaporation (Berezniak et al., 2017; Bergstad et al., 2018) and solute enrichment in root zone (Haber-Pohlmeier et al., 2019). This has inspired developing innovative technology to manage crops in saline soil (Berezniak et al., 2017). The ultra-fast neutron tomography can even capture water flow in rooted soil at a temporal interval of 10 seconds (Totzke et al., 2017). Since water flow and solute transport in the rhizosphere is regulated by its physical structure, understanding how a root enriches solute and alerts its hydraulic properties is imperative.

The purpose of this chapter is to investigate salt precipitation in the adhesive aggregates discussed in Chapter 4. For images that was found to be enriched by solute from visual inspection, I segmented them into pore-solid-salt ternary structure and analysed the relationship between the salt crust and the pore sizes.

5.2. Materials and methods

This is the continuation of Chapters 3 and 4. All experimental procedures, including crop growth, soil sampling and their X-ray imaging, were the same. In brief, visual inspection of the grayscale images of all aggregates found salt crusts only in two images, indicating that

root water uptake was selective rather than uniform along the root, and that the ion-filtering by the root resulted in salt precipitation as shown in Figure 5.1a.

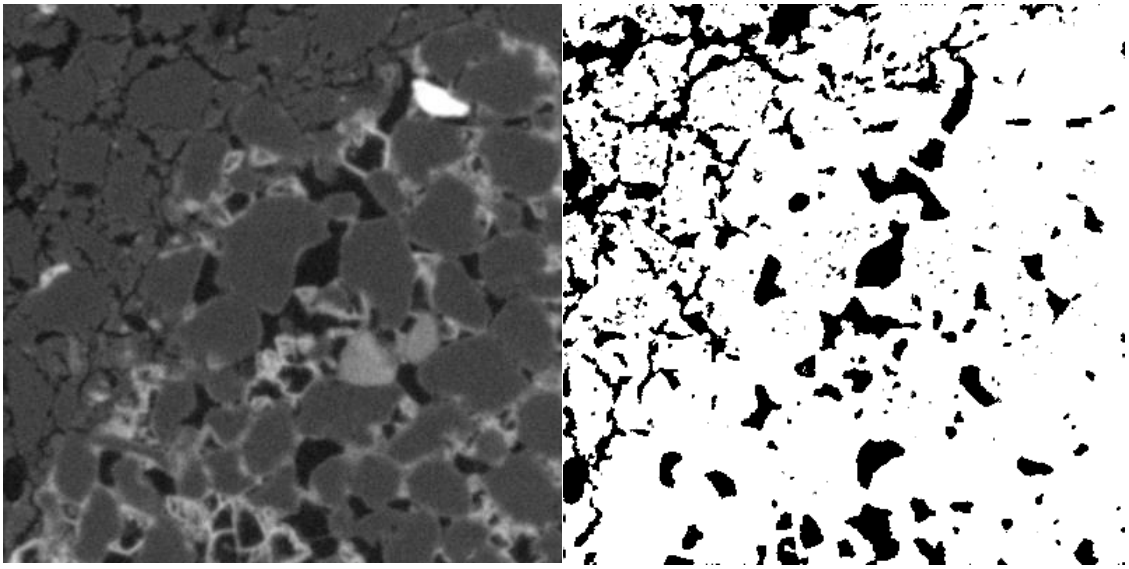

(a) (b)

Figure 5.1. The original grayscale scale X-ray image (a), and its segmented image (b).

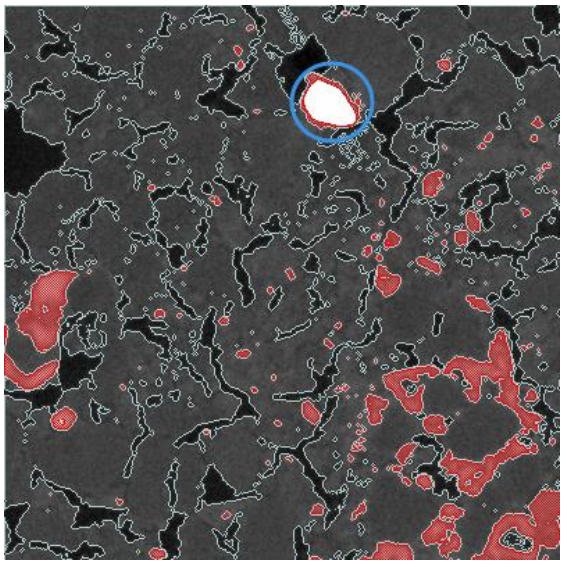

Figure 5.2. The salt crusts in the soil were separated as salt thin film (inside the blue circle) and the salt agglomerates (red-filled areas).

5.2.1 Image analysis

Processing the image with existence of salt crusts is similar to the analysis of the soil images discussed in Chapter 4, except that there are three phases to be separated: pores, salt crusts and soil matrix. Depending on their location and growth, the salt crusts can be further separated into “crystal salt” which grew into agglomerates from the pore walls, and “attached salt” which were the thin salt films attached to the pore walls, as shown in Figure 5.2.

The method used to separate the salt crusts was similar as the methods used in Chapter 3 to map the roots. In brief, the salt agglomerates were mapped out first using Huang’s global threshold method, while the thin salt films were segmented manually using the “magic band” method to mark the interface between the salt film and the soil matrix using a threshold which was adjusted until all slat films were mapped out as shown in Figure 5.2. Areas where salt precipitated was void space prior to the salt precipitation. To determine the pores to which the salt preferred to precipitate, I merged the pore space segmented using the method in Chapter 4 and the salt crusts segmented using the methods just discussed. Figure 5.3 shows the procedure, in which the green-filled areas are pores and the red-filled areas are salt crusts, with others being soil matrix. Combination of the pores and salt crusts was represented by blue in the figure. To calculate the size of the pores prior to salt precipitation, I combined the salt crusts and pores into one phase and embedded it into the original image to make a binary image as shown in Figure 5.3e. The pore-size distribution of the original pores before salt precipitation was calculated using the method discussed in Chapter 4.

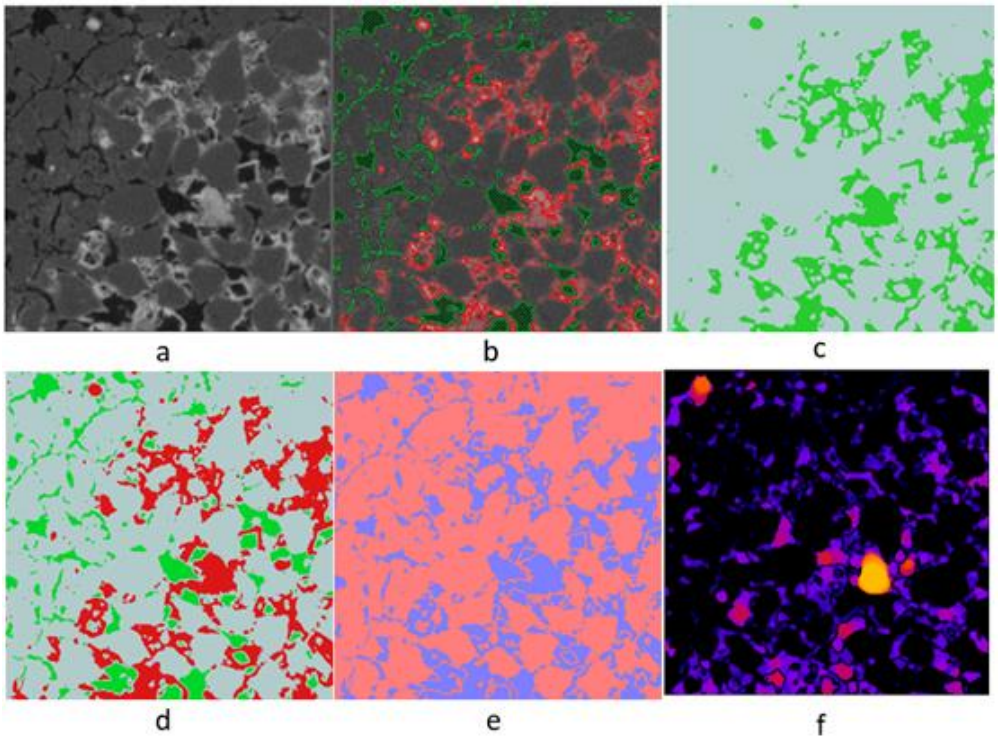

Figure 5.3. Schematic showing the procedure of calculating the sizes of the pores before salt precipitation. The original grayscale image (a); the grayscale image after the pores and salt crusts are mapped out (b); after all pores were re-filled (c); re-filling the salt crusts and embedding it into the image (d); after the salt crusts and pores were merged (e); result of the pore-size distribution with pore size increasing from the dark to bright yellow (f).

5.2.2. Calculating salt crust consent

For salt crusts in each pore, I calculated their volumetric fraction - defined as the ratio of the volume of the salts in the pores with the same diameter to the volume of all such pores. As an illustration, Figure 5.4 takes pores with a diameter in the range of 20-30 μm as an example, explaining how this was calculated. I first took all salt voxels out and embedded all pores with the diameter in the range of 20-30μm into it. The overlapped areas are the salt crusts that had precipitated in the pores with diameter in this range. The volumetric fraction of the salt crusts in the pores with this specific diameter was calculated from

$$s = V_d / V_{salt} \qquad (5\text{-}1)$$

where V_d is the volume of the salt in the pores with a diameter D, and V_{salt} is the total volume of the salt crusts in the image.

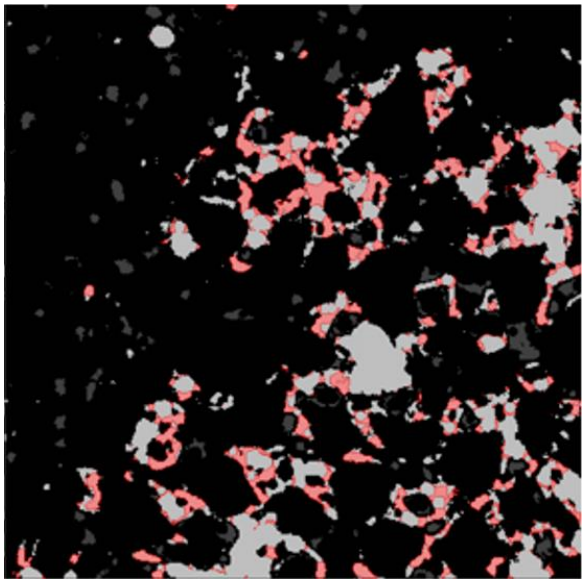

Figure 5.4. Schematic illustration of the calculation of the volumetric salt content in specific pores. The grey and pink areas represent salt crusts, and the pink areas are pores with a diameter in the range of 20-30μm.

5.3. Results

The method used for salt segmentation can successfully separate the precipitated salt from the pore and soil matrix. Water flow and solute transport in the aggregate were regulated by the spatial connection of the pores of different sizes when the aggregate was drying, and Figure 5.5 shows a ternary structure in three-dimensions after segmenting the pores, salt crusts and soil matrix. Figure 5.6 plots the volumetric ratio of the salt crusts to the diameter of the pores in which the solute precipitated. It is evident that with the pore size increasing, the relative volume of the salt precipitated in it decreased, indicating that the dissolved solute had migrated into small pores before its enriched concentration reached its solubility as the aggregate desiccated. Figure 5.6 reveals that the salt crusts existed on the

walls of some large pores, and I used the volume of the whole pore to calculate the volumetric ratio of the salt crusts.

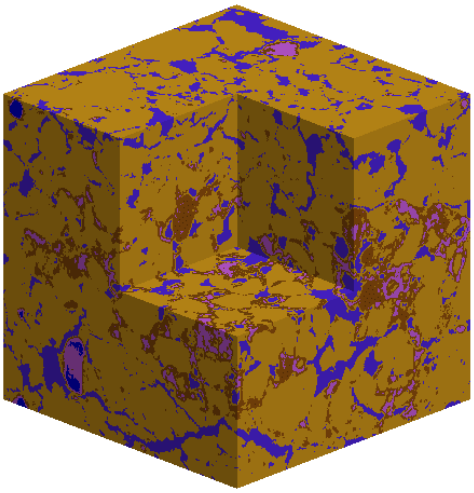

Figure 5.5. 3D ternary structure with the solid matrix (yellow), the air-filled pores (blue), the salt-filled pores (pink) and salt precipitated on the pore walls (brown).

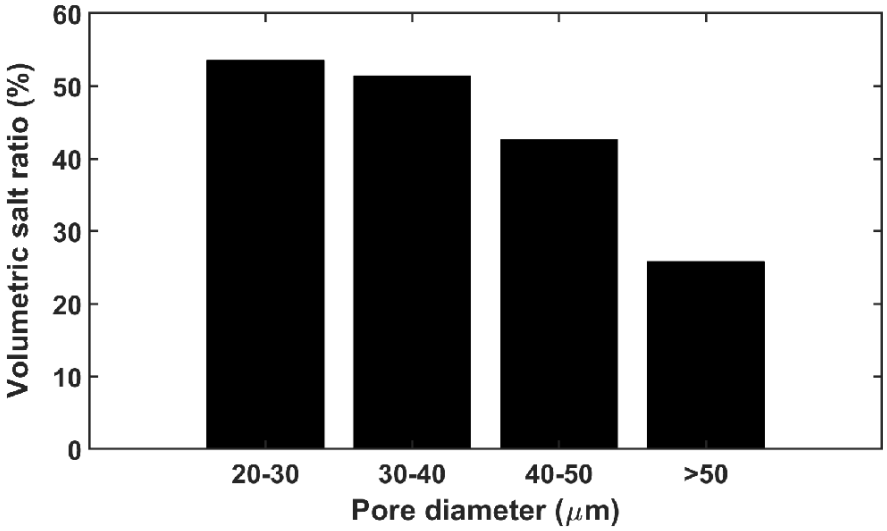

Figure 5.6. The change in ratio of the volume of salt crusts to the volume of pores in which the solute precipitated.

5.4. Discussion

Visual inspection found salt crusts in two of all aggregates although only a tiny salt crust was found in one of the two images, suggesting that a significant amount of dissolved solute had migrated into these aggregates before the root was extracted from the pot. Since maize is halophytic and the site from which we collected the soil is free of salinity, it is almost certain that the salt crusts in the aggregate were the salt we added deliberately as the stress and that the solute enrichment was the consequence of localized root water uptake.

The identified salt crusts were formed when dissolved solute precipitated as the aggregate desiccated. This differs from soil drying induced by root uptake, which takes place only at the aggregate-root interface and does not involve water evaporation. Therefore, the ensuing solute enrichment associated with soil-drying by root uptake occurs at the root-soil interface and is quicker in large pores than in small pores because water flow and ion-filtering in the former are faster than in the latter. In contrast, during air-drying, large pores lose water first, and the solute thus enriches at the water-air interface within the large pores. As such, the relationship between solute precipitation and pore size under air-drying is unlikely to be the same as that caused by root water uptake. This explains why salt crusts were also found on the walls of some pores (Figure. 5.5).

X-ray images identified salt precipitation only in two aggregates, but this does not mean that there was no solute enrichment in other aggregates. Solute enrichment is associated with root uptake, and its relative significance depends on root water uptake rate and where the root takes up water. It has been known that roots do not take water uniformly from their

distal end to proximal end, but there is a paucity of research about the exact water uptake pattern along a root because of the difficulty associated with its direct measurement. Indirect methods based on inverse calculation from neutron imaging and tracer technology has shown variation in root uptake rate along a root (Ahmed et al., 2016), consistent with our findings. Solute enrichment leads to an increase in osmotic potential, thereby reducing root water uptake, especially by root hairs which absorb water actively. One interesting question arising from this work which deserves further research is, if roots compensate for the lost water uptake due to the increased osmotic potential by increasing water uptake from other parts by biologically adjusting its radial hydraulic conductivity.

5.5. Conclusion and summary

Aggregates adhering to a maize root were harvested 14 days after saline water irrigation, and the interior structure of each aggregate was scanned using X-ray tomography at a resolution of 4μm following air-drying. We visually check possible salt crusts in all images and then segmented them. We segmented those with visible salt crusts to ternary structure. The results showed that among the nine aggregates we scanned, only two show visible salt crusts, proving, indirectly, that water uptake along a root is nonuniform and that the root appeared to have taken up water from one region more substantially than from other regions. Our findings have an important implication in root uptake modelling, although incorporating these into the model needs continued effort.

Chapter 6. Impact of long-term management on soil structure and its physical function

6.1. The long-term experiment

The Highfield ley-arable long-term experiment was established at Rothamsted Research, Harpenden, UK (51.80N 0.36W, as shown in Figure 6.1) in 1949 in a field that had been under perennial grass since at least 1838, aimed to investigate the impact of changes in cropping systems on crop yield and dynamic of soil organic matter. Overall, there are six treatments in 50m×7m plots arranged randomly over four blocks. The details of the experiments were available in the literature. My work focused on two cropping systems: perennial grass system dominated by rye grass (*Lolium perenne L.*) and the continuous winter wheat system (*Triticum aestivum L.*). Ten years after the ley-arable experiment was established, a trapezoidal grassland area approximately 900 m^2 adjacent to the experiment site was ploughed and since then, it has remained as bare fallow by mouldboard ploughing and cultivating two to four times per year to 0.23m depth in the same ploughing as in the continuous winter wheat system (Barré et al., 2010). A further adjacent narrow strip approximately 100m×5m and 30m from one end of the bare fallow treatment has had a similar long-term management history. These two bare fallow strips with the same soil type provide a baseline to investigate how the change in cropping systems had alerted soil structure and soil functions. Spatial arrangements of the three treatments and how the soils under different treatments look like now are shown in Figure 6.1.

Soil texture on the site varies slightly with depth. The soil texture in the top 0-18cm and 19-30 cm is similar, with 56%-59% of silt, 26%-29% of clay and 15% of sand, and a pH of 4.8-4.9. But their organic matter differs, with organic matter content in the top 0-18cm soil being 8.2% compared to the 6.0% in the 18-30cm soil. The soil in 30-60cm differs from the topsoil in its texture, with 32% of silt, 63% of clay and 5% of sand. Its pH and organic matter content are 5.6 and 4.5% respectively.

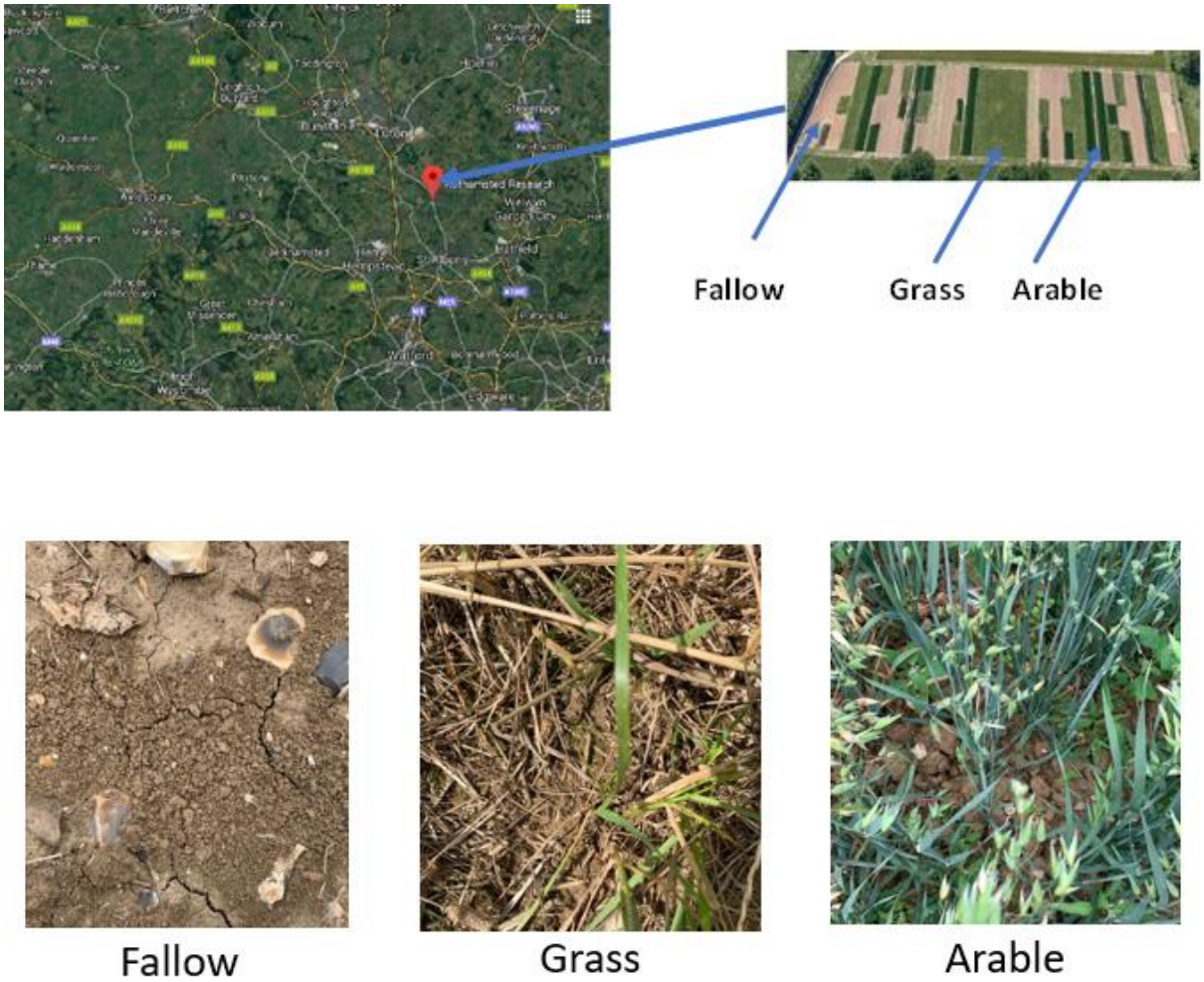

Figure 6.1. The aerial map of the Highfield long-term experiment (left map in the top panel); the spatial arrangement of the treatments (right map in the top panel); and how the soils under different treatments look like now (the bottom panel).

Rainfall and other meteorological data have been measured on the site since 1853 and 1873 respectively. The annual rainfall from 1971 to 2000 varied from 380 mm to 973 mm with an annual average of 704 mm (Johnston and Poulton, 2018). The observed data from the site reveals that the average atmospheric temperature from 2006 to 2011 had risen at an annual rate of 0.46ºC, which was far higher than the annual rising rate of 0.082ºC measured from 1878 to 1988 (Hansen and Sato, 2016). It also found that there have been considerable changes in chemical components of the rainfall since 1850.

6.2. Soil Sampling

Soil samples were taken from the field in October 2015. The locations of the sampling were chosen randomly from the plots for each of the three treatments: fallow, permanent arable, and perennial grass. We used plastic cores, each 120mm high with an internal diameter of 68mm, to sample the soil. The core was hammered into the soil gently from the soil surface, and we then carefully removed the adjacent soil using a trowel ensuring that the soil inside the core was not disturbed. The core was then dug out, with the loose soil on the top of the core gently peeled off using a sharp knife before being tightly wrapped it using a plastic film. We took four replicas from each plot in the grass and arable treatments, and three replicates from the bare fallow treatment. Overall, there were 11 cores. All cores were taken in the same days and they were then transported into a storeroom at Rothamsted.

6.3. X-ray imaging

To keep the soils in the cores not collapsed, they were all watered to approximately the field capacity prior to being scanned using a Phoenix v|tome|x M scanner in the University of

Nottingham. All cores were scanned with voltage 160 kV and current of 180 μA, and their resolution was 40μm; the details of the core imaging was given in (Bacq-Labreuil et al., 2018a), and the focus of my work was the aggregates which were obtained as follows.

After scanning each core, it was manually broken and then passed through 4, 2 and 0.71mm mesh-size sieves shaken under 300 rotations min^{-1} for 3 minutes. Three aggregates between the sieves of 2mm and 0.71mm were selected randomly from each core. They were then scanned using a Phoenix Nanotom in the University of Nottingham under voltage 90 kV and current 65 μA. A total 1440 projection images were taken approximately one hour to scan one aggregate, and its resolution was 1.51μm. Each aggregate was scanned twice due to the limitation of the sample holder size. The raw data for all aggregates were reconstructed using the software Phoenix Datos|x2 rec, and we used the VG StudioMax® 2.2 to combine and assemble the two parts of the image obtained from each scan. Each constructed image was outputted as a stack of grayscale 2D slices. As described in the previous chapters, each image was optimized and segmented before segmenting the images into a binary structure.

6.4. Physical properties of the soils

For each image, I calculated its pore-size distribution, saturated permeability, water retention and the unsaturated permeability.

6.4.1 Pore size distribution (PSD)

The size of each pore was still defined as the diameter of an inscribed sphere that just fits in the pore. The histogram of these diameters is called pore-size distribution. For each

segmented image, I calculated its pore size distribution using the Bone J plugin for ImageJ, and the details were given in Chapter 4.

6.4.2. Saturated hydraulic conductivity and permeability

The permeability of each aggregate was calculated from pore-scale simulation of fluid flow using the lattice Boltzmann (LB) method as explained in Chapter 4. In short, fluid flow in each aggregate was driven by a pressure gradient and the code simulated the flow to steady state. Once flow was deemed to have reached the steady state, judged when the relative difference between the fluid velocity in all voxels simulated at two times points separated by 100 steps was less than 10^{-7}, the fluid velocity and pressure at all voxels were sampled. They were then volumetrically averaged over the cross section normal to the pressure gradient direction to calculate the permeability and hydraulic conductivity using the formulae detailed in Chapter 4.

6.4.3. Water retention curves

Water retention curve is a soil parameter quantifying the ability of a soil to retain water at different conditions represented by matric potential; the dyer the soil is, the higher the matric potential is. The matric potential is also called capillary force and is related to pore size. Water distribution in a soil is controlled by both pore size and how pores of different sizes are spatially connected. There are different methods to calculate water distribution in soil and in this work, we used a simplified geometrical method to calculate water distribution based on the pore size and spatial connection of the pores. Following the pore size

distribution calculation for each image as discussed above, I analysed the pores of different sizes and their spatial location as shown in Figure 6.2.

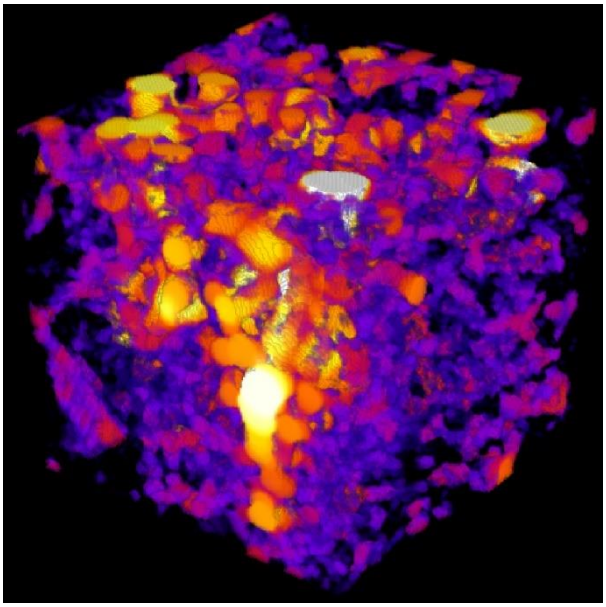

Figure 6.2. Locations and connection of pores of different sizes. The pore size increases from blue to bright yellow, and the soil matrix is made transparent.

Once spatial location of all pores is determined as shown in Figure 6.2, I mimic the lab experiment by putting the sample on a tension table as shown in Figure 6.3. The image was assumed to be initially saturated; a pulling pressure (suction) is applied to the bottom of the image pull the water out. If the pulling pressure is *p*, only water in some pores could be drained. As we use sphere to measure the pore size, and for a pore with radius *r*, its associated capillary pressure was $p' = 2\sigma / r$, where σ is water-air surface tension (Pa/cm). Therefore, when the pulling pressure is *p*, only pores whose associated capillary pressure is less than *p* ($p' < p$) and that they form a cluster(s) which stretches from the bottom to the top of the image as shown in Figure 6.3 cab be drained. There might be pores whose associated capillary pressure is less than *p* but are isolated and not in the clusters; such pores cannot be

drained. Once all water was drained, the water distribution and water content associated with the pulling pressure were calculated. I then increased the pulling pressure incrementally to repeat the above procedure until no more water could be drained out of the image. The relationship between the pulling pressure *p* and its associated water content is called water retention curve of the soil. I simulated the water retention curves for all aggregates using the in-house codes developed by Rothamsted Research.

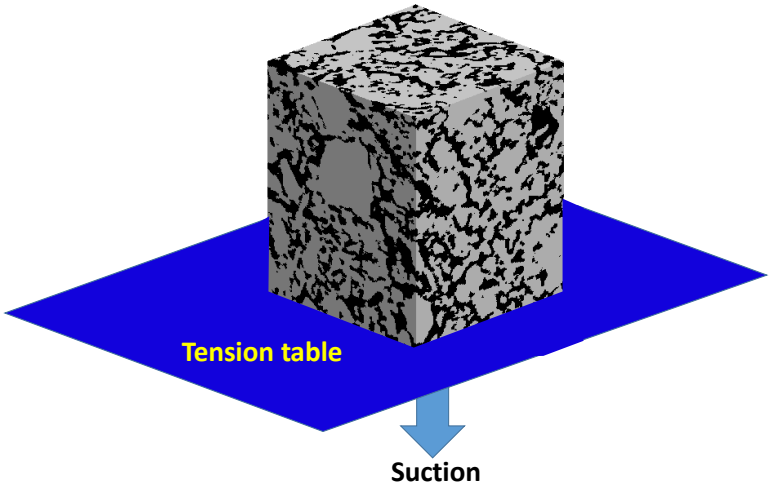

Figure 6.3. Numerical method mimicking the lab experiment to calculate water distribution in soil (grey represents solid and black represents pores) as well as water retention curves.

6.5. The results

6.5.1. The pore-size distribution (PSD)

Figure 6.4 compares the PSD of the aggregates in the three treatments. The shape of the PSD curves is approximately the same, with soils taken from all treatments dominated by pores with diameter in the range of 7.5μm to 15μm. The pores with diameter in the range 0-7.5μm under perennial grass is significantly smaller than that under permanent arable and the bare fallow, indicating that the cropping and tillage (present in the arable and bare fallow

treatments, but absent in the perennial grassland) have a long-term effect on the small pores than on the large pores.

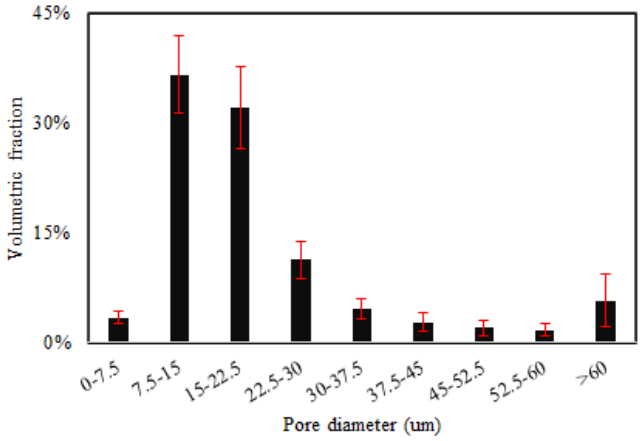

(a)

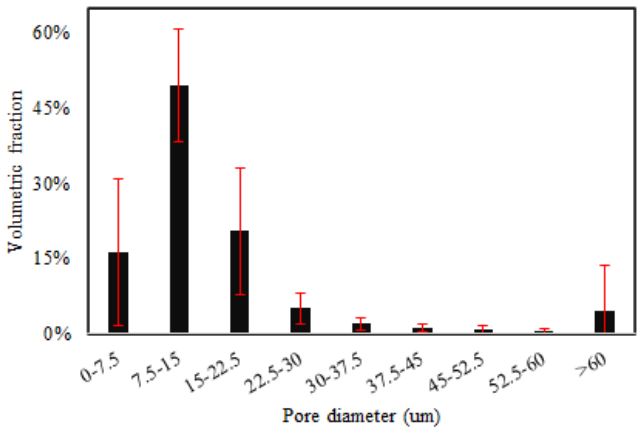

(b)

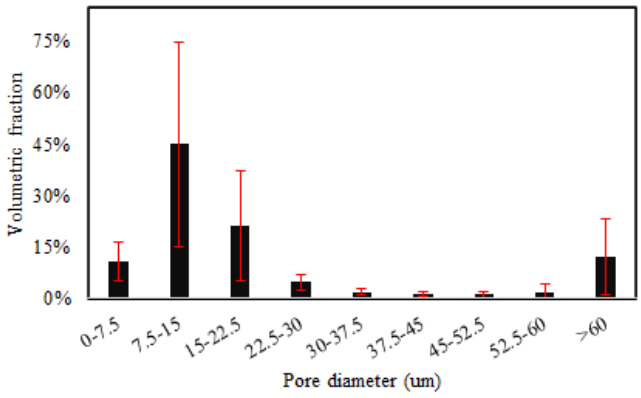

(c)

Figure 6.4. Comparison of PSD of soil aggregates under different treatments. Permanent grass (a), permanent winter wheat (b), and permanent bare fallow (c).

The error bars (standard deviation) in above figures indicate that the aggregates in all treatments are highly heterogeneous with the heterogeneity depending on both pore size and the treatments. For pores with diameter in the range of 7.5-15μm, the aggregates in the bare fallow treatment (Figure 6.4c) is more heterogeneous than those in the other two treatments, especially the aggregates in the arable treatment. For aggregates under the same treatment, pore heterogeneity also varies with pore size. For example, pores with diameters in the range of 0-22.5μm were more heterogeneous than other pores under the arable treatments, while under grass treatment, the pores with diameter in the range of 7.5-225μm were more heterogeneous than other pores.

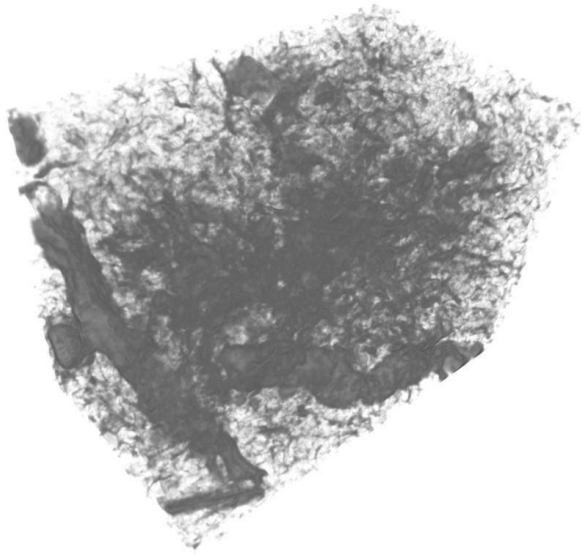

Figure 6.5. A pore network consisting of pores larger than 5 microns only.

Some large pores in the aggregates appear to be the legacy of roots (bio-pores, formed by decay of the root hairs). Figure 6.5 shows a pore network consisting of pores larger than 5μm only in an aggregate taken from the plot under the permanent arable treatment. While

most pores are geometrically complex, there are a few large pores which look geometrically similar to roots, suggesting strongly that they have root origin.

6.5.2. Permeability

As hydraulic conductivity depends on water viscosity and density which changes with temperature and chemical components of the water, I only analysed the permeability which depends on soil structure only. The permeability of a soil depends on both porosity and how pores are spatially connected in it. To elucidate this, I plot in Figure 6.6 the change in permeability with porosity for the aggregates taken from all three treatments. Overall, the permeability of aggregates in the grassland is almost one order of magnitude higher than that in the fallow treatment, with the permeability in the arable treatment in between. I fitted the change in permeability (k) with the porosity (θ) for all aggregates to the following power-law function:

$$k = a\theta^{b} \qquad (6\text{-}1)$$

with the value of parameters, *a* and *b* shown in the figure. The fitting curve describes the increase of permeability with the porosity for the bare fallow and arable treatments reasonably well but underestimated the change of the permeability with the porosity for the perennial grass treatment. This implies that the pores in the aggregates taken from the grassland geometrically differ from that in the aggregates taken from the bare fallow and the arable treatments. The average and the associated standard deviation of the permeability of the aggregates in each treatment is shown in Table 6.1. The increase in permeability with the porosity shown in Figure 6.6 indicates that the porosity is an important factor determining the

permeability, while the deviation from the power-law function suggests that how pores of different sizes are spatially connected is also equally important.

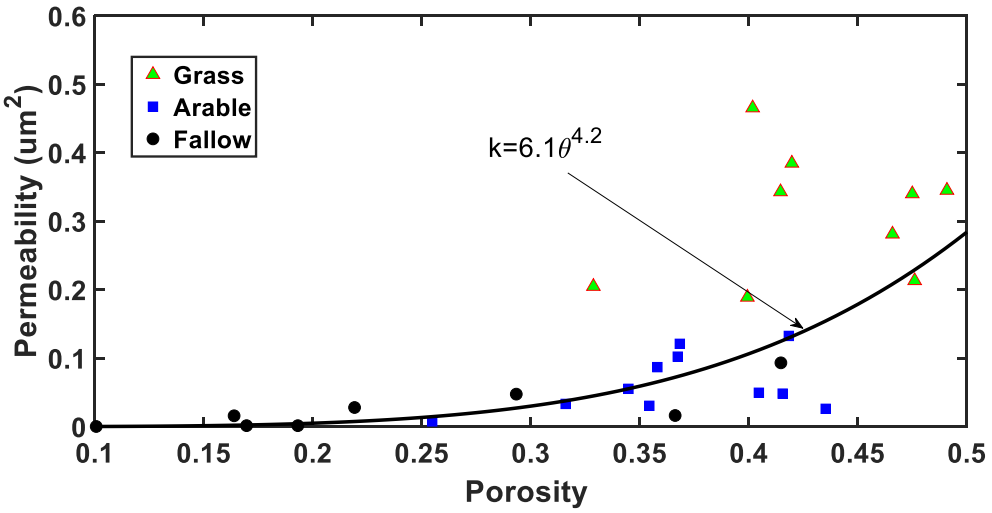

Figure 6.6. The change in porosity and its associated permeability for all aggregates taken from all three treatments

Table 6.1. The mean and standard deviation of the permeability of the aggregates.

	Grass	Arable	Fallow
Mean (μm^2)	0.338	0.063	0.025
Standard deviation (μm^2)	0.13	0.041	0.031

6.5.3. Water retention curves

Figure 6.7 shows an example of water distribution in an image simulated using the method described above under a specific pulling pressure in both three dimensions and two dimensions, respectively. Water distribution is mediated by how pores of different sizes are connected spatially, and it occupies small pores preferentially; this creates a curved water-air interface – meniscus -which similar to part of a spherical surface. It is evident from the figure that the model correctly captures these.

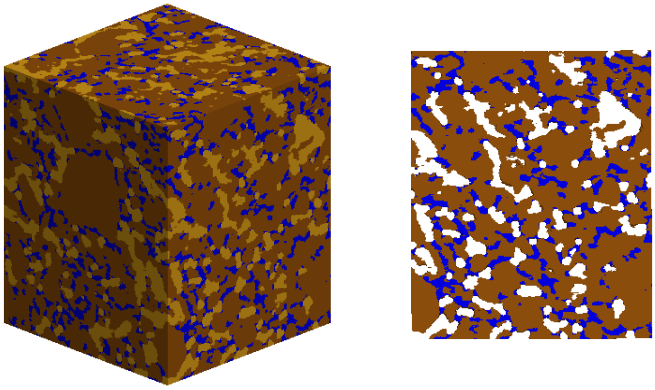

Figure 6.7. An example showing water distribution in the pores simulated using the model. White is air-filled pores, and blue is water and brown is solid.

The pulling pressure used to drain the aggregates is estimated by the radius of the pore size from $p = 2\sigma / r$. For all pores estimated for the image as shown in the pore-size distribution curve, we started draining the soil from the largest pore (r_{max}). Once all possible pores are drained under this pressure, we increased the pulling pressure to drain more water. These proceeded until we drained all pores. As water distribution in the soil is complicated affected by many factors such as the existence of organic matter, this method is approximate, but it correctly captures the impact of the pore geometry on water distribution.

As water-air surface tension affects the capillary pressure, which changes with environment such as temperature and concentration of solute in soil, we normalize the capillary pressure p in our analysis as follows

$$h' = p\delta / \sigma. \qquad (6\text{-}2)$$

where δ is the size of the voxel in the image, and h' is the normalized capillary pressure.

We fit the results for all aggregates to the following van Genuchten formula:

$$\Theta = \Theta_r + \frac{\Theta_s - \Theta_r}{[1 + (\beta h')^n]^{1-1/n}} \qquad (6\text{-}3)$$

where Θ is soil water content, Θ_r is residual water content – the content of water in pores that are isolated and cannot be drained, Θ_r is saturated content – the content of water when soil is fully saturated, β and *n* are parameters – representing how pores of different sizes are spatially connected.

The simulated results (symbols) for aggregates taken from each treatment are shown in Figure 6.8 to Figure 6.10. Also shown in the figures is the best fitting (solid lines) of the van Genuchten formula. The parameters in the van Genuchten formula for the aggregates in each treatment is given in Table 6.2.

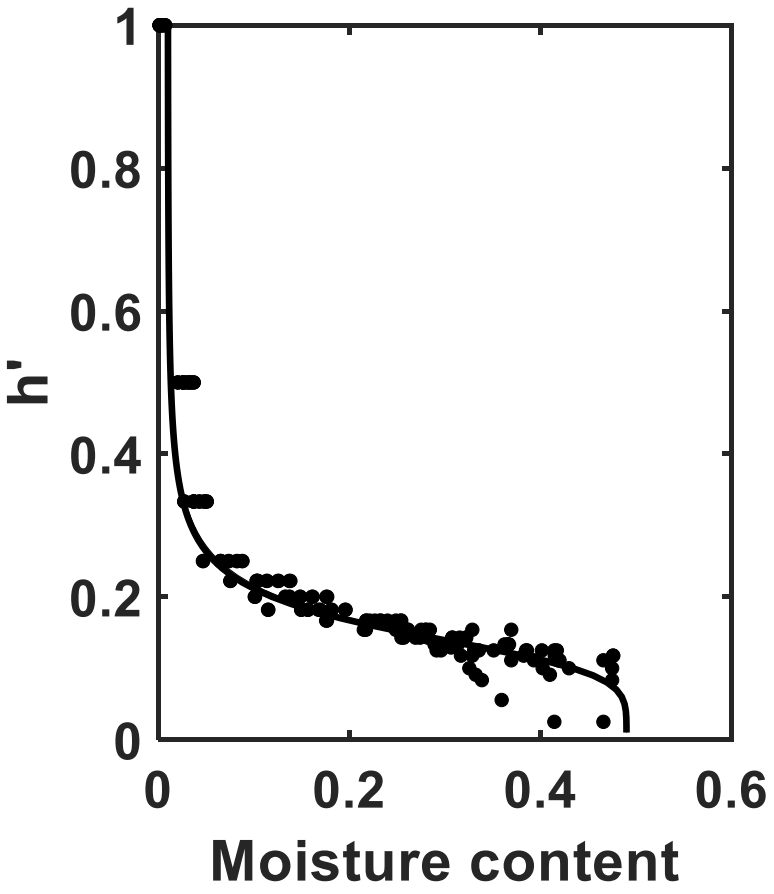

Figure 6.8. The retention curves calculated for all aggregates in the grass treatment.

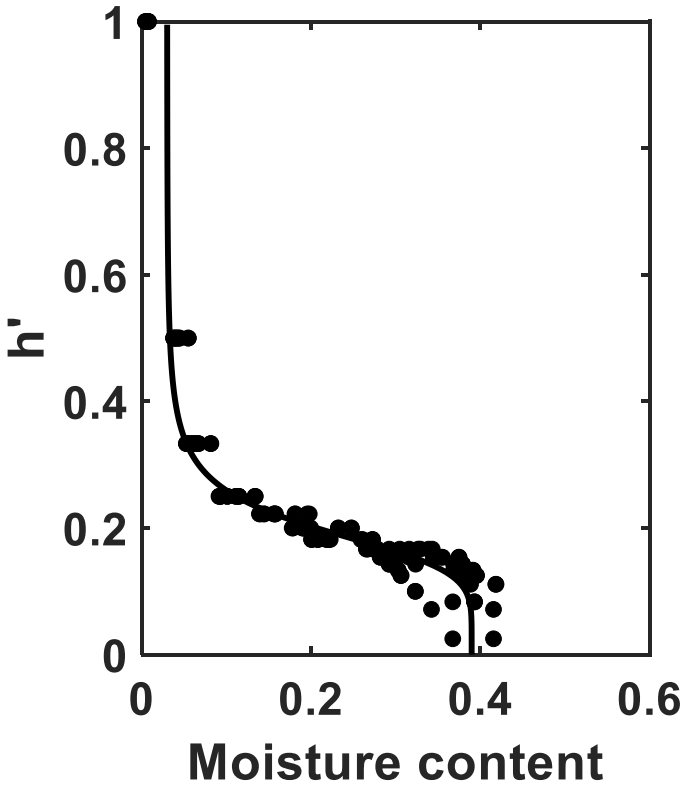

Figure 6.9. The retention curve calculated for all aggregates taken from the arable treatment.

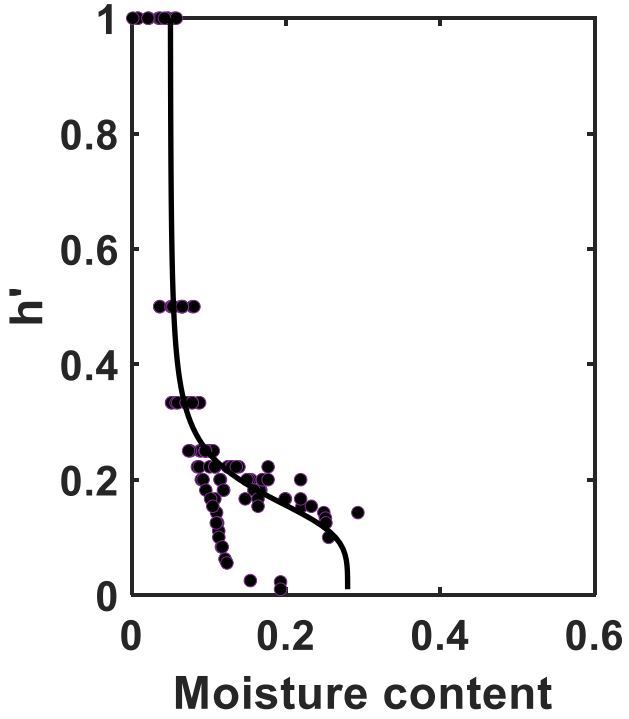

Figure 6.10. The retention curve calculated for all aggregates taken from the bare-fallow treatment.

Table 6.2. The values of the best-fitting parameters

Parameter	Grass	Arable	Fallow
β	6.9	5.1	6.0
n	5.1	5.4	4.6
Θ_s	0.49	0.4	0.28
Θ_r	0.01	0.03	0.05

6.5.4. Unsaturated hydraulic conductivity

Unsaturated hydraulic conductivity is the ability of soil to conduct water when the soil is unsaturated. It is an extension of the Darcy's law for water flow in saturated condition. In unsaturated soil, water flow is still assumed to follow Darcy's law as follows:

$$q = -K(\Theta)\frac{\partial H}{\partial z} \qquad (6\text{-}4)$$

where H is the water pressure head, the sum of water pressure head (less than atmospheric pressure and is hence negative) and elevation potential.

Measuring the unsaturated hydraulic conductivity is very complicated and tedious and in the literature, the common method to estimate the unsaturated hydraulic conductivity is to combine the saturated hydraulic conductivity and the water retention curve estimated from the van Genuchten formula as follows:

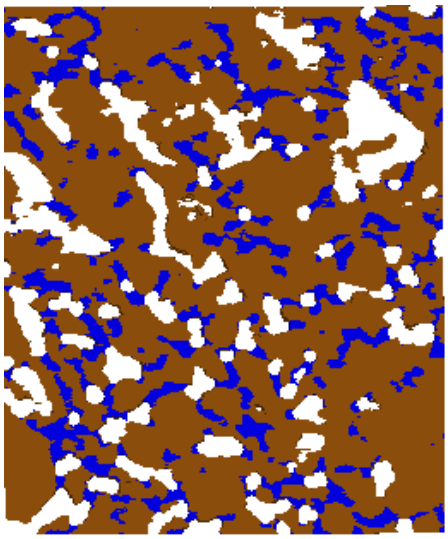

Figure 6.11. Schematic illustration of unsaturated water flows under gravity.

$$\Phi = \frac{\Theta - \Theta_r}{\Theta_s - \Theta_r},$$
$$K(\Phi) = K_s \sqrt{\Phi}\left[1-\left(1-\Phi^{1/m}\right)^m\right]^2, \qquad (6\text{-}5)$$
$$m = 1 - / n$$

where Φ is saturation, Θ_r, Θ_s and n are the parameters in the van Genuchten formula as defined in Eq. (6-3).

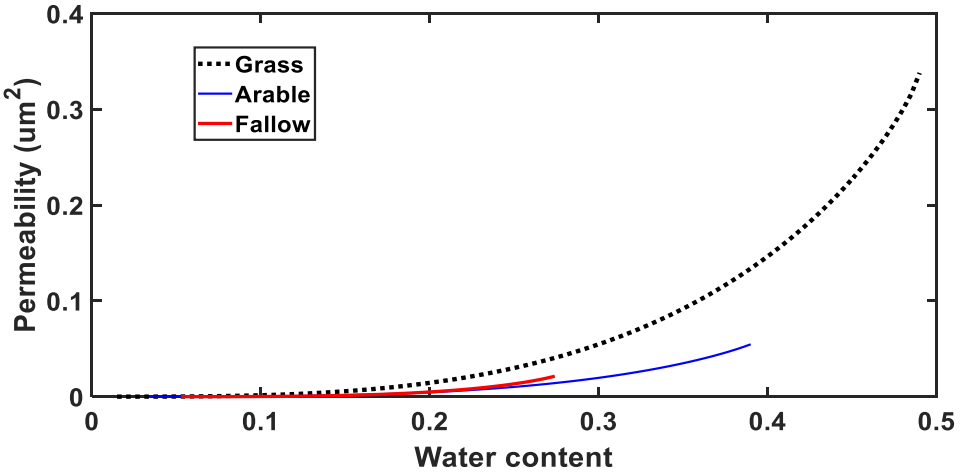

Figure 6.12. Comparison of the change in unsaturated hydraulic conductivity with soil water content for aggregates taken from the three treatments.

Using the values of the parameters estimated for the aggregates in each treatment, we compared the change in unsaturated hydraulic conductivity with water content θ for aggregates in all three treatments; the results are shown in Figure 6.12.

6.6. Discussion

Microscopic analysis based on X-ray tomography revealed that the changes in cropping systems more than 70 years ago had substantially changed the soil structure, which consequently alerted the ability of the soil to retain and conduct water.

Contrasting to the bare fallow treatment that reduced organic matter input into soil, cropping increased both porosity and permeability of the soil aggregates, especially the perennial grassland. Bacq-Labreuila et al. (2018a) studied the same soils. However, due to the limitation of the computer resources, they divided each original image into 16 sub-samples and calculated the permeability of each sub-sample. The permeability of the whole aggregates was calculated as an arithmetic average of the 16 sub-samples. Using the Rothamsted Research software, I used the original image without further subdividing it. The results are thus more accurate and representative. The comparison shows that there is a significant difference between the permeability calculated using my methods with that obtained by Bacq-Labreuila et al. (2018a), with the average permeability calculated using mt method for grass, arable and fallow treatments being 0.338, 0.063 and 0.025 μm^2 respectively, while the associated permeability calculated by the former being 31.0, 23.0 and 14.8 μm^2.

Compared with the bare fallow, the perennial grass increased soil porosity and its associated permeability more than the seasonal arable cropping because the grassland had not been ploughed for at least 100 years. This should keep a large number of bio-pores from being destroyed and is likely the main reason behind the increase in soil porosity permeability. In addition to lack of ploughing, it is suggested that the grassland has a diversity of plants which could make the soil more porous. The relationship between the porosity and permeability for the aggregates taken from all treatments appears to separate the data into two groups: one for the bare fallow and arable soil and the other one for the soil taken from the grassland. The increase in permeability with porosity was fitted to a power law function. Overall, the fitting curve describes the change in permeability with the porosity well for the bare fallow and arable soil, but substantially underestimated the permeability for the grassland treatment.

Annual tillage of the fallow and arable land could reconstruct the soil, making the pores in them geometrically different from those in the grassland soil. This might be the main reason why the permeability – porosity relationship is similar between the fallow and arable soil but differs from the grassland. In addition to these, the porosity and permeability in the bare fallow are more heterogeneous than the arable soil, and comparatively, the grassland soil is more homogeneous. Average permeability for all three treatments follows in the order of fallow < arable < grassland, which is same as the work of Bacq-Labreuila et al.(2018a). However, our results simulated using the original images showed that the average permeability of the arable soil is two times that of the fallow treatment, differing from the

results of Bacq-Labreuila et al.(2018a) which showed that the permeability of the fallow and arable lands does not differ from each other significantly.

In a previous work, Bacq-Labreuila et al (2018a) compared the pore-size distribution. While the pore-size distribution is a function to describe soil structure, water distribution in soil depends on how pores of different sizes are spatially connected. In this paper, we calculated both, from which we calculated water retention curves of all aggregates. The relationship between soil water content and the normalized capillary pressure shows that soil in the grassland appears to be more homogeneous, and the relationship between soil water and the capillary pressure follows almost the same trend in that they differ only slightly at the wet ends (near saturation) associated with large pores. As large pores dry and water content reduces, the water retention curves calculated from all aggregates converges almost to the same line. Similar was also found for the arable soil, in which the water retention curves calculated from all aggregates are very close. In contrast, the water retention for aggregates of the fallow treatment varies widely, implying that cropping makes soil more homogeneous.

Under the same water content, the hydraulic conductivity of the grassland soil is almost one order of magnitude higher than that of the arable land and fallow soil. As permeability of soil depends on pore size and how pores are connected, the increase in permeability in the grassland under the same water content implies that the pores in grassland are less tortuous. This is similar to the results of Bacq-Labreuila et al.(2018a) who used the Euler's number to quantify the connectivity of different pores.

6.7. Conclusions

This chapter analyses the X-ray images of aggregates taken from different cropping systems and a bare-fallow treatment which have been in operation for more than 70 years. From each aggregate image, I segmented it and then calculated its pore geometry, including pore-size distribution and how pores of different size are spatially connected. I also calculated the permeability and water retention of each aggregate using the in-house codes developed by Rothamsted Research, finding that the both perennial grass and arable cropping increased the porosity and permeability, compared to the soil under long-term bare fallow. The relationship between porosity and permeability for the bare fallow and the arable soil follows the same trend and can be fitted to the same power-law function, while the permeability of the grassland soil was much higher than that predicted by this power-law function. When capillary pressure is high, the water held in soil under different treatments is comparable, but with the matric potential decreasing and soil becoming wet, the arable and grassland soil holds more water. In addition, the cropping systems appear to have made the soil more homogeneous and the water retention curves calculated for their aggregates follow the same trend. It was also found that under the same water content, the grassland soil is more permeable than the bare fallow and arable soils.

Chapter 7. Impact of soil structure on solute diffusion coefficient

7.1. Introduction

Soil aggregates in the field are normally at saturated condition, and gases in soil mainly flows through the large pores between the aggregates. For example, gaseous oxygen in the atmosphere normally moves into the soil through inter-aggregate pores and then dissolves at the water-air interface before moving into the aggregates to sustain microbial activity which controls almost all soil functions. When oxygen inside the aggregates is insufficient to support microbial respiration, the microbes will use other elements as electron acceptors creating an anoxic environment. Also, fertilizers applied on the soil surface move into the soil through these inter-aggregate pores first and then migrate into the aggregates. For aggregates far away from roots, the impact of root water uptake is minor and solute movement in such aggregates is driven largely by molecular diffusion. Therefore, the ability of aggregates to diffuse soluble solute is important for soil functions. The objective of this chapter is to investigate how the cropping system changes as discussed in Chapter 6 affect the ability of the aggregates to diffuse solute.

7.2. Effective diffusion coefficient

Soluble solute in water moves from high-concentration area to low-concentration area driven by molecular diffusion. The diffusive flux depends on concentration difference between the two areas as illustrated in Figure 7.1.

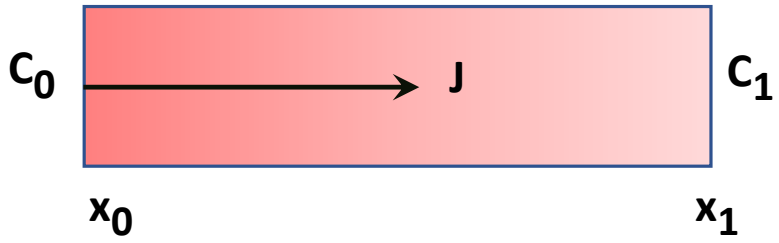

Figure 7.1. Schematic showing solute diffusion driven by concentration gradient.

For solute diffusion driven by concentration gradient in a tube filled with saturated soil as illustratively shown Figure 7.1, when the diffusion is at steady state, the diffusive flux flowing from the high concentration end (C_0) to the low concentration end (C_1) is

$$j = \frac{J}{A} = -D_e \frac{C_1 - C_0}{x_1 - x_0} \tag{7-1}$$

In the limit, Equation (7-1) can be written as the following Fick's law:

$$j = \frac{J}{A} = \lim_{x_0 \to x_1} -D_e \frac{C_1 - C_0}{x_1 - x_0} = -D_e \frac{\partial C}{\partial x} \tag{7-2}$$

where D_e is the effective diffusion coefficient of the soil. Similarly, measuring the effective diffusion of a soil needs a large soil sample, which is impossible for the aggregates I studied. I hence calculated the effective diffusion of each aggregate based on pore-scale simulations.

7.3. Calculating effective diffusion from pore-scale simulation

To estimate the ability of the aggregate to molecularly diffuse solute, I calculated its effective diffusion under saturated condition. For each aggregate, the pore-scale simulation is to mimic the experimental setup in Figure 7.1 by imposing a high concentration on one side

and a low concentration on its opposite side of the aggregate. The solute moves through the pores filled by water, and its movement is described by the following equation:

$$\frac{\partial c}{\partial t} = D\left(\frac{\partial^2 c}{\partial x^2} + \frac{\partial^2 c}{\partial y^2} + \frac{\partial^2 c}{\partial z^2}\right) \tag{7-3}$$

where c is solute concentration in the pore space, and D is the molecular diffusion coefficient in water, t is time and x, y and z are the coordinates.

Similar to pore-scale simulation of water flow, initial solute concentration in the pore-scale simulation of solute diffusion also zero in the pore space. Solute diffusion was instigated by imposing a concentration gradient in one direction, and I then simulated solution diffusion to steady state. In all simulations, Eq. (7-3) was solved numerically using the finite volume method. Each voxel in the image has six sides, and the finite volume method first calculates the diffusive fluxes flowing in/out of the voxel from each of its six sides, depending on whether the side is solid or water-filled voxels. Figure 7.2 illustratively explain method. I use *o* (hidden in the figure) to represent the voxel being analysed which is bordered by six voxels represented by *d*, *s*, *w*, *e*, *u* and *n* (hidden in the figure) respectively.

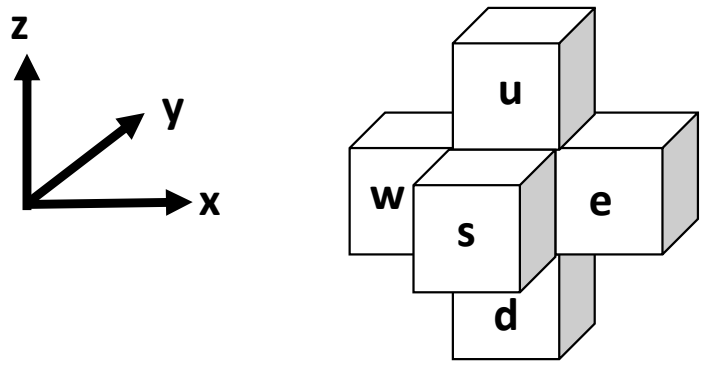

Figure 7.2. Stencil of the seven voxels in the numerical method (voxel o and n are hidden)

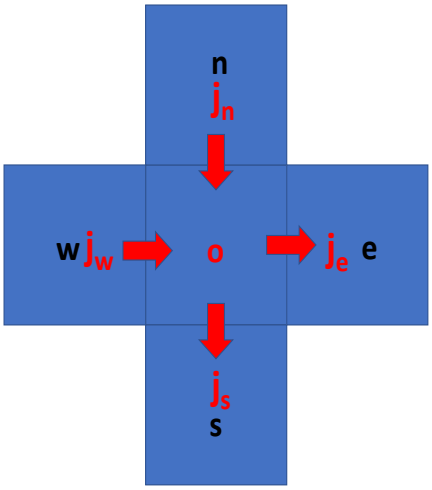

Figure 7.3. Illustration of calculation of the solute fluxes in the *x*-*y* plane.

The solute movement between the voxel *o* and its six neighbours is described by Eq. (7-1). Taking the five voxels in the *x*-*y* plane as shown in Figure 7.3 as an example, there are four fluxes: j_s, j_w, j_e and j_n; they are calculated as follows assuming the side-size (the resolution of the voxel) of all voxels is δ:

$$
\begin{aligned}
j_s &= \begin{cases} D\dfrac{c_s - c_o}{\delta} & \textbf{\textit{if voxel s is pore}} \\ 0 & \textbf{\textit{f voxel s is solid}} \end{cases} \\
j_w &= \begin{cases} D\dfrac{c_w - c_o}{\delta} & \textbf{\textit{if voxel w is pore}} \\ 0 & \textbf{\textit{f voxel w is solid}} \end{cases} \\
j_e &= \begin{cases} D\dfrac{c_s - c_o}{\delta} & \textbf{\textit{if voxel e is pore}} \\ 0 & \textbf{\textit{f voxel e is solid}} \end{cases} \\
j_n &= \begin{cases} D\dfrac{c_s - c_o}{\delta} & \textbf{\textit{if voxel n is pore}} \\ 0 & \textbf{\textit{f voxel n is solid}} \end{cases}
\end{aligned}
\qquad (7\text{-}4)
$$

For solute movement between voxel *o* and voxels *d* and *u* in the x-z plane, the associated fluxes can be calculated similarly as follows:

$$j_d = \begin{cases} D\dfrac{c_d - c_o}{\delta} & \textbf{\textit{if voxel d is pore}} \\ 0 & \textbf{\textit{f voxel d is solid}} \end{cases}$$
$$j_u = \begin{cases} D\dfrac{c_w - c_o}{\delta} & \textbf{\textit{if voxel u is pore}} \\ 0 & \textbf{\textit{f voxel u is solid}} \end{cases} \qquad (7\text{-}5)$$

where c_o, c_s, c_w, c_e, c_n, c_d, c_u are the concentrations of solute in voxels *o*, *s*, *w*, *e*, *n*, *d* and *u* respectively. Since the voxel is cubic, the cross-section through which the solute moves in all direction is $A = \delta \cdot \delta$. During one time period from t_0 to t_1, the mass of solute moving into and out of the voxel o is

$$\Omega = A \cdot \left(j_s + j_w + j_e + j_n + j_d + j_u \right) \Delta t, \quad \Delta t = t_1 - t_0. \qquad (7\text{-}6)$$

Before solute movement reaches steady state, $\Omega \neq 0$, and the concentration in voxel o thus changes with time. I assume that the concentration in voxel o at time t_0 is c_0 and the concentration at time t_1 is c_1. Since the volume of voxel o is $V = \delta^3$, the mass change in the voxel o during Δt is

$$\Delta m = \delta^3 \left(c_o^{t_1} - c_o^{t_0} \right) \qquad (7\text{-}7)$$

The mass balance requires

$$\Delta m = \Omega \qquad (7\text{-}8)$$

That is;

$$\delta^3 \left(c_o^{t_1} - c_o^{t_0} \right) = \delta \cdot \delta \cdot \left(j_s + j_w + j_e + j_n + j_d + j_u \right) \Delta t \qquad (7\text{-}9)$$

The concentrations c_o, c_s, c_w, c_e, c_n, c_d, c_u for calculating the six fluxes in Eqs. (7-8) and (7-9) take the concentration at time t_0, which is assumed to be known. Therefore, the concentration at time t_1 at the voxel o can be calculated from

$$c_o^{t_1} = c_o^{t_0} + \frac{D}{\delta}\left(c_s^{t_0} + c_w^{t_0} + c_e^{t_0} + c_n^{t_0} + c_d^{t_0} + c_u^{t_0} - 6c_o^{t_0}\right)\Delta t \qquad (7\text{-}10)$$

Repeating the above procedures for all pore voxels allows me to calculate their concentration at time t_1. Once the concentration in all voxels at t_1 is calculated, the above procedure was repeated by replacing t_1 by t_0 until the steady was reached. This method is known as explicit method and is stable when $6D\Delta t/\delta < 1$.

All simulations were conducted using a code developed by Rothamsted Research (Li et al., 2018c). In short, for each aggregate image as shown in Chapter 6, at time t_0=0, a constant concentration C_1=1.0 and C_0=0 (mg/l) were imposed on the left-hand side and the right-hand side of the image respectively, with solute concentration in other pore voxels being zero. The code simulated solute diffusion using the above method to steady state, deemed to have been reached once relative difference between the sum of concentration in all voxels at two time points separated by 100 time steps was less than 10^{-6}. Once the solute diffusion was in steady state, the code calculated the diffusive flux and solute concentration in all voxels, and they were then volumetrically averaged over each cross section normal the direction along which the external concentration gradient was imposed. These volumetric average concentration and diffusive flux were assumed to follows the following Fick's law, for example, when the external concentration gradient was imposed in the *x* direction:

$$J = -D_e \frac{\partial C}{\partial x} \qquad (7\text{-}11)$$

where *C* is the volumetric average concentation and *J* is the average diffusive flux in the *x* direction. The average concentation *C* is linearly distributed from the inlet to the outlet when

diffusion reached steady state; the effective diffusion coefficient can thus be calcualetd from Eq. (7-11) as follows based on the pore-scale simulaetd concentration and diffusive flux:

$$D_e = J\frac{L}{C_1 - C_0}$$
$$J = \frac{\sum_{i=1}^{N} j_x(x_i, y_i, z_i)}{N} \quad (7\text{-}12)$$

where N is the number of all voxels and $j_x(x_i, y_i, z_i)$ is the diffusive flux in voxel cantered at (x_i, y_i, z_i), L is the length of the image in the x direction where the external concentration gradient was imposed. Switching the imposed external concentration direction allows users to calculate the effective diffusion coefficient of the soil in other two directions. In what follows, the effective diffusion coefficient of each sample is the average of the diffusion coefficients calculated in its three orthogonal directions.

7.4. Result analysis

For ease of analysis in what follows, for the effective diffusion coefficient I calculated for each aggregate image, I normalized it using the diffusion coefficient of the solute in bulk water. That is, $D' = D_e / D_0$, where D_0 is the diffusion coefficient of the solute in water.

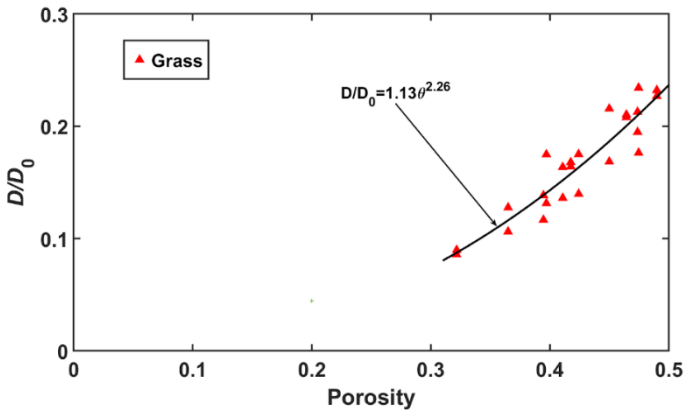

Figure 7.4. Change in the normalized molecular diffusion coefficient with porosity for all aggregates taken from the grassland treatment.

There are 12 aggregates for the grass and arable treatments each, and 9 aggregates for the bare fallow treatment. Because of soil heterogeneity and spatial variation as discussed in Chapter 6, the porosity of the aggregates taken from the same treatment also varies. Figure 7.4 shows the change in porosity of all aggregates taken from the continuous grassland treatment in which the porosity varies approximately from 0.31 to 0.49, while its associated normalized molecular diffusion coefficient varies from approximately 0.1 to 0.24.

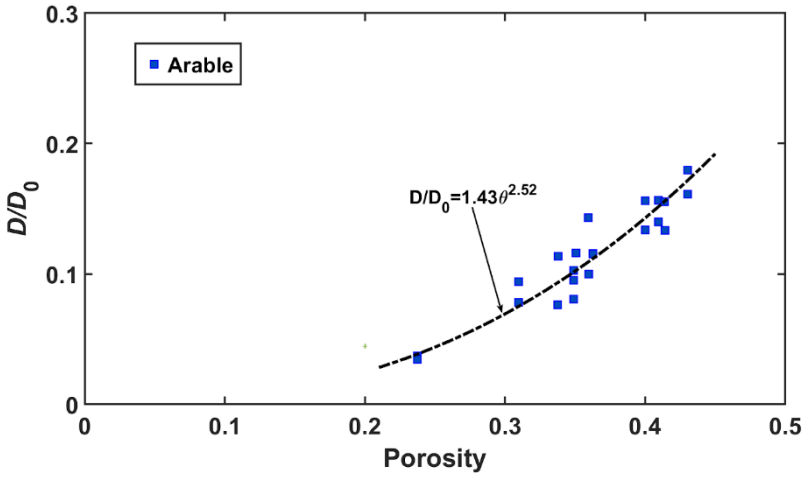

Figure 7.5. Change in the normalized diffusion coefficient with porosity for all aggregates taken from the arable treatment.

In contrast, converting grassland to arable 70 years ago reduced the aggregate porosity considerably. Figure 7.5 reveals that the porosity of all aggregates taken from the arable treatment varied from 0.22 to 0.45. Although the highest porosity is comparable to that of the aggregates taken from the grassland, its lowest porosity (0.22) is much smaller than that of the grassland (0.31), indicating that the arable treatment has made the soil aggregates more heterogeneous. In addition to the reduction in porosity, the ability of the aggregates under arable treatment is also reduced. Figure 7.5 reveals that the normalized effective molecular

diffusion coefficient of the aggregates in the arable soil changed approximately from 0.03 to 0.2, much less than that under the grassland which changed from 0.22 to 0.31. This difference is an interplay of the reduction in porosity and connectedness of the pores of different pores inside the aggregates.

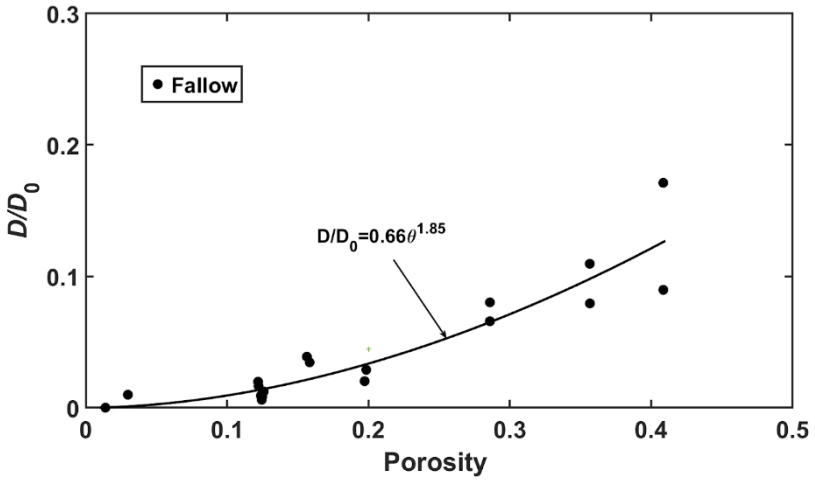

Figure 7.6. Change in the normalized diffusion coefficient with porosity for all aggregates taken from the fallow treatment.

Figure 7.6 shows the change in porosity and the normalized effective molecular diffusion coefficient of the aggregates taken from the bare fallow treatment. Compared with the grassland and arable land, the bare fallow considerably reduced the porosity and the normalized diffusion coefficient of the aggregates. Again, the highest porosity of the aggregates in the bare fallow treatment is approximately 0.4, only slightly less than that of the arable (0.45) and the grassland (0.49) treatment, but its lowest porosity is less than 0.1, far less than that of the grassland (0.31) and arable land (0.22). These differences indicate that fallowing the soil not only makes it less porous but also more heterogeneous due to the reduced carbon input. The normalized molecular diffusion coefficient of the aggregates taken

from the bare fallow varies from 0.005 to 0.17, far less than that of the grassland and the arable land.

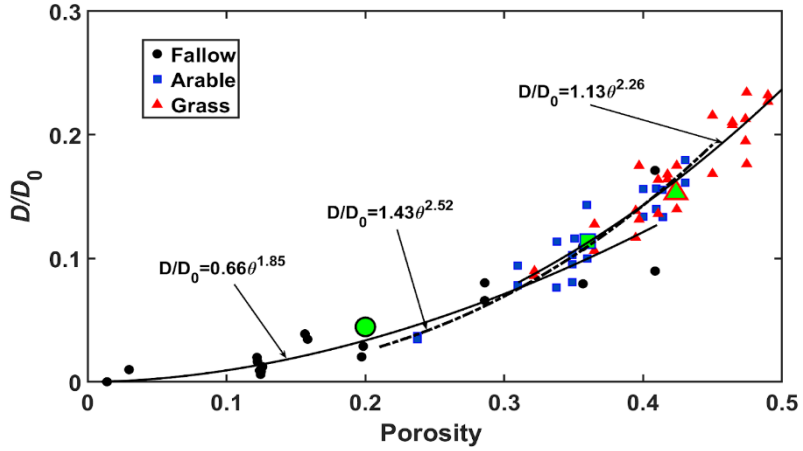

Figure 7.7. Change in the normalized diffusion coefficient with porosity by pooling aggregates taken from all treatments.

The cropping systems in the long-term experiment differed but the soil texture is the same. To elucidate if the change in the normalized molecular diffusion coefficient with the porosity follows the same trend, I pooled the results of the aggregates taken from all treatments and plot them in Figure 7.7. In the figure, the large-green symbols are the average for the associated three treatments. Also plotted in the figure are the best-fitted exponential curves describing the increase in the normalized molecular diffusion coefficient with the porosity for each treatment. It is evident from the figure that the change in the normalized effective molecular diffusion coefficient with porosity differed between the treatments, especially the fallow treatment. The exponent of the curve for the fallow treatment was 1.85, much smaller than that for the arable land (2.52) and the grassland (2.26). This difference indicates that the diffusion coefficient increases more slowly with porosity for the bare fallow treatment than for the arable and grassland treatments.

Soil carbon and nitrogen are two important indicators of soil health, and to unravel how the change in ability of the soil aggregates to transport solute links to soil carbon and nitrogen, I plotted in Figure 7.8 the soil organic carbon in the top 0-20 cm of soil where the samples were taken against the normalized molecular diffusion coefficient for all treatments. It is evident that there is a strong correlation between soil organic carbon in the soil and the ability of the aggregates to transport substrates. The soil organic carbon increases with the effective diffusion coefficient of the aggregates, and the increase is adequately described by an exponential function as shown in the figure. The soil organic carbon data were taken from archive of the long-term experiment, and the detail was given in Gregory et al. (2016).

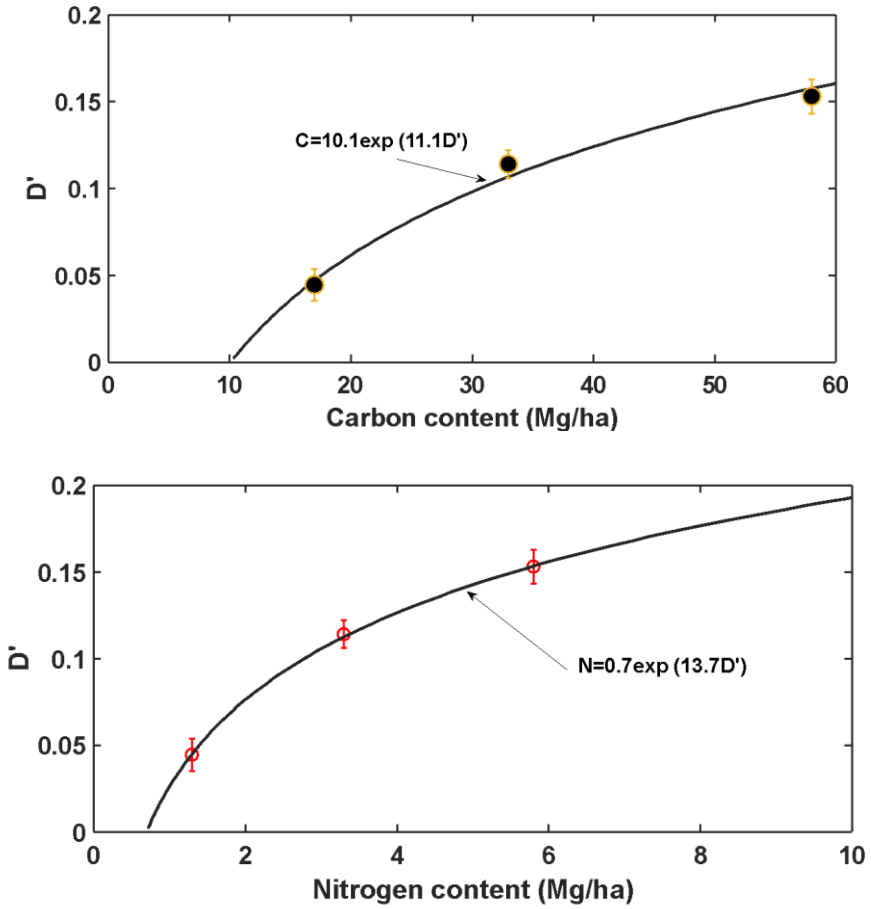

Figure 7.8. The change in normalized molecular diffusion of the aggregates taken from all three treatments with soil organic carbon (a) and nitrogen (b) in the soils.

Soil organic carbon and nitrogen are closely linked, and I also plotted in Figure 7.8 the relationship between total soil nitrogen and the normalized molecular diffusion coefficient of the aggregates. Similar as for the soil organic carbon, the soil nitrogen also increases exponentially with effective diffusion coefficient of the aggregates.

7.5. Discussion

The aggregate structures acquired using X-ray computed tomography and their diffusion coefficient calculated from the pore-scale simulation proved that the porosity of soil and its ability to transport soluble substrates were substantially modulated by cropping system and land management. My results were corroborated by the findings of Guo et al who showed that agronomic management altered carbon input into soil thereby changing soil structure (Guo et al., 2020). While there is an ongoing debate over the use of aggregate as an operational structural unit to describe soil processes, I used this term to represent a sub-scale soil structure which is relevant to microbial activity. Perennial grassland without tillage enhanced soil aggregation and increased soil carbon sequestration (López-Garrido et al., 2011); this is consistent with my results which showed that the grassland soil is most rich in carbon. I also found a strong correlation between soil organic carbon and the ability of the aggregates to transport substrates. Six et al claimed that tillage destroys soil aggregates thereby reducing particulate organic matter (Six et al., 1999). This is again consistent with my finding that soil organic carbon in the arable and bare-fallow treatments is much less than that in the non-tilled perennial grassland.

Changing agronomic practices shifts carbon input to soil thereby alerting the ability of the aggregates to retain and transport substrates, including water (Guo et al., 2020). This is corroborated by our findings although my results showed that such effects are asymptotic in that there is a critical soil organic carbon content beyond which the aggregate structure and its transport properties no longer change with a further increase in soil organic carbon, although my results did not show thus critical carbon content. Perennial grassland had increased aggregate porosity compared with the arable land, consistent with previous studies although the increasing level in my results differ (Naveed et al., 2013). Aggregates taken from the grassland and the arable land were more porous and diffusive than those taken from the bare fallow treatment due to their difference in carbon input (the arable land vs the bare-fallow) and the tillage (grassland vs the arable and bare-fallow).

The formation of stable aggregate is a long process modulated by soil carbon (Jastrow et al., 1996). The measurement from the Broadbalk wheat experiment, 1000m away from the ley-arable experiment but still inside Rothamsted, reveals that soil organic carbon did not stabilize 100 years after switching the fertilization to farmyard manure (Poulton et al., 2018). Therefore, it remains unknown if the soil structure under different treatments at the ley-arable experiment is still in transition or has stabilized.

Organic matter and its associated microbial activity occur only at some hotspots, and the pore geometry inside the aggregate is thus spatially heterogeneous even in the same treatment. The porosity and diffusion coefficient of the aggregates in the arable and grassland treatments appear to follow the same trend, differing from those for the bare fallow treatment.

The transport ability of a soil depends on its porosity as well as how pores of different sizes are spatially connected. The same trend in porosity-diffusion coefficient relationship for aggregates in the grassland and arable land suggests that their pores are geometrically similar, and that the mechanisms underlying the formation of their aggregates are comparable.

An asymptotic relationship between soil organic carbon and the ability of the aggregates to transport substrates was found in my study, meaning that the impact of soil carbon on aggregate structure becomes less important as soil carbon increases. Because both pore geometry and organic matter in the aggregates are spatially heterogeneous, for organic matter which is distant from microbes, the microbes secrete extracellular enzymes to decompose it in order to obtain the nutrients they require. However, because of pore heterogeneity, there is always organic matter which is inaccessible to microbes (Dungait et al., 2012). Therefore, once carbon supply and carbon decomposition within the aggregates balance each other, aggregate structure and the carbon within it reach equilibrium and any further carbon input would not shift this equilibrium. This is likely the mechanism underlying the asymptotic increase in transport ability of the aggregates with soil organic carbon.

Increasing carbon input enhances transport ability of the aggregates, which in turn alters biogeochemical reactions and nutrient cycling. For example, the increased porosity and diffusion of the aggregates in the grassland could make dissolved oxygen and substrates easy to move through, thereby changing nitrogen and carbon cycling and facilitating nitrification (Zhou et al., 2018). This could increase nitrate leaching from the soil (Goulding, 2000).

7.6. Conclusions

Soil samples taken from the long-term experiment at Highfield in Rothamsted, UK show that the changes in cropping system and land management more than 70 years ago altered soil carbon input thereby reshaping soil structure and the ability of the soil to transport water and substrates. Compared with bare fallow, perennial grass and permanent arable cultivation increase carbon input thereby increasing the porosity of the aggregates and their ability to transport substrates. The diffusion coefficient of the aggregate increases with soil carbon asymptotically before plateauing when soil carbon exceeds a critical value although this value does not appear in my results. For aggregates taken from all treatments, their effective diffusion coefficients increase with porosity approximately in a power law, but the increasing trend varies with treatments. For the perennial grassland and the arable land, their diffusion coefficient increases with their porosity almost in the same trend, while the diffusion coefficient of the aggregates in the bare fallow soil varies their porosity differently. This suggests that the interior structures of the aggregates in the grassland and arable land are geometrically similar, distinguished from that in the bare fallow soil. As soil structure controls almost all physical and biogeochemical processes in terrestrial ecosystems and is mediated by soil organic matter, understanding the relationship between soil structure and soil organic matter, as well as their consequence for soil transport ability, is essential to improving nutrient management and agronomical practices.

Chapter 8 Conclusions and future work

8.1. Summary and conclusions

The overarching objective of my project is to investigate soil-root interactions using X-ray and neutron computed tomography at various scales, including the impact of biotic and abiotic stresses on root development in 3D, as well as structure of the rhizosphere using pot experiment. I also studied how cropping systems and land management impact the structure of soil aggregates and their ability to retain and transport substrates, including water.

Soil is the most complicated biomaterial on the earth, which is opaque and heterogeneous, and it also changes spatiotemporally across different seasons and spatial scale. It is thus challenging to study soil structure and root growth in it. However, they are important to improve nutrient and water use efficiency in developing sustainable agriculture. In made efforts in this project, presenting various experimental and theoretical methods to bridge this knowledge gap.

Chapter 3 focuses on soil-root interaction under different abiotic and biotic stresses, including root architecture and change in hydraulic properties of the rhizosphere. Maize was grown in pots packed with sandy loam, and it was then subjected to water and salinity stress in both isolation and combination. I also imposed a biotic stress by cutting one leaf when the crop grew to three-leaf stage. Analysing the images acquired using the X-ray tomography at resolution of 110 microns revealed that the abiotic stresses altered the root traits considerably. In particular, it was found that both water stress and salinity stress made the crown roots

grow more horizontally. While this apparently conflicts with the “cheap, deep and steep” principle when maize growing in the field suffers from water stress, in the pot experiment it is the topsoil where water and nutrients were rich due to the irrigation and fertilization. Thus, my results are still consistent with the principle “cheap, deep and steep” in that under abiotic stress, roots grow into areas that are rich in water and nutrients.

Chapter 4 is the continuation of Chapter 3, aimed to study the impact of water and salinity stress on hydraulic properties of the rhizosphere of the maize. Aggregates adhering to the roots under different treatments were harvested after pulling the roots from the pots, and I then scanned them using X-ray tomography at a resolution of 4um. The images were then segmented and their porosity and ability to conduct fluid (permeability) were calculated from pore-scale simulation using the lattice Boltzmann model. The permeability of each image was calculated from the simulated pore-scale velocity and pressure. I found that the abiotic stress, either working alone or in combination, substantially reduced the aggregate porosity and its ability to conduct water, especially when the crop was under both water and salinity stresses. As water and nutrients must flow into the rhizosphere before being taken up by crops, these findings have important implications for understanding the impact of abiotic stresses on root uptake of water and nutrients.

Chapter 5 is the continuation of Chapters 3 and 4, aimed to investigate how root uptake of water affects solute movement and its subsequent accumulation in soil, especially in the rhizosphere. Visualization of all aggregates acquired using the X-ray tomography found salt crusts in two images, indicating that salt was not uniformly distributed along the root, but

accumulated in specific locations. To understand the relationship between salt accumulation and pore geometry, I presented a method to simultaneously quantify the salt crusts and the size of the pores in which the salt precipitated. The results showed that the salt precipitation was a result of ion-filtering by the root when it took up the water, and that the salt precipitated in small pores more than in large pores.

Chapters 6 and 7 studied the impact of long-term cropping systems and land management changes on soil structure and its ability to transport water and soluble substrates. Soil samples were taken from the ley-arable experiment at Rothamsted in the UK, which were started by Lawes and Gilbert in 1843 onwards and are still in operation. The soil samples were scanned using X-ray tomography at resolutions of 40μm (core scale) and 1.5 μm (aggregate scale) respectively. In my thesis, I only investigate the structure of the aggregates and their ability to retain and conduct water and substrates.

Chapter 6 focused on the change in hydraulic properties, which are important for aggregates in the proximity of the roots as root water uptake drives water in these aggregates to flow towards the root. In this chapter, I investigated how the cropping systems and land management changes more than 70 years ago reshaped the soil structure. X-ray images of the aggregates taken from soil under perennial grass and winter wheat, as well as bare fallow were segmented into binary images, from which I analysed the porosity and calculated the ability of the aggregates to retain and conduct water respectively. My results show that the porosity and ability of the aggregates to retain and conduct water were affected substantially by the cropping systems and land management. In short, the perennial grass increased the

porosity and the ability of the aggregates to retain and conduct water under both saturated and unsaturated conditions, compared to the permanent arable land and bare-fallow soil. Although the porosity of the aggregates taken from the grassland and arable land differed, their pores are more geometrically similar compared to the aggregate taken from the bare fallow soil.

Chapter 7 focused on the ability of the aggregates to transport soluble substrates. This is relevant for aggregates far away from roots where the water is almost stagnant and soluble substrates in them move predominantly by molecular diffusion. This is important to understand the interaction between soil microbes and soil structure. For each aggregate, I calculated its effective molecular diffusion coefficient and linked it to soil carbon. The results showed that the increased carbon input to soil in the grassland and the arable land increased the porosity and ability of the aggregates to transport substrates. In particular, I found that the effective diffusion of the aggregates does not increase with soil carbon proportionally but asymptotically in that there is a limit for soil organic carbon to affect the aggregate structure and its ability to transport substrates. This has important implications for understanding the potential of soil to sequester carbon.

8.2. Problem and future work

Segmentation of X-ray images bears uncertainty and depends on practitioners. Apparently, there are no reliable methods to automatically segment X-ray images and in certain circumstances, the segmentation has to be done manually. For example, I tried but failed to map the roots automatically and thus had to do this manually, which was extremely

tedious given that there were 24 samples to analyse. Also, due to the limitation of beamtime, I was unable to scan enough samples, such as the samples for studying salt precipitation and the rhizosphere aggregates. Therefore, it is thus prudent not to extend the results to more general situations, such as maize growing in the field.

Notwithstanding this, the results of my project improved our understanding of how root-soil interactions coordinate root growth and alter the properties of the soil in the immediate proximity of the roots. As the studies were based on potted soil which limited the root growth and is not as complicated as the field soil, to what extent these results could be extrapolated to the field soil needs further examination. The impact of long-term experiments on soil structure was based on soil samples taken from the field, and how to apply these results to improve our understanding of other soil processes such as greenhouse emission and improving soil management also needs further research.

References

Abbe, E.C., Stein, O.L., 1954. THE GROWTH OF THE SHOOT APEX IN MAIZE: EMBRYOGENY. American Journal of Botany, 41(4): 285-293. DOI:10.1002/j.1537-2197.1954.tb14338.x

Affairs, D.o.E.a.S., 2017. WorldPopulation2017. Department of Economic and Social Affairs • Population Division, United Nations.

Ahmed, M.A. et al., 2016. Drying of mucilage causes water repellency in the rhizosphere of maize: measurements and modelling. Plant and Soil, 407(1): 161-171. DOI:10.1007/s11104-015-2749-1

Ahmed, M.A. et al., 2018. Root type matters: measurement of water uptake by seminal, crown, and lateral roots in maize. J Exp Bot, 69(5): 1199-1206. DOI:10.1093/jxb/erx439

Al-Raoush, R.I., Willson, C.S., 2005. Extraction of physically realistic pore network properties from three-dimensional synchrotron X-ray microtomography images of unconsolidated porous media systems. J. Hydrol., 300(1-4): 44-64. DOI:10.1016/j.jhydrol.2004.05.005

Alami, Y., Achouak, W., Marol, C., Heulin, T., 2000. Rhizosphere soil aggregation and plant growth promotion of sunflowers by an exopolysaccharide-producing Rhizobium sp. strain isolated from sunflower roots. Applied and environmental microbiology, 66(8): 3393-3398. DOI:10.1128/aem.66.8.3393-3398.2000

Alberti, M., 2008. Advances in Urban Ecology. Integrating Humans and Ecological Processes in Urban Ecosystems, 1-366 pp. DOI:10.1007/978-0-387-75510-6

Alharby, H.F., Colmer, T.D., Barrett-Lennard, E.G., 2014. Salt accumulation and depletion in the root-zone of the halophyte Atriplex nummularia Lindl.: influence of salinity, leaf area and plant water use. Plant and Soil, 382(1): 31-41. DOI:10.1007/s11104-014-2148-z

Alharby, H.F., Colmer, T.D., Barrett-Lennard, E.G., 2018. Salinization of the soil solution decreases the further accumulation of salt in the root zone of the halophyte Atriplex nummularia Lindl. growing above shallow saline groundwater. Plant Cell Environ, 41(1): 99-110. DOI:10.1111/pce.12958

Ananyeva, K., Wang, W., Smucker, A.J.M., Rivers, M.L., Kravchenko, A.N., 2013. Can intra-aggregate pore structures affect the aggregate's effectiveness in protecting carbon? Soil Biology and Biochemistry, 57: 868-875. DOI:https://doi.org/10.1016/j.soilbio.2012.10.019

Arai, M. et al., 2019. An improved method to identify osmium-stained organic matter within soil aggregate structure by electron microscopy and synchrotron X-ray micro-computed tomography. Soil and Tillage Research, 191: 275-281. DOI:https://doi.org/10.1016/j.still.2019.04.010

Aravena, G., Broitman, B., Stenseth, N.C., 2014. Twelve Years of Change in Coastal Upwelling along the Central-Northern Coast of Chile: Spatially Heterogeneous Responses to Climatic Variability. PLOS ONE, 9(2): e90276. DOI:10.1371/journal.pone.0090276

Atkinson, B.S., Sparkes, D.L., Mooney, S.J., 2009. Effect of seedbed cultivation and soil macrostructure on the establishment of winter wheat (Triticum aestivum). Soil and Tillage Research, 103(2): 291-301. DOI:10.1016/j.still.2008.10.027

Atkinson, J.A., Hawkesford, M.J., Whalley, W.R., Zhou, H., Mooney, S.J., 2020a. Soil strength influences wheat root interactions with soil macropores. Plant, Cell & Environment, 43(1): 235-245. DOI:10.1111/pce.13659

Atkinson, J.A., Hawkesford, M.J., Whalley, W.R., Zhou, H., Mooney, S.J., 2020b. Soil strength influences wheat root interactions with soil macropores. Plant Cell Environ., 43(1): 235-245. DOI:10.1111/pce.13659

Augustin, M., J., E, P., F, B., 1995. Litter decomposition and matter transport in beds of soil aggregates. 237–255.

Bacq-Labreuil, A. et al., 2018a. Effects of cropping systems upon the three-dimensional architecture of soil systems are modulated by texture. Geoderma, 332: 73-83. DOI:10.1016/j.geoderma.2018.07.002

Bacq-Labreuil, A. et al., 2018b. Effects of cropping systems upon the three-dimensional architecture of soil systems are modulated by texture. Geoderma, 332: 73-83. DOI:10.1016/j.geoderma.2018.07.002

Bacq-Labreuil, A., Crawford, J., Mooney, S.J., Neal, A.L., Ritz, K., 2020. Recovery of soil structure under long-term fallow in response to annual or perennial cropping requires at least 10 years after conversion. Enropean Journal of Soil Science, 9: 9. DOI:10.1038/s41598-019-43937-6

Bao, Y. et al., 2014. Plant roots use a patterning mechanism to position lateral root branches toward available water. Proceedings of the National Academy of Sciences, 111(25): 9319. DOI:10.1073/pnas.1400966111

Barber, S., 2014. Soil nutrient bioavailability :a mechanics approach.

Bargaz, A., Lyamlouli, K., Chtouki, M., Zeroual, Y., Dhiba, D., 2018. Soil Microbial Resources for Improving Fertilizers Efficiency in an Integrated Plant Nutrient Management System. Front. Microbiol., 9: 1606-1606. DOI:10.3389/fmicb.2018.01606

Barré, P. et al., 2010. Quantifying and isolating stable soil organic carbon using long-term bare fallow experiments. Biogeosciences, 7(11): 3839-3850. DOI:10.5194/bg-7-3839-2010

Baumert, V.L. et al., 2018. Root Exudates Induce Soil Macroaggregation Facilitated by Fungi in Subsoil. Frontiers in Environmental Science, 6(140). DOI:10.3389/fenvs.2018.00140

Baveye, P.C. et al., 2010. Observer-dependent variability of the thresholding step in the quantitative analysis of soil images and X-ray microtomography data. Geoderma, 157(1): 51-63. DOI:https://doi.org/10.1016/j.geoderma.2010.03.015

Baveye, P.C. et al., 2018. Emergent Properties of Microbial Activity in Heterogeneous Soil Microenvironments: Different Research Approaches Are Slowly Converging, Yet Major Challenges Remain. Front. Microbiol., 9: 48. DOI:10.3389/fmicb.2018.01929

Bazihizina, N., Barrett-Lennard, E.G., Colmer, T.D., 2012. Plant growth and physiology under heterogeneous salinity. Plant and Soil, 354(1): 1-19. DOI:10.1007/s11104-012-1193-8

Bechtold, M. et al., 2011. Near-surface solute redistribution during evaporation. Geophys. Res. Lett., 38, L17404. DOI:10.1029/2011GL048147

Benard, P. et al., 2019. Microhydrological Niches in Soils: How Mucilage and EPS Alter the Biophysical Properties of the Rhizosphere and Other Biological Hotspots. Vadose Zone Journal, 18(1): 180211. DOI:10.2136/vzj2018.12.0211

Bengough, A.G., 2012. Water Dynamics of the Root Zone: Rhizosphere Biophysics and Its Control on Soil Hydrology. Vadose Zone J., 11(2): 6. DOI:10.2136/vzj2011.0111

Bengough, A.G., McKenzie, B.M., Hallett, P.D., Valentine, T.A., 2011. Root elongation, water stress, and mechanical impedance: a review of limiting stresses and beneficial root tip traits. J Exp Bot, 62(1): 59-68. DOI:10.1093/jxb/erq350

Berezniak, A., Ben-Gal, A., Mishael, Y., Nachshon, U., 2017. Manipulation of Soil Texture to Remove Salts from a Drip-Irrigated Root Zone. Vadose Zone Journal, 17. DOI:10.2136/vzj2017.01.0019

Berger, A.L. et al., 2013. Ecological Impacts of Energy-Wood Harvests: Lessons from Whole-Tree Harvesting and Natural Disturbance. Journal of Forestry, 111(2): 139-153. DOI:10.5849/jof.12-020

Bergmann, J. et al., 2016. The interplay between soil structure, roots, and microbiota as a determinant of plant-soil feedback. Ecology and evolution, 6(21): 7633-7644. DOI:10.1002/ece3.2456

Bergstad, M., Or, D., Withers, P.J., Shokri, N., 2018. Evaporation Dynamics and NaCl Precipitation on Capillarity-Coupled Heterogeneous Porous Surfaces. Water Resources Research, 54(6): 3876-3885. DOI:10.1029/2018wr022614

Bergstad, M., Shokri, N., 2016. Evaporation of NaCl solution from porous media with mixed wettability. Geophysical Research Letters, 43(9): 4426-4432. DOI:10.1002/2016GL068665

Beven, K., Germann, P., 2013. Macropores and water flow in soils revisited. Water Resources Research, 49(6): 3071-3092. DOI:10.1002/wrcr.20156

Bill A. Stout, R.L., Curtis H. Monger, 2016. Carbon capture and sequestration: The roles of agriculture and soils. International Journal of Agricultural and Biological DOI:10.3965/j.ijabe.20160901.2280

Blunt, M.J. et al., 2013. Pore-scale imaging and modelling. Adv. Water Resour., 51: 197-216. DOI:10.1016/j.advwatres.2012.03.003

Bowers, S.A., Hanks, R.J., 1965. REFLECTION OF RADIANT ENERGY FROM SOILS. Soil Science, 100(2).

Bucksch, A. et al., 2014. Image-Based High-Throughput Field Phenotyping of Crop Roots. Plant Physiology, 166(2): 470. DOI:10.1104/pp.114.243519
Caldwell, T.G., Young, M.H., McDonald, E.V., Zhu, J., 2012. Soil heterogeneity in Mojave Desert shrublands: Biotic and abiotic processes. Water Resources Research, 48(9). DOI:10.1029/2012WR011963
Cantone, M., Hoeschen, C., 2011. Radiation Physics for Nuclear Medicine. DOI:10.1007/978-3-642-11327-7
Caravaca, F., Figueroa, D., Barea, J.M., Azcón-Aguilar, C., Roldán, A., 2004. Effect of Mycorrhizal Inoculation on Nutrient Acquisition, Gas Exchange, and Nitrate Reductase Activity of Two Mediterranean-Autochthonous Shrub Species Under Drought Stress. Journal of Plant Nutrition, 27(1): 57-74. DOI:10.1081/PLN-120027547
Carey, J.C. et al., 2016. Temperature response of soil respiration largely unaltered with experimental warming. Proc Natl Acad Sci U S A, 113(48): 13797-13802. DOI:10.1073/pnas.1605365113
Carminati, A. et al., 2010. Dynamics of soil water content in the rhizosphere. Plant and Soil, 332(1): 163-176. DOI:10.1007/s11104-010-0283-8
Castro, H.F., Classen, A.T., Austin, E.E., Norby, R.J., Schadt, C.W., 2010. Soil microbial community responses to multiple experimental climate change drivers. Appl Environ Microbiol, 76(4): 999-1007. DOI:10.1128/AEM.02874-09
Chang, C.-W., Laird, D.A., Mausbach, M.J., Hurburgh, C.R., 2001. Near-Infrared Reflectance Spectroscopy–Principal Components Regression Analyses of Soil Properties. Soil Science Society of America Journal, 65(2): 480-490. DOI:10.2136/sssaj2001.652480x
Chen, S., Doolen, G.D., 1998. Lattice Boltzmann method for fluid flows. Annual Review of Fluid Mechanics, 30: 329-364. DOI:10.1146/annurev.fluid.30.1.329
Comas, L.H., Becker, S.R., Cruz, V.M.V., Byrne, P.F., Dierig, D.A., 2013. Root traits contributing to plant productivity under drought. Frontiers in plant science, 4: 442-442. DOI:10.3389/fpls.2013.00442
Condron, L.M., Stark, C., O'Callaghan, M., Clinton, P., Huang, Z., 2010. The Role of Microbial Communities in the Formation and Decomposition of Soil Organic Matter, pp. 81-118. DOI:10.1007/978-90-481-9479-7_4
Crawford, J.W. et al., 2012. Microbial diversity affects self-organization of the soil-microbe system with consequences for function. J R Soc Interface, 9(71): 1302-1310. DOI:10.1098/rsif.2011.0679
Crawford, J.W., Harris, J.A., Ritz, K., Young, I.M., 2005. Towards an evolutionary ecology of life in soil. Trends in ecology & evolution, 20(2): 81-7. DOI:10.1016/j.tree.2004.11.014
Cullen, J.J., Boyd, P.W., 2008. Predicting and verifying the intended and unintended consequences of large-scale ocean iron fertilization. Marine Ecology Progress Series, 364: 295-301.

Czarnes, S., Hallett, P., Bengough, A., Young, I., 2000. Root- and microbial-derived mucilages affect soil structure and water transport. European Journal of Soil Science, 51: 435-443. DOI:10.1046/j.1365-2389.2000.00327.x

d'Humières, D., Ginzburg, I., Krafczyk, M., Lallemand, P., Luo, L.S., 2002. Multiple-relaxation-time lattice Boltzmann models in three dimensions. Philos. Trans. R. Soc. Lond. Ser. A-Math. Phys. Eng. Sci., 360(1792): 437-451. DOI:10.1098/rsta.2001.0955

Dalal, R., Henry, R., 1986. Simultaneous Determination of Moisture, Organic Carbon, and Total Nitrogen by Near Infrared Reflectance Spectrophotometry1. Soil Science Society of America Journal - SSSAJ, 50. DOI:10.2136/sssaj1986.03615995005000010023x

Daly, K.R. et al., 2015. Assessing the influence of the rhizosphere on soil hydraulic properties using X-ray computed tomography and numerical modelling. J Exp Bot, 66(8): 2305-14. DOI:10.1093/jxb/eru509

Darrah, P.R., 1991a. Models of the rhizosphere. Plant and Soil, 133(2): 187-199. DOI:10.1007/BF00009191

Darrah, P.R., 1991b. Models of the rhizosphere: II. A quasi three-dimensional simulation of the microbial population dynamics around a growing root releasing soluble exudates. Plant and Soil, 138(2): 147-158.

de Moraes, M.T. et al., 2019. Mechanical and Hydric Stress Effects on Maize Root System Development at Different Soil Compaction Levels. Frontiers in Plant Science, 10(1358). DOI:10.3389/fpls.2019.01358

Deng, X., Li, Z., 2016. Economics of Land Degradation in China. In: Nkonya, E., Mirzabaev, A., von Braun, J. (Eds.), Economics of Land Degradation and Improvement – A Global Assessment for Sustainable Development. Springer International Publishing, Cham, pp. 385-399. DOI:10.1007/978-3-319-19168-3_13

Dexter, A.R., 1987. Compression of soil around roots Plant Soil, 97(3): 401-406. DOI:10.1007/bf02383230

Dignac, M.-F. et al., 2017. Increasing soil carbon storage: mechanisms, effects of agricultural practices and proxies. A review. Agronomy for Sustainable Development, 37(2): 14. DOI:10.1007/s13593-017-0421-2

Dunbabin, V.M. et al., 2013. Modelling root–soil interactions using three–dimensional models of root growth, architecture and function. Plant and Soil, 372(1-2): 93-124. DOI:10.1007/s11104-013-1769-y

Dungait, J.A.J., Hopkins, D.W., Gregory, A.S., Whitmore, A.P., 2012. Soil organic matter turnover is governed by accessibility not recalcitrance. Global Change Biology, 18(6): 1781-1796. DOI:10.1111/j.1365-2486.2012.02665.x

Easton, Z.M., Bock, E.M., 2016. Soil and Soil Water Relationships.

Fahad, S. et al., 2017. Crop Production under Drought and Heat Stress: Plant Responses and Management Options. Frontiers in plant science, 8: 1147-1147. DOI:10.3389/fpls.2017.01147

Feldman, L., 1994. The Maize Root. In: Freeling, M., Walbot, V. (Eds.), The Maize Handbook. Springer New York, New York, NY, pp. 29-37. DOI:10.1007/978-1-4612-2694-9_4

Franco, J., Bañón, S., Vicente, M., Miralles, J., Martínez-Sánchez, J.J., 2011. Root development in horticultural plants grown under abiotic stress conditions - a review. Journal of Horticultural Science and Biotechnology, 86: 543-556. DOI:10.1080/14620316.2011.11512802

Fu, J.L., Thomas, H.R., Li, C.F., 2021. Tortuosity of porous media: Image analysis and physical simulation. Earth-Sci. Rev., 212: 30. DOI:10.1016/j.earscirev.2020.103439

Galkovskyi, T. et al., 2012. GiA Roots: software for the high throughput analysis of plant root system architecture. BMC Plant Biol., 12: 12. DOI:10.1186/1471-2229-12-116

Garcia-Pausas, J. et al., 2007. Soil organic carbon storage in mountain grasslands of the Pyrenees: effects of climate and topography. Biogeochemistry, 82(3): 279-289. DOI:10.1007/s10533-007-9071-9

Ghanbarian, B., Hunt, A.G., Ewing, R.P., Sahimi, M., 2013. Tortuosity in Porous Media: A Critical Review. Soil Sci. Soc. Am. J., 77(5): 1461-1477. DOI:10.2136/sssaj2012.0435

Godwill, E., Ferdinand, P., Nwalo, N., Unachukwu, M., 2019. Mechanism and Health Effects of Heavy Metal Toxicity in Humans, pp. 1-23. DOI:10.5772/intechopen.82511

Gong, F., Wu, X., Zhang, H., Chen, Y., Wang, W., 2015. Making better maize plants for sustainable grain production in a changing climate. Front Plant Sci, 6: 835. DOI:10.3389/fpls.2015.00835

Gonzalez, R.C., 1987. Digital_Image_Processing.

Goulding, K., 2000. Nitrate leaching from arable and horticultural land. Soil Use and Management, 16(s1): 145-151. DOI:10.1111/j.1475-2743.2000.tb00218.x

Gray, S.B., Brady, S.M., 2016. Plant developmental responses to climate change. Developmental Biology, 419(1): 64-77. DOI:https://doi.org/10.1016/j.ydbio.2016.07.023

Gregory, A.S. et al., 2016. Long-term management changes topsoil and subsoil organic carbon and nitrogen dynamics in a temperate agricultural system. Eur. J. Soil Sci., 67(4): 421-430. DOI:10.1111/ejss.12359

Gregory, P.J., 2006. Roots, rhizosphere and soil: the route to a better understanding of soil science? Eur. J. Soil Sci., 57(1): 2-12. DOI:10.1111/j.1365-2389.2005.00778.x

Gregory, P.J. et al., 2003. Non-invasive imaging of roots with high resolution X-ray micro-tomography. Plant and Soil, 255(1): 351-359. DOI:10.1023/A:1026179919689

Grevers, M.C.J., Jong, E.D., St. Arnaud, R.J., 1989. THE CHARACTERIZATION OF SOIL MACROPOROSITY WITH CT SCANNING. Canadian Journal of Soil Science, 69(3): 629-637. DOI:10.4141/cjss89-062

Guo, Y. et al., 2020. Tillage-induced effects on SOC through changes in aggregate stability and soil pore structure. Sci Total Environ, 703: 134617. DOI:10.1016/j.scitotenv.2019.134617

Haber-Pohlmeier, S. et al., 2019. Combination of Magnetic Resonance Imaging and Neutron Computed Tomography for Three-Dimensional Rhizosphere Imaging. Vadose Zone Journal, 18(1): 180166. DOI:10.2136/vzj2018.09.0166

Haling, R.E. et al., 2013a. Root hairs improve root penetration, root–soil contact, and phosphorus acquisition in soils of different strength. Journal of Experimental Botany, 64(12): 3711-3721. DOI:10.1093/jxb/ert200

Haling, R.E., Tighe, M.K., Flavel, R.J., Young, I.M., 2013b. Application of X-ray computed tomography to quantify fresh root decomposition in situ. Plant and Soil, 372(1): 619-627. DOI:10.1007/s11104-013-1777-y

Hall, R.O., 2016. Chapter 4 - Metabolism of Streams and Rivers: Estimation, Controls, and Application. In: Jones, J.B., Stanley, E.H. (Eds.), Stream Ecosystems in a Changing Environment. Academic Press, Boston, pp. 151-180. DOI:https://doi.org/10.1016/B978-0-12-405890-3.00004-X

Hallett, P.D., Gordon, D.C., Bengough, A.G., 2003. Plant influence on rhizosphere hydraulic properties: direct measurements using a miniaturized infiltrometer. New Phytol., 157(3): 597-603. DOI:10.1046/j.1469-8137.2003.00690.x

Hamza, M.A., Aylmore, L.A.G., 1992. Soil solute concentration and water uptake by single lupin and radish plant roots. Plant and Soil, 145(2): 187-196. DOI:10.1007/BF00010347

Hansen, J., Sato, M., 2016. Regional climate change and national responsibilities. Environmental Research Letters, 11(3): 034009. DOI:10.1088/1748-9326/11/3/034009

Hartmann, A., Rothballer, M., Schmid, M., 2008. Lorenz Hiltner, a pioneer in rhizosphere microbial ecology and soil bacteriology research. Plant and Soil, 312(1): 7-14. DOI:10.1007/s11104-007-9514-z

Heeraman, D.A., Hopmans, J.W., Clausnitzer, V., 1997. Three dimensional imaging of plant roots in situ with X-ray Computed Tomography. Plant and Soil, 189(2): 167-179. DOI:10.1023/B:PLSO.0000009694.64377.6f

Helliwell, J.R. et al., 2013. Applications of X-ray computed tomography for examining biophysical interactions and structural development in soil systems: a review. Eur. J. Soil Sci., 64(3): 279-297. DOI:10.1111/ejss.12028

Helliwell, J.R. et al., 2017. The emergent rhizosphere: imaging the development of the porous architecture at the root-soil interface. Scientific reports, 7(1): 14875-14875. DOI:10.1038/s41598-017-14904-w

Helliwell, J.R., Sturrock, C.J., Miller, A.J., Whalley, W.R., Mooney, S.J., 2019. The role of plant species and soil condition in the structural development of the rhizosphere. Plant Cell Environ, 42(6): 1974-1986. DOI:10.1111/pce.13529

Hiltner, L., 1904. Über neuere Erfahrungen und Probleme auf dem Gebiete der Bodenbakteriologie unter besonderer Berücksichtigung der Gründüngung und Brache.

Hinsinger, P., Bengough, A.G., Vetterlein, D., Young, I.M., 2009. Rhizosphere: biophysics, biogeochemistry and ecological relevance. Plant and Soil, 321(1): 117-152. DOI:10.1007/s11104-008-9885-9

Hinsinger, P., Plassard, C., Tang, C., Jaillard, B., 2003. Origins of root-mediated pH changes in the rhizosphere and their responses to environmental constraints: A review. Plant and Soil, 248: 43-59. DOI:10.1023/A:1022371130939

Hochholdinger, F., Tuberosa, R., 2009. Hochholdinger F, Tuberosa T. Genetic and genomic dissection of maize root development and architecture. Curr Opin Plant Biol, 2009. Current opinion in plant biology, 12: 172-7. DOI:10.1016/j.pbi.2008.12.002

Hochholdinger, F., Woll, K., Sauer, M., Dembinsky, D., 2004. Genetic Dissection of Root Formation in Maize (Zea mays) Reveals Root-type Specific Developmental Programmes. Annals of botany, 93: 359-68. DOI:10.1093/aob/mch056

Hodge, A., 2004. The plastic plant: root responses to heterogeneous supplies of nutrients. New Phytologist, 162(1): 9-24. DOI:10.1111/j.1469-8137.2004.01015.x

Huang, Y., Yang, Z., Ren, W., Liu, G., Zhang, C., 2015. 3D meso-scale fracture modelling and validation of concrete based on in-situ X-ray Computed Tomography images using damage plasticity model. International Journal of Solids and Structures, 67-68: 340-352. DOI:https://doi.org/10.1016/j.ijsolstr.2015.05.002

Hutchings, M., John, E., 2003. Distribution of Roots in Soil, and Root Foraging Activity, pp. 33-60. DOI:10.1007/978-3-662-09784-7_2

Jacoby, R., Peukert, M., Succurro, A., Koprivova, A., Kopriva, S., 2017. The Role of Soil Microorganisms in Plant Mineral Nutrition-Current Knowledge and Future Directions. Frontiers in plant science, 8: 1617-1617. DOI:10.3389/fpls.2017.01617

Jassogne, L., Hettiarachchi, G., Chittleborough, D., McNeill, A., 2009. Distribution and Speciation of Nutrient Elements around Micropores. Soil Science Society of America Journal, 73(4): 1319-1326. DOI:10.2136/sssaj2008.0174

Jastrow, J.D., Miller, R.M., Boutton, T.W., 1996. Carbon Dynamics of Aggregate-Associated Organic Matter Estimated by Carbon-13 Natural Abundance. Soil Science Society of America Journal, 60(3): 801-807. DOI:10.2136/sssaj1996.03615995006000030017x

Johnston, A.E., Poulton, P.R., 2018. The importance of long-term experiments in agriculture: their management to ensure continued crop production and soil fertility; the Rothamsted experience. European Journal of Soil Science, 69(1): 113-125. DOI:10.1111/ejss.12521

Johnston, A.E., Poulton, P.R., Coleman, K., 2009. Soil organic matter: its importance in sustainable agriculture and carbon dioxide fluxes. Elsevier Inc., San Diego, pp. 1-57.

Juarez, S. et al., 2013. Effects of different soil structures on the decomposition of native and added organic carbon. European Journal of Soil Biology, 58: 81-90. DOI:https://doi.org/10.1016/j.ejsobi.2013.06.005

Kabir, Z., Koide, R.T., 2000. The effect of dandelion or a cover crop on mycorrhiza inoculum potential, soil aggregation and yield of maize. Agriculture, Ecosystems & Environment, 78(2): 167-174. DOI:https://doi.org/10.1016/S0167-8809(99)00121-8

Kaci, Y., Heyraud, A., Barakat, M., Heulin, T., 2005. Isolation and identification of an EPS-producing Rhizobium strain from arid soil (Algeria): characterization of its EPS and the effect of inoculation on wheat rhizosphere soil structure. Research in microbiology, 156(4): 522-31. DOI:10.1016/j.resmic.2005.01.012

Kallenbach, C.M., Frey, S.D., Grandy, A.S., 2016. Direct evidence for microbial-derived soil organic matter formation and its ecophysiological controls. Nat Commun, 7: 13630. DOI:10.1038/ncomms13630

Keller, A.A., 1997. High resolution cat imaging of fractures in consolidated materials. International Journal of Rock Mechanics and Mining Sciences, 34(3): 155.e1-155.e16. DOI:https://doi.org/10.1016/S1365-1609(97)00181-0

Khan, A.L. et al., 2020. Rhizosphere Microbiome of Arid Land Medicinal Plants and Extra Cellular Enzymes Contribute to Their Abundance. Microorganisms, 8(2): 213. DOI:10.3390/microorganisms8020213

Koebernick, N. et al., 2017. High-resolution synchrotron imaging shows that root hairs influence rhizosphere soil structure formation. New Phytol., 216(1): 124-135. DOI:10.1111/nph.14705

Koevoets, I.T., Venema, J.H., Elzenga, J.T.M., Testerink, C., 2016. Roots Withstanding their Environment: Exploiting Root System Architecture Responses to Abiotic Stress to Improve Crop Tolerance. Frontiers in plant science, 7: 1335-1335. DOI:10.3389/fpls.2016.01335

Kong, X., Luo, Z., Dong, H., Li, W., Chen, Y., 2017. Non-uniform salinity in the root zone alleviates salt damage by increasing sodium, water and nutrient transport genes expression in cotton. Scientific Reports, 7(1): 2879. DOI:10.1038/s41598-017-03302-x

Kravchenko, A.N. et al., 2019. Microbial spatial footprint as a driver of soil carbon stabilization. Nat. Commun., 10: 10. DOI:10.1038/s41467-019-11057-4

Kravchenko, A.N., Negassa, W.C., Guber, A.K., Rivers, M.L., 2015. Protection of soil carbon within macro-aggregates depends on intra-aggregate pore characteristics. Scientific reports, 5: 16261-16261. DOI:10.1038/srep16261

Krishna, K.R., 2013. Agroecosystems: Soils, climate, crops, nutrient dynamics, and productivity, 1-517 pp. DOI:10.1201/b16300

Krishnan, P., Alexander, J.D., Butler, B.J., Hummel, J.W., 1980. Reflectance Technique for Predicting Soil Organic Matter. Soil Science Society of America Journal, 44(6): 1282-1285. DOI:10.2136/sssaj1980.03615995004400060030x

Krounbi, L., Lazarovitch, N., 2014. Soil Hydraulic Properties Affecting Root Water Uptake, pp. 748-754. DOI:10.1007/978-90-481-3585-1_149

Kumar, R., Rawat, K.S., Singh, J., Singh, A., Rai, A., 2013. Soil aggregation dynamics and carbon sequestration. Journal of Applied and Natural Science, 5(1): 250-267. DOI:10.31018/jans.v5i1.314

Kuzyakov, Y., Blagodatskaya, E., 2015. Microbial hotspots and hot moments in soil: Concept & review. Soil Biology and Biochemistry, 83: 184-199. DOI:10.1016/j.soilbio.2015.01.025

Lal, R., 1996. Deforestation and land-use effects on soil degradation and rehabilitation in western Nigeria. II. Soil chemical properties. Land Degradation & Development, 7(2): 87-98. DOI:10.1002/(SICI)1099-145X(199606)7:2<87::AID-LDR219>3.0.CO;2-X

Lambers, H., Shane, M.W., Cramer, M.D., Pearse, S.J., Veneklaas, E.J., 2006. Root structure and functioning for efficient acquisition of phosphorus: Matching morphological and physiological traits. Annals of botany, 98(4): 693-713. DOI:10.1093/aob/mcl114

Li, L., Peters, C.A., Celia, M.A., 2006. Upscaling geochemical reaction rates using pore-scale network modeling. Adv. Water Resour., 29(9): 1351-1370. DOI:10.1016/j.advwatres.2005.10.011

Li, Y. et al., 2014. An analysis of China's grain production: looking back and looking forward. Food and Energy Security, 3(1): 19-32. DOI:10.1002/fes3.41

Li, Z., Zhang, X., Wang, D., Liu, Y., 2018a. Direct methods to calculate the mass exchange between solutes inside and outside aggregates in macroscopic model for solute transport in aggregated soil. Geoderma, 320: 126-135. DOI:https://doi.org/10.1016/j.geoderma.2018.01.021

Li, Z.Y., Wang, D., Zhang, X.X., Crawford, J.W., 2018b. Water flow across the interface of contrasting materials: Pressure discontinuity and its implications. J. Hydrol., 566: 435-440. DOI:10.1016/j.jhydrol.2018.09.029

Li, Z.Y., Zhang, X.X., Wang, D., Liu, Y., 2018c. Direct methods to calculate the mass exchange between solutes inside and outside aggregates in macroscopic model for solute transport in aggregated soil. Geoderma, 320: 126-135. DOI:10.1016/j.geoderma.2018.01.021

Liang, A. et al., 2019. Investigations of relationships among aggregate pore structure, microbial biomass, and soil organic carbon in a Mollisol using combined non-destructive measurements and phospholipid fatty acid analysis. Soil and Tillage Research, 185: 94-101. DOI:10.1016/j.still.2018.09.003

Lipson, D.A., Wilson, R.F., Oechel, W.C., 2005. Effects of Elevated Atmospheric CO₂ on Soil Microbial Biomass, Activity, and Diversity in a Chaparral Ecosystem. Applied and Environmental Microbiology, 71(12): 8573. DOI:10.1128/AEM.71.12.8573-8580.2005

Liu, J.e., Wang, Z., Li, Y., 2017. Efficacy of Natural Polymer Derivatives on Soil Physical Properties and Erosion on an Experimental Loess Hillslope. Int J Environ Res Public Health, 15(1): 9. DOI:10.3390/ijerph15010009

Liu, W., Liu, G., Zhang, Q., 2011. Influence of Vegetation Characteristics on Soil Denitrification in Shoreline Wetlands of the Danjiangkou Reservoir in China. CLEAN - Soil, Air, Water, 39(2): 109-115. DOI:10.1002/clen.200900212

López-Garrido, R., Madejón, E., Murillo, J.M., Moreno, F., 2011. Short and long-term distribution with depth of soil organic carbon and nutrients under traditional and conservation tillage in a Mediterranean environment (southwest Spain). Soil Use and Management, 27(2): 177-185. DOI:10.1111/j.1475-2743.2011.00329.x

Luo, Z., Wang, E., Sun, O.J., 2010. Can no-tillage stimulate carbon sequestration in agricultural soils? A meta-analysis of paired experiments. Agriculture, Ecosystems & Environment, 139(1): 224-231. DOI:https://doi.org/10.1016/j.agee.2010.08.006

Lützow, M.v. et al., 2006. Stabilization of organic matter in temperate soils: mechanisms and their relevance under different soil conditions – a review. European Journal of Soil Science, 57(4): 426-445. DOI:10.1111/j.1365-2389.2006.00809.x

Lynch, J.P., 2013. Steep, cheap and deep: an ideotype to optimize water and N acquisition by maize root systems. Ann Bot, 112(2): 347-57. DOI:10.1093/aob/mcs293

Mairhofer, S., Sturrock, C.J., Bennett, M.J., Mooney, S.J., Pridmore, T.P., 2015. Extracting multiple interacting root systems using X-ray microcomputed tomography. Plant J, 84(5): 1034-43. DOI:10.1111/tpj.13047

Masciandaro, G., Macci, C., Peruzzi, E., Ceccanti, B., Doni, S., 2013. Organic matter–microorganism–plant in soil bioremediation: a synergic approach. Reviews in Environmental Science and Bio/Technology, 12(4): 399-419. DOI:10.1007/s11157-013-9313-3

Mawodza, T., Burca, G., Casson, S., Menon, M., 2020. Wheat root system architecture and soil moisture distribution in an aggregated soil using neutron computed tomography. Geoderma, 359. DOI:10.1016/j.geoderma.2019.113988

McLean, J.E., Bledsoe, B.E., 1992. Behavior of metals in soils, United States.

Melton, E.D., Swanner, E.D., Behrens, S., Schmidt, C., Kappler, A., 2014. The interplay of microbially mediated and abiotic reactions in the biogeochemical Fe cycle. Nature Reviews Microbiology, 12(12): 797-808. DOI:10.1038/nrmicro3347

Mmolawa, K., Or, D., 2000. Root zone solute dynamics under drip irrigation: A review. Plant and Soil, 222(1): 163-190. DOI:10.1023/A:1004756832038

Mooney, S.J., 2002. Three-dimensional visualization and quantification of soil macroporosity and water flow patterns using computed tomography. Soil Use and Management, 18(2): 142-151. DOI:10.1111/j.1475-2743.2002.tb00232.x

Mooney, S.J., Morris, C., Berry, P.M., 2006. VISUALIZATION AND QUANTIFICATION OF THE EFFECTS OF CEREAL ROOT LODGING ON THREE-DIMENSIONAL SOIL

MACROSTRUCTURE USING X-RAY COMPUTED TOMOGRAPHY. Soil Science, 171(9).
Mooney, S.J., Pridmore, T.P., Helliwell, J., Bennett, M.J., 2011. Developing X-ray Computed Tomography to non-invasively image 3-D root systems architecture in soil. Plant and Soil, 352(1-2): 1-22. DOI:10.1007/s11104-011-1039-9
Mooney, S.J., Pridmore, T.P., Helliwell, J., Bennett, M.J., 2012. Developing X-ray Computed Tomography to non-invasively image 3-D root systems architecture in soil. Plant Soil, 352(1-2): 1-22. DOI:10.1007/s11104-011-1039-9
Moradi, A.B. et al., 2011. Three-dimensional visualization and quantification of water content in the rhizosphere. New Phytologist, 192(3): 653-663. DOI:10.1111/j.1469-8137.2011.03826.x
Morán, X.A.G. et al., 2017. Temperature regulation of marine heterotrophic prokaryotes increases latitudinally as a breach between bottom-up and top-down controls. Global Change Biology, 23(9): 3956-3964. DOI:10.1111/gcb.13730
Morris, E.C. et al., 2017. Shaping 3D Root System Architecture. Current Biology, 27(17): R919-R930. DOI:https://doi.org/10.1016/j.cub.2017.06.043
Naveed, M. et al., 2013. Revealing Soil Structure and Functional Macroporosity along a Clay Gradient Using X-ray Computed Tomography. Soil Science Society of America Journal, 77(2): 403-411. DOI:10.2136/sssaj2012.0134
Nciizah, A., Wakindiki, I., 2014. Physical indicators of soil erosion, aggregate stability and erodibility. Archives of Agronomy and Soil Science, 61: 1-16. DOI:10.1080/03650340.2014.956660
Neuffer, M.G., 1994. Growing Maize for Genetic Studies. In: Freeling, M., Walbot, V. (Eds.), The Maize Handbook. Springer New York, New York, NY, pp. 197-209. DOI:10.1007/978-1-4612-2694-9_21
Nicholson, A.M. et al., 2018. Fixation and Spread of Somatic Mutations in Adult Human Colonic Epithelium. Cell stem cell, 22(6): 909-918.e8. DOI:10.1016/j.stem.2018.04.020
Nunan, N., Ritz, K., Rivers, M., Feeney, D.S., Young, I.M., 2006. Investigating microbial micro-habitat structure using X-ray computed tomography. Geoderma, 133(3-4): 398-407. DOI:10.1016/j.geoderma.2005.08.004
Orchard, V.A., Cook, F.J., 1983. Relationship between soil respiration and soil moisture. Soil Biology and Biochemistry, 15(4): 447-453. DOI:https://doi.org/10.1016/0038-0717(83)90010-X
Ostadi, H. et al., 2010. 3D reconstruction of a gas diffusion layer and a microporous layer. Journal of Membrane Science, 351(1-2): 69-74. DOI:10.1016/j.memsci.2010.01.031
Pandey, B.K. et al., 2021. Plant roots sense soil compaction through restricted ethylene diffusion. Science, 371(6526): 276-280. DOI:10.1126/science.abf3013
Papadopoulos, A., Bird, N.R.A., Whitmore, A.P., Mooney, S.J., 2009. Investigating the effects of organic and conventional management on soil aggregate stability

using X-ray computed tomography. European Journal of Soil Science, 60(3): 360-368. DOI:10.1111/j.1365-2389.2009.01126.x
Peleg, Z., Blumwald, E., 2011. Hormone balance and abiotic stress tolerance in crop plants. Current Opinion in Plant Biology, 14(3): 290-295. DOI:https://doi.org/10.1016/j.pbi.2011.02.001
Perret, J., Al-Belushi, M.E., Deadman, M., 2007. Non-destructive visualization and quantification of roots using computed tomography. Soil Biology and Biochemistry, 39: 391-399. DOI:10.1016/j.soilbio.2006.07.018
Peth, S. et al., 2014. Localization of soil organic matter in soil aggregates using synchrotron-based X-ray microtomography. Soil Biology and Biochemistry, 78: 189-194. DOI:https://doi.org/10.1016/j.soilbio.2014.07.024
Petrovic, A.M., Siebert, J.E., Rieke, P.E., 1982. Soil Bulk Density Analysis in Three Dimensions by Computed Tomographic Scanning. Soil Science Society of America Journal, 46(3): 445-450. DOI:10.2136/sssaj1982.03615995004600030001x
Peyton, R.L., Haeffner, B.A., Anderson, S.H., Gantzer, C.J., 1992. Applying X-ray CT to measure macropore diameters in undisturbed soil cores. Geoderma, 53(3): 329-340. DOI:https://doi.org/10.1016/0016-7061(92)90062-C
Poulton, P., Johnston, J., Macdonald, A., White, R., Powlson, D., 2018. Major limitations to achieving "4 per 1000" increases in soil organic carbon stock in temperate regions: Evidence from long-term experiments at Rothamsted Research, United Kingdom. Glob Chang Biol, 24(6): 2563-2584. DOI:10.1111/gcb.14066
Pound, M.P. et al., 2013. RootNav: Navigating Images of Complex Root Architectures. Plant Physiol., 162(4): 1802-1814. DOI:10.1104/pp.113.221531
Qian, Y.H., Dhumieres, D., Lallemand, P., 1992. Lattice BGK models for Navier-Stokes equation. Europhysics Letters, 17(6BIS): 479-484. DOI:10.1209/0295-5075/17/6/001
Quin, P.R. et al., 2014. Oil mallee biochar improves soil structural properties-A study with x-ray micro-CT. Agric. Ecosyst. Environ., 191: 142-149. DOI:10.1016/j.agee.2014.03.022
Rabbi, S.M.F. et al., 2018. Plant roots redesign the rhizosphere to alter the three-dimensional physical architecture and water dynamics. New Phytologist, 219(2): 542-550. DOI:10.1111/nph.15213
Rao, I.M., Miles, J.W., Beebe, S.E., Horst, W.J., 2016. Root adaptations to soils with low fertility and aluminium toxicity. Annals of Botany, 118(4): 593-605. DOI:10.1093/aob/mcw073
Rasmussen, C. et al., 2018. Beyond clay: towards an improved set of variables for predicting soil organic matter content. Biogeochemistry, 137(3): 297-306. DOI:10.1007/s10533-018-0424-3
Read, D.B. et al., 2003. Plant roots release phospholipid surfactants that modify the physical and chemical properties of soil. New Phytol., 157(2): 315-326. DOI:10.1046/j.1469-8137.2003.00665.x

Ren, W., Yang, Z., Sharma, R., Zhang, C., Withers, P.J., 2015. Two-dimensional X-ray CT image based meso-scale fracture modelling of concrete. Engineering Fracture Mechanics, 133: 24-39. DOI:https://doi.org/10.1016/j.engfracmech.2014.10.016

Rogasik, H. et al., 1999. Discrimination of soil phases by dual energy x-ray tomography. Soil Sci. Soc. Am. J., 63(4): 741-751.

Rogasik, H., Onasch, I., Brunotte, J., Jegou, D., Wendroth, O., 2003. Assessment of Soil Structure Using X-ray Computed Tomography. Geological Society, London, Special Publications, 215: 151-165. DOI:10.1144/GSL.SP.2003.215.01.14

Rousseva, S. et al., 2017. Chapter Two - Soil Water Characteristics of European SoilTrEC Critical Zone Observatories. In: Banwart, S.A., Sparks, D.L. (Eds.), Advances in Agronomy. Academic Press, pp. 29-72. DOI:https://doi.org/10.1016/bs.agron.2016.10.004

Ruiz, S.A., Or, D., 2018. Biomechanical limits to soil penetration by earthworms: direct measurements of hydroskeletal pressures and peristaltic motions. J R Soc Interface, 15(144): 20180127. DOI:10.1098/rsif.2018.0127

Saljnikov, E., Cakmak, D., Rahimgalieva, S., 2013. Soil Organic Matter Stability as Affected by Land Management in Steppe Ecosystems, pp. 269-310. DOI:10.5772/53557

Schimel, J., Schaeffer, S., 2012. Microbial control over carbon cycling in soil. Front. Microbiol., 3(348). DOI:10.3389/fmicb.2012.00348

Schmidt, M.W.I. et al., 2011. Persistence of soil organic matter as an ecosystem property. Nature, 478(7367): 49-56. DOI:10.1038/nature10386

Schoonover, J.E., Crim, J.F., 2015. An Introduction to Soil Concepts and the Role of Soils in Watershed Management. Journal of Contemporary Water Research & Education, 154(1): 21-47. DOI:10.1111/j.1936-704X.2015.03186.x

Sessitsch, A., Weilharter, A., Gerzabek, M.H., Kirchmann, H., Kandeler, E., 2001. Microbial population structures in soil particle size fractions of a long-term fertilizer field experiment. Applied and environmental microbiology, 67(9): 4215-4224. DOI:10.1128/aem.67.9.4215-4224.2001

Sexstone, A.J., Revsbech, N.P., Parkin, T.B., Tiedje, J.M., 1985. Direct Measurement of Oxygen Profiles and Denitrification Rates in Soil Aggregates. Soil Science Society of America Journal, 49(3): 645-651. DOI:10.2136/sssaj1985.03615995004900030024x

Six, J., Bossuyt, H., Degryze, S., Denef, K., 2004. A history of research on the link between (micro)aggregates, soil biota, and soil organic matter dynamics. Soil Tillage Res., 79(1): 7-31. DOI:10.1016/j.still.2004.03.008

Six, J., Elliott, E.T., Paustian, K., 1999. Aggregate and Soil Organic Matter Dynamics under Conventional and No-Tillage Systems. Soil Science Society of America Journal, 63(5): 1350-1358. DOI:10.2136/sssaj1999.6351350x

Six, J., Elliott, E.T., Paustian, K., 2000. Soil macroaggregate turnover and microaggregate formation: a mechanism for C sequestration under no-tillage agriculture. Soil Biol. Biochem., 32(14): 2099-2103. DOI:10.1016/s0038-0717(00)00179-6

Smet, I., 2012. Lateral root initiation: One step at a time. The New phytologist, 193: 867-73. DOI:10.1111/j.1469-8137.2011.03996.x

Stingaciu, L. et al., 2013. In Situ Root System Architecture Extraction from Magnetic Resonance Imaging for Water Uptake Modeling. Vadose Zone J., 12(1): 9. DOI:10.2136/vzj2012.0019

Stott, D., Martin, J., 1989. Organic matter decomposition and retention in arid soils. Arid Land Research and Management - ARID LAND RES MANAG, 3: 115-148. DOI:10.1080/15324988909381195

Sun, J., Yang, G., Zhang, W., Zhang, Y., 2016. Effects of heterogeneous salinity on growth, water uptake, and tissue ion concentrations of alfalfa. Plant and Soil, 408(1): 211-226. DOI:10.1007/s11104-016-2922-1

Taina, I.A., Heck, R.J., Elliot, T.R., 2008. Application of X-ray computed tomography to soil science: A literature review. Canadian Journal of Soil Science, 88(1): 1-19. DOI:10.4141/CJSS06027

Tanveer, S., Lu, X., Shah, S., Hussain, I., Sohail, M., 2019. Soil Carbon Sequestration through Agronomic Management Practices. DOI:10.5772/intechopen.87107

Tartakovsky, A.M., Meakin, P., Scheibe, T.D., Wood, B.D., 2007. A smoothed particle hydrodynamics model for reactive transport and mineral precipitation in porous and fractured porous media. Water Resour. Res., 43(5): 18. DOI:10.1029/2005wr004770

Tecon, R., Or, D., 2017. Biophysical processes supporting the diversity of microbial life in soil. FEMS Microbiol Rev, 41(5): 599-623. DOI:10.1093/femsre/fux039

Thorslund, J. et al., 2017. Wetlands as large-scale nature-based solutions: Status and challenges for research, engineering and management. Ecological Engineering, 108: 489-497. DOI:10.1016/j.ecoleng.2017.07.012

TISDALL, J.M., OADES, J.M., 1982. Organic matter and water-stable aggregates in soils. Journal of Soil Science, 33(2): 141-163. DOI:10.1111/j.1365-2389.1982.tb01755.x

Tollenaar, M., Wu, J., 1999. Yield Improvement in Temperate Maize is Attributable to Greater Stress Tolerance. Crop Science, 39(6): 1597-1604. DOI:10.2135/cropsci1999.3961597x

Tollner, E.W., Ramseur,, E.L. and Murphy, C., 1994. Techniques and Approaches for Documenting Plant Root Development with X-Ray Computed Tomography, Tomography of Soil-Water-Root Processes, pp. 115-133. DOI:10.2136/sssaspecpub36.c10

Torsvik, V., Øvreås, L., Thingstad, T.F., 2002. Prokaryotic Diversity--Magnitude, Dynamics, and Controlling Factors. Science (New York, N.Y.), 296(5570): 1064. DOI:10.1126/science.1071698

Totzke, C., Kardjilov, N., Manke, I., Oswald, S.E., 2017. Capturing 3D Water Flow in Rooted Soil by Ultra-fast Neutron Tomography. Sci Rep, 7(1): 6192. DOI:10.1038/s41598-017-06046-w

Trachsel, S., Kaeppler, S.M., Brown, K.M., Lynch, J.P., 2011. Shovelomics: high throughput phenotyping of maize (Zea mays L.) root architecture in the field. Plant and Soil, 341(1): 75-87. DOI:10.1007/s11104-010-0623-8

Tracy, J.L., Shariff, A.F., Cheng, J.T., 2010. A naturalist's view of pride. Emotion Review, 2(2): 163-177. DOI:10.1177/1754073909354627

Tracy, S.R. et al., 2015. Three-dimensional quantification of soil hydraulic properties using X-ray Computed Tomography and image-based modeling. Water Resources Research, 51(2): 1006-1022. DOI:10.1002/2014wr016020

van der Heijden, M.G.A., Boller, T., Wiemken, A., Sanders, I.R., 1998. DIFFERENT ARBUSCULAR MYCORRHIZAL FUNGAL SPECIES ARE POTENTIAL DETERMINANTS OF PLANT COMMUNITY STRUCTURE. Ecology, 79(6): 2082-2091. DOI:10.1890/0012-9658(1998)079[2082:DAMFSA]2.0.CO;2

Van Loo, D. et al., 2014. Contrast agents for soil investigation with X-ray computed tomography. Geoderma, 213: 485-491. DOI:https://doi.org/10.1016/j.geoderma.2013.08.036

Vanhees, D.J., Loades, K.W., Bengough, A.G., Mooney, S.J., Lynch, J.P., 2020. Root anatomical traits contribute to deeper rooting of maize under compacted field conditions. Journal of experimental botany, 71(14): 4243-4257. DOI:10.1093/jxb/eraa165

Varney, G.T., Canny, M.J., 1993. Rates of water uptake into the mature root system of maize plants. New Phytologist, 123(4): 775-786. DOI:10.1111/j.1469-8137.1993.tb03789.x

Vetterlein, D., Doussan, C., 2016. Root age distribution: how does it matter in plant processes? A focus on water uptake. Plant and Soil, 407(1): 145-160. DOI:10.1007/s11104-016-2849-6

Vetterlein, D., Kuhn, K., Schubert, S., Jahn, R., 2004. Consequences of sodium exclusion for the osmotic potential in the rhizosphere – Comparison of two maize cultivars differing in Na+ uptake. J. Plant Nutr. Soil Sci., 167(3): 337-344. DOI:10.1002/jpln.200420407

Violante, A., Caporale, A.G., 2015. Biogeochemical processes at soil-root interface. Journal of soil science and plant nutrition, 15: 422-448.

Wang, D. et al., 2020. Change in hydraulic properties of the rhizosphere of maize under different abiotic stresses. Plant Soil, 452(1-2): 615-626. DOI:10.1007/s11104-020-04592-3

Wanyonyi, R.W., Mwangi, J.K., 2016. Impact of human activities on land degradation IN Lugari sub-county, Kakamega county, Kenya. E3 Journal of Environmental Research and Management, 7(2): 038-044. DOI:10.18685/ejerm(7)2_ejerm-16-018

Watanabe, Y., Gould, E., Daniels, D.C., Cameron, H., McEwen, B.S., 1992. Tianeptine attenuates stress-induced morphological changes in the hippocampus. European Journal of Pharmacology, 222(1): 157-162. DOI:https://doi.org/10.1016/0014-2999(92)90830-W

West, T., Post, W., 2002. Soil Organic Carbon Sequestration Rates by Tillage and Crop Rotation: A Global Data Analysis. Soil Science Society of America Journal, 66: 1930-1946.
Whalley, W., Lipiec, J., Stepniewski, W., Tardieu, F., 2000. Control and measurement of the physical environment in root growth experiments. Root Methods: A Handbook: 75-112.
Willatt, S.T., Struss, R.G., Taylor, H.M., 1978. In situ Root Studies Using Neutron Radiography1. Agronomy Journal, 70(4): 581-586. DOI:10.2134/agronj1978.00021962007000040016x
Williams, V., 2011. A Case Study of the Desertification of Haiti. Journal of Sustainable Development, 4. DOI:10.5539/jsd.v4n3p20
Wuana, R.A., Okieimen, F.E., 2011. Heavy Metals in Contaminated Soils: A Review of Sources, Chemistry, Risks and Best Available Strategies for Remediation. ISRN Ecology, 2011: 402647. DOI:10.5402/2011/402647
Yang, H., Kuang, B., Mouazen, A.M., 2012. Quantitative analysis of soil nitrogen and carbon at a farm scale using visible and near infrared spectroscopy coupled with wavelength reduction. European Journal of Soil Science, 63(3): 410-420. DOI:10.1111/j.1365-2389.2012.01443.x
Yoo, G., Spomer, L.A., Wander, M.M., 2006. Regulation of carbon mineralization rates by soil structure and water in an agricultural field and a prairie-like soil. Geoderma, 135: 16-25. DOI:https://doi.org/10.1016/j.geoderma.2005.11.003
Young, I.M., Crawford, J.W., 1992. The analysis of fracture profiles of soil using fractal geometry. Soil Research, 30(3): 291-295.
Young, I.M., Crawford, J.W., 2004. Interactions and self-organization in the soil-microbe complex. Science, 304(5677): 1634-1637. DOI:10.1126/science.1097394
Young, R., Orsini, S., FitzPatrick, I., 2016. Soil Degradation : A Major Threat to Humanity Sustainable Food Trust.
Zahran, H.H., 1999. Rhizobium-legume symbiosis and nitrogen fixation under severe conditions and in an arid climate. Microbiol Mol Biol Rev, 63(4): 968-989.
Zamanian, K., Pustovoytov, K., Kuzyakov, Y., 2016. Pedogenic carbonates: Forms and formation processes. Earth-Science Reviews, 157: 1-17. DOI:https://doi.org/10.1016/j.earscirev.2016.03.003
Zarebanadkouki, M., Ahmed, M.A., Carminati, A., 2016. Hydraulic conductivity of the root-soil interface of lupin in sandy soil after drying and rewetting. Plant and Soil, 398(1): 267-280. DOI:10.1007/s11104-015-2668-1
Zarebanadkouki, M., Carminati, A., 2014. Reduced root water uptake after drying and rewetting. J. Plant Nutr. Soil Sci., 177(2): 227-236. DOI:10.1002/jpln.201300249
Zarebanadkouki, M., Kim, Y.X., Carminati, A., 2013. Where do roots take up water? Neutron radiography of water flow into the roots of transpiring plants growing in soil. New Phytologist, 199(4): 1034-1044. DOI:10.1111/nph.12330
Zeng, Y., Payton, R.L., Gantzer, C.J., Anderson, S.H., 1996. Fractal Dimension and Lacunarity of Bulk Density Determined with X-ray Computed Tomography. Soil

Science Society of America Journal, 60(6): 1718-1724. DOI:10.2136/sssaj1996.03615995006000060016x

Zhang, X., Crawford, J.W., Flavel, R.J., Young, I.M., 2016a. A multi-scale Lattice Boltzmann model for simulating solute transport in 3D X-ray micro-tomography images of aggregated porous materials. J. Hydrol., 541, Part B: 1020-1029. DOI:http://dx.doi.org/10.1016/j.jhydrol.2016.08.013

Zhang, X., Crawford, J.W., Young, I.M., 2016b. A Lattice Boltzmann model for simulating water flow at pore scale in unsaturated soils. Journal of Hydrology, 538: 152-160. DOI:https://doi.org/10.1016/j.jhydrol.2016.04.013

Zhang, X., Deeks, L.K., Glyn Bengough, A., Crawford, J.W., Young, I.M., 2005. Determination of soil hydraulic conductivity with the lattice Boltzmann method and soil thin-section technique. Journal of Hydrology, 306(1): 59-70. DOI:https://doi.org/10.1016/j.jhydrol.2004.08.039

Zhang, X., Lv, M., 2007. Persistence of anomalous dispersion in uniform porous media demonstrated by pore-scale simulations. Water Resources Research, 43(7). DOI:10.1029/2006WR005557

Zhang, X. et al., 2021. The effects of long-term fertilizations on soil hydraulic properties vary with scales. J. Hydrol., 593: 125890. DOI:https://doi.org/10.1016/j.jhydrol.2020.125890

Zhang, X.X., Crawford, J.W., Flavel, R.J., Young, I.M., 2016c. A multi-scale Lattice Boltzmann model for simulating solute transport in 3D X-ray micro-tomography images of aggregated porous materials. J. Hydrol., 541: 1020-1029. DOI:10.1016/j.jhydro1.2016.08.013

Zhang, X.X., Crawford, J.W., Young, I.M., 2016d. A Lattice Boltzmann model for simulating water flow at pore scale in unsaturated soils. J. Hydrol., 538: 152-160. DOI:10.1016/j.jhydrol.2016.04.013

Zhang, X.X., Fan, X.Y., Li, Z.Y., 2016e. Water velocity at water-air interface is not zero: Comment on “Three-dimensional quantification of soil hydraulic properties using X-ray computed tomography and image-based modeling” by Saoirse R. Tracy et al. Water Resour. Res., 52(7): 5687-5690. DOI:10.1002/2015WR018432

Zhang, X.X., Qi, X.B., Qiao, D.M., 2010. Change in macroscopic concentration at the interface between different materials: Continuous or discontinuous. Water Resour. Res., 46: 12. DOI:10.1029/2009wr008853

Zhang, Z.B. et al., 2018. Three dimensional characteristics of biopores and non-biopores in the subsoil respond differently to land use and fertilization. Plant Soil, 428(1-2): 453-467. DOI:10.1007/s11104-018-3689-3

Zhao, L., Hou, R., 2019. Human causes of soil loss in rural karst environments: a case study of Guizhou, China. Sci Rep, 9(1): 3225. DOI:10.1038/s41598-018-35808-3

Zhao, Y., Hu, X., Li, X., 2020. Analysis of the intra-aggregate pore structures in three soil types using X-ray computed tomography. CATENA, 193: 104622. DOI:https://doi.org/10.1016/j.catena.2020.104622

Zhao, Y. et al., 2019. Variations in soil δ13C with alpine meadow degradation on the eastern Qinghai–Tibet Plateau. Geoderma, 338: 178-186. DOI:10.1016/j.geoderma.2018.12.005

Zhou, H. et al., 2018. Evaluating Hydraulic Properties of Biochar-Amended Soil Aggregates by High-Performance Pore-Scale Simulations. Soil Science Society of America Journal, 82(1). DOI:10.2136/sssaj2017.02.0053

Zobel, R.W., 2005. Tertiary Root Systems. DOI:doi:10.2134/agronmonogr48.c3

Zou, Q.S., Hou, S.L., Chen, S.Y., Doolen, G.D., 1995. An improved incompressible Lattice Boltzmann model for time-independent flows. . Journal of Statistical Physics, 81(1-2): 35-48. DOI:10.1007/bf02179966